University of Genoa

Ph.D. Programme in Geophysics

XXII Cycle

Ph.D. Thesis

Numerical modelling of circulation and pollutant dispersion-degradation in coastal waters. An application to the Eastern Ligurian Sea.

Candidate

Patrizia De Gaetano

Supervisor

Prof. Roberto Festa

Coadvisor

Prof. Andrea M. Doglioli

Dott. Massimiliano Burlando

April 2010

Acknowledgments

I must first express my gratitude towards my supervisor Prof. Roberto Festa for his support and advice. I would like to express all my gratitude to my co-advisor Prof. Andrea M. Doglioli. His leadership, support, attention to detail, patience and constant encouragement have helped me to accomplish my PhD. I am also grateful to him for give me the possibility to work with him in the LOPB laboratory in Marseille and for advising me whenever I needed it. I also wish to acknowledge my co-advisor Dr. Massimiliano Burlando for its valuable suggestions and comments and for providing numerous ideas and useful discussions.
More thanks to Prof. Corrado F. Ratto for providing me with many suggestions, important advice and constant encouragement. I am grateful to the whole staff of the Oceanic and Atmospheric Physics Group at the University of Genoa for their technical and human support.
Special thanks to Anne Petrenko for invite me in the LOPB of the Marseille University and for her advice and comments. Thanks also to all the staff of the LOBP laboratory for welcome me and for their interesting and suggests. I am sincerely grateful to ZiYuan Hu for the Symphonie data, the suggestions and her friendship.
I am grateful to Marcello G. Magaldi for his valuable advice and interest in my work. More thanks to Davide Sacchetti and CMRL-PC of the Ligurian Regions for the BOLAM data and for helpful advice. Thanks to Paolo Vassallo, Marco Bartoli and Daniele Nizzoli for the benthic measurements and their great help with the biological part of my thesis.
I am deeply grateful to Cosmo Carmisciano and the whole INGV staff of Portovenere for welcome me in their laboratory and for give me the opportunity to participate to the oceanographic campaign on the ALLIANCE ship. Special thanks to Marina Locritani for having shared with me her office and her passion for oceanography.
Last, but definitely not least, thanks to my fellow students Andrea Zunino, Marco Formenton and Federico Cassola who helped and supported me in many difficult moments.
On a more personal note, I wish to extend my gratitude to Federico, my families and all my friends for instilling in me confidence and for their sincere affection.

Contents

List of Figures

List of Tables

List of publications

- De Gaetano P., Doglioli A.M., Magaldi M.G., Vassallo P., Fabiano M., 2008.
FOAM, a new simple benthic degradative module for the LAMP3D model: an application to a Mediterranean fish farm.
Aquac. Res. 39, 1229-1242.

- De Gaetano P., 2008.
Dispersion and degradation model for marine organic pollutions: an evaluation of sediment impact due to a fish farm.
PLINIUS 34, 11-13.

- De Gaetano P., 2009.
Calibration of the degradation model FOAM by new Mediterranean mineralization rates: evaluation of marine fish farm impact.
PLINIUS 35, 223-225.

- De Gaetano P., Vassallo P., Bartoli, M., Nizzoli D., Doglioli, A.M., Magaldi M.G., Fabiano M., 2009.
Impact of new measured Mediterranean mineralization rates on the fate of simulated aquaculture wastes.
In revision on: Aquac. Res.

- De Gaetano P., Burlando M., Doglioli A.M., Petrenko A., 2010.
Wind forcing effects on coastal circulation and eddy formation around a cape.
Ocean Sci. Discuss., 7, 207-249.

Abstract

Coastal waters are one of the most challenging marine environment to understand and to model. Coastline irregularity, complex bottom topography, fluctuations in the wind and baroclinic instabilities combine to make coastal hydrodynamics very complicated. Consequently, the prediction of the fate of non-conservative tracers, such as biodegradable waste, is particularly difficult. In this field, numerical models reveal to be a very useful tool to handle this kind of studies. Indeed, in scientific literature a large number of numerical models are been developed and applied for simulating flows in realistic conditions and evaluating spread of waste. Moreover, numerical models are successfully used to test different impact scenarios, to identify sensible parameters and to develop mitigation strategies.

In relation to the different anthropic activities acting on the coast, the mariculture represents the one with the most rapid grown in the world. Then, the attention to the possible impact on the surrounding environment increases. Experimental studies indicate that particulate wastes originated by marine fish farms (uneaten feed and faeces) may have a significant environmental impact. Nevertheless, monitoring in space and time the dispersion of that waste is difficult and costly. Therefore, the interest in tracking aquaculture wastes with numerical models has been rapidly increasing in time.

The coastal waters around the Promontorio of Portofino, in the eastern Ligurian Sea (northwestern Mediterranean), represent a very interesting area for this kind of studies. The presence of the cape and the associated complex topography generate current separation, high flow variability and formation and growth of instabilities like coastal eddies and lee waves. Moreover, the installation of an off-shore fish farm in this area of great natural and touristic value has given rise to conflicts about the possible impacts on the surrounding environment.

Three scientific questions are the motivated concerns of this work: i) what is the effect of the degradation on the fate of the settling aquaculture waste? ii) are local Mediterranean conditions to taken in to account to simulate the processes above? iii) how the wind forcing and its resolution affect the coastal circulation in the studied area?

The adopted method is based on the use and the development of an advanced set of numerical models. Starting from a core represented by a high-resolution hydrodynamic model coupled with a dispersion model for aquaculture waste dispersion (POM-LAMP3D), a new benthic degradative model, FOAM, is developed and used to answer to the first question. FOAM uses the outputs of the advection-dispersion model POM-LAMP3D to simulate the organic carbon degradation and the net carbon accumulation on the sediment, evaluating the natural capability of the sea floor in absorbing part of the organic load. In particular, the organic degradation for both uneaten feed and faeces is evaluated by changing release modality (continuous and periodical) and by varying the settling velocities.

The second question is handled by a combined use of *in situ* measurement and numerical sensibility tests. Accurate measurements of particulate carbon input and benthic respiration rates are performed via sediment

traps and intact core incubations in a typical Mediterranean fish farm. The obtained values are used for an accurate comparison between different parameterizations of FOAM.

Finally, in order to answer to the third question, an innovative analysis technique is applied to compare hydrodynamical simulations with different wind forcings.

The present work provided original and innovative answers to the three scientific questions above. It is found that the maximum impact on the benthic community is observed either for quickly-sinking uneaten feed released twice a day, or for less intense near bottom current conditions. If both the above mentioned scenarios coexist, a high stress level is established in the sediment. This fact also suggests that the use of self-feeders in cages can significantly reduce farm impacts.

The *in situ* measurements show, in Mediterranean conditions, smaller carbon flux and oxygen consumption, but a greater degradation capability with respect to the data reported in literature. Moreover, a temperature dependence of the benthic parameters is highlighted. The numerical results with the new parameterization show a smaller benthic impact compared to the old one, due to a minor carbon input and to higher mineralization rates. Furthermore, a seasonal variation is now observed in the organic carbon concentration. Nevertheless, the new results remain consistent with the old ones on two points: a) the negligible benthic impact of faeces with respect to uneaten feed; and b) the dependence of that impact on the different feed release conditions.

Finally, three main wind and current patterns are identified by a cluster analysis. It is shown that the typical wind regimes are coherent with the current ones highlighting the key role played by the wind in enhancing the coastal dynamics and the eddy formation around the cape. Indeed, the effect of the wind is greater near the coast and the higher resolution wind forcing increases the intensity of a coastal countercurrent and an eddy in the lee of the cape.

In conclusion, these results show how the new and more complete modeling framework presented here is able to improve the objectivity in the decision making processes and how it may be successfully used for planning and monitoring purposes.

Nevertheless, there is a real need of *in situ* measurements by eulerian mooring, lagrangian drifter buoys and passive tracers dispersion for future systematic testing and comparison with numerical model results.

Riassunto

Le acque costiere costituiscono uno degli ambienti marini piú impegnativi da studiare e da modellizare poiché l'idrodinamica costiera é resa estremamente complicata dalla presenza di irregolaritá nella linea di costa, dalla complessa topografia del fondale, dalle fluttuazioni del vento e dalle instabilitá barocline. Per questi motivi, la previsione della dispersione in mare di tracciati non conservativi, come ad esempio sostanze biodegradabili, risulta particolarmente difficile.

In questi ambiti di studio, i modelli numerici si sono rivelati strumenti veramente utili; in letteratura sono presenti numerosi esempi di sviluppo e applicazione di modelli numerici per la simulazione di flussi in condizioni realistiche e per la valutazione della dispersione di materiale sospeso. I modelli sono inoltre largamente utilizzati per testare diversi scenari di impatto, identificare i parametri sensibili e mettere a punto strategie di mitigazione degli impatti stessi.

Sono molteplici le attivitá antropiche che insistono sulla fascia costiera e, tra queste, la maricoltura rappresenta quella che ha avuto negli ultimi anni la piú rapida crescita mondiale. Questo ha comportato una crescente attenzione della comunitá scientifica sui possibili impatti che tale attiviá produttiva puó causare sull'ambiente circostante. Numerosi studi sperimentali hanno individuato nel particolato organico originato dalle gabbie di pesci in mare (costituito dal cibo non ingerito e dalle particelle fecali) il principale responsabile degli impatti ambientali dovuti alla produzione di pesce. É importante sottolineare come il monitoraggio spaziale e temporale della dispersione di tali prodotti sia difficoltoso oltre che oneroso, per cui l'utilizzo di modelli numerici per tracciare la dispersione dei residui dell'acquacoltura si é largamente diffuso negli ultimi anni.

Le acque intorno al Promontorio di Portofino, uno scosceso promontorio situato lungo la costa del Mar Ligure orientale (Mar Mediterraneo nordoccidentale), forniscono un'interessante caso studio dei processi sopra citati. Infatti la presenza del promontorio e la frastagliata topografia della costa danno origine a fenomeni idrodinamici quali la separazione della corrente, l'alta variabilitá del flusso e la formazione e la crescita di instabilitá come i vortici costieri sottoflusso al capo. Inoltre, in queste acque di grande valore turistico e naturale, é situato un allevamento intensivo di pesci tramite gabbie galleggianti. La presenza dell'impianto ha generato grande preoccupazione per i possibili impatti sull'ambiente marino circostante dovuti al rilascio dei residui di tale attivitá.

In questo mio lavoro di tesi ho affrontato tre questioni aperte scaturite dal panorama scientifico illustrato, ed in particolare mi sono chiesta: i) quali sono gli effetti della degradazione sul destino dei residui prodotti dagli impianti di maricoltura? ii) le condizioni locali del Mediterraneo sono da tenere in considerazione nella simulazione di questi processi al fine di ottenere un'affidabile valutazione degli impatti ambientali? iii) che ruolo giocano il vento e la sua risoluzione sulla circolazione costiera nell'area d'indagine?

Per lo studio e l'analisi di queste problematiche é stato sviluppato ed utilizzato un insieme avanzato di modelli numerici. Nel dettaglio, per quanto riguarda la prima questione posta, all'insieme di modelli

costituito da un modello idrodinamico ad alta risoluzione accoppiato con un modello di dispersione (POM-LAMP3D) che permette di simulare la dispersione dei residui dell'acquacoltura, é stato aggiunto il nuovo modello degradativo FOAM. FOAM utilizza le uscite del modello avvettivo-dispersivo POM-LAMP3D per simulare la degradazione organica del carbonio derivante dalle gabbie di pesce e l'accumulo netto di questo carbonio sui sedimenti valutando quindi la capicitá naturale dell'ambiente marino nell'assorbire parte del materiale organico che giunge sul fondo. In particolare, le simulazioni effettuate hanno permesso di valutare la degradazione del carbonio organico contenuto nel cibo non ingerito e nelle particelle fecali. Inoltre nelle simulazioni, ho considerato le diverse modalitá di rilascio dei residui (rilascio in continuo e rilascio periodico) e differenti velocitá di sedimentazione delle particelle.

Misure *in situ* e test sulla sensibilitá del modello hanno permesso di rispondere al secondo problema posto. Sono state infatti effettuate, in un tipico allevamento mediterraneo di pesci, misure accurate del carbonio particolato che arriva sul fondale e dei tassi di respirazione del benthos, utilizzando trappole sedimentarie e carote. I risultati sperimentali sono stati utilizzati per riparametrizzare il modello degradativo FOAM. É stato perció possibile confrontare i risultati numerici ottenuti considerando le diverse parametrizzazioni.

Infine, un'analisi innovativa, effettuata su diverse simulazioni idrodinamiche che utilizzano diverse forzanti di vento, ha permesso di rispondere alla terza questione.

Questo mio lavoro ha fornito risposte originali ed innovative alle tre problematiche sopra esposte. In particolare, un maggiore impatto sulle comunitá benthoniche é osservato quando si considerano particelle di cibo con alta velocitá di sedimentazione rilasciate due volte al giorno e quando si verificano condizioni di bassa velocitá della corrente sul fondale. Se entrambi gli scenari descritti coesistono, il sedimento presenta un alto livello di stress. Questo suggerisce l'uso di auto-alimentatori all'interno delle gabbie; tale pratica permetterebbe di ridurre significativamente gli impatti sull'ambientali dovuti ai residui dell'acquacoltura.

Le misure *in situ* effettuate in Mediterraneo presentano valori minori di flusso di carbonio verso il sedimento e di ossigeno consumato rispetto ai dati riportati in letteratura e relativi alle condizioni Atlantiche. Al contrario, la capacitá degradativa é maggiore in Mediterraneo. Inoltre, si osserva una dipendenza dei parametri benthonici dalla temperatura dell'acqua, non rilevata nelle misure in Atlantico. I risultati delle simulazioni numeriche effettuate utilizzando la nuova parametrizzazione del modello FOAM evidenziano un minore impatto sul benthos rispetto ai risultati ottenuti con la parametrizzazione atlantica. Questo é principalmente dovuto al minore input di carbonio organico e ai tassi di mineralizzazione piú elevati. Inoltre si osserva una variabilitá stagionale nei dati di concentrazione di carbonio organico che rimane sul fondale non osservabile utilizzando la parametrizzazione atlantica. I nuovi risultati numerici sono in accordo con i precedenti su due punti: a) l'impatto sul benthos dovuto alle particelle fecali é trascurabile rispetto a quello causato dal cibo non ingerito; b) la modalitá con cui il cibo viene fornito ai pesci ha molta influenza sull'entitá degli impatti.

Infine, la cluster analysis effettuata separatamente sui dati di vento e di corrente costiera ha evidenziato la presenza di tre regimi principali caratteristici dell'area di studio. I regimi tipici del vento sono fluidodinamicamente coerenti con quelli della corrente sottolineando il ruolo chiave giocato del vento sulla dinamica costiera e sulla formazione del vortice sottoflusso al promontorio. Inoltre, l'azione del vento risulta maggiore vicino a costa e l'utilizzo di un vento a piú alta risoluzione come forzate della circolazione determina un aumento dell'intensitá della controcorrente costiera in direzione sud-est e del vortice sottoflusso al capo.

In conclusione, i risultati ottenuti evidenziano come il nuovo e piú completo insieme di modelli qui sviluppato sia in grado di aumentare l'obiettivitá nei processi decisionali e possa essere utilizzato con successo nei procedimenti di pianificazione e monitoraggio. Per testare e migliorare ulteriormente le capacitá predittive dei modelli sarebbero necessarie campagne di misura effettuate utilizzando boe euleriane e lagrangiane e traccianti passivi.

1

Introduction

The ocean is a turbulent fluid that is driven mainly by the mechanical forcing of the winds and the net effect on density of surface exchanges of heat and moisture. It responds according to physical laws for the conservation of mass, momentum, energy and other properties (Semtner, 1995). Analytic solutions of the equations of motion are impossible to obtain for typical oceanic flows. The problem is due to no-linear terms in the equations of motion, turbulence and the need for realistic shapes for the sea floor and coastlines. Moreover, there are some difficult to describe the ocean from measurements. Satellites can observe some processes almost everywhere every few days. But they observe only some processes, and only near or at the surface. Ships and floats can measure more variables, and deeper into the water, but the measurements are sparse.

Hence, numerical models provide a useful, global view of ocean currents. Indeed, they simulate flows in realistic ocean basins with a realistic sea floor and include the influence of viscosity and non-linear dynamics. Moreover, they interpolate between sparse observations of the ocean produced by ships, drifters and satellites and they can calculate possible future flows in the ocean (Stewart, 2008).

However, numerical models are not without problems, as that the numerical models use algebraic approximations to the differential equations and these approximations involved can create spurious solutions (Stewart, 1992). Moreover, numerical models provide information only at grid points of the model. They provide no information about the flow between the points. Yet, the ocean is turbulent, and any oceanic model capable of resolving the turbulence needs grid points spaced millimeters apart, with time steps of milliseconds. Practical ocean models have grid points spaced tens to hundreds of kilometers apart in the horizontal, and tens to hundreds of meters apart in the vertical. This means that turbulence cannot be calculated directly, and the influence of turbulence must be parameterized. Models of the ocean must run on available computers. This means oceanographers further simplify their models. For this reason, the hydrostatic and Boussinesq approximations, and often equations integrated in the vertical, the shallow-water equations (Haidvogel and Beckmann, 1998), are used.

Despite these many sources of error, most are small in practice. Hence, numerical models of the ocean are giving the most detailed and complete views of the circulation available to oceanographers and some of the simulations contain unprecedented details of the flow (Stewart, 2008). Furthermore, significant changes of the currents and property transports occur in response to modified surface forcing, and the correct simulation of these responses is crucial to solving a variety of problems ranging from understanding the history of the Earth system to predicting future climates. These are the challenges for ocean modeling (Semtner, 1995).

The first simulation model was developed by Kirk Bryan and Michael Cox (Bryan, 1969) at the Geophysical Fluid Dynamics laboratory in Princeton. They calculated the 3-dimensional flow in the ocean using the continuity and momentum equation with the hydrostatic and Boussinesq approximations and a simple equation of state. Such models are called *primitive equation* models because they use the basic, or primitive form of the equations of motion. The equation of state allows the model to calculate changes in density due to fluxes of heat and water through the surface, so the model includes thermodynamic processes. The Bryan-Cox model used large horizontal and vertical viscosity and diffusion to eliminate turbulent eddies having diameters smaller about 500 km, which is a few grid points in the model. It had complex coastlines, smoothed

sea-floor features, and a rigid lid. The rigid lid was needed to eliminate ocean-surface waves, such as tides and tsunamis, that move far too fast for the coarse time steps used by all simulation models. The rigid lid had, however, disadvantages. Islands substantially slowed the computation, and the sea-floor features were smoothed to eliminate steep gradients. The first simulation model was regional. It was quickly followed by a global model (Cox, 1975) with a horizontal resolution of 2° and with 12 levels in the vertical. The model ran far too slowly even on the fastest computers of the day, but it laid the foundation for more recent models. The coarse spatial resolution required that the model have large values for viscosity, and even regional models were too viscous to have realistic western boundary currents or mesoscale eddies. Since those times, the goal has been to produce models with ever finer resolution, more realistic modeling of physical processes, and better numerical schemes. Computer technology is changing rapidly, and models are evolving rapidly. The output from the most recent models of the north Atlantic, which have resolution of 0.03° look very much like the real ocean. Models of other areas show previously unknown currents near Australia and in the south Atlantic.

The great economic importance of the coastal zone has led to the development of many different numerical models for describing coastal currents, tides, and storm surges. The models extend from the beach to the continental slope, and they can include a free surface, realistic coasts and bottom features, river runoff and atmospheric forcing. Because the models do not extend very far into deep water, they need additional information about deep-water currents or conditions at the shelf break. Moreover, coastal circulation has been a subject for inquiry by marine scientists insofar as it is one of the most challenging marine environment to understand and to model (e.g. Haidvogel and Beckmann, 1998). Indeed, coastline irregularity, complicated bottom topography, fluctuations in the wind and baroclinic instabilities combine to make coastal current flow systems very complicated. The circulation occurring over the continental shelf typically exhibits considerable temporal and spatial variability. It is characterized by relatively large-scale alongshore current system which have a variety of interannual, seasonal and daily variations. The variability in circulation from place to place is evident in satellite sea surface temperature images which show patchy upwelling zones, filaments of cold water extending offshore, rotating eddies and other large-scale circulation features. Processes responsible for the circulation are wind driven currents and mixing which are often the dominant processes over the shelf, buoyancy effects which lead to plume and frontal formations, shelf-open ocean interactions where meandering offshore currents and mesoscale eddies can entrain much water from the shelf and intense vertical mixing (Blumberg et al., 1993).

The many different coastal models have many different goals, and many different implementations. The last decade has been a veritable explosion of field studies of coastal circulation, made possible by the development of recording current meters which, deployed in array over the shelf, provide long time series of horizontal currents, temperature and salinity. Also, the numerical models have been largely employed for study the complex coastal dynamic. Due to limited computer resources, simple models have been developed in the past. Recently, major computing resources available have been permitted the development of more complex models. Moreover the reliability and the accuracy of the coastal model are increased using validated and tested models (Haidvogel and Beckmann, 1998).

The principal difficulty in modelling a limited region of an ocean basin, such as the continental shelf, is the problem associated with the open ocean boundaries. The effect of the large-scale circulation in the rest of basin must be brought in through boundary conditions. This essentially implies prescribing the transports in and out the region or the baroclinicity and the sea surface elevation along the open boundaries (Blumberg and Kantha, 1985). The problem for the barotropic filtered equations has been found to be ill-posed (Bennett and Kloeden, 1978), as well as for the primitive equations (Oliger and Sundstrom, 1978). Thus the adoption of a specific open boundary condition can strongly affect the solution on the local implementation of the model. For this reason sensitivity experiments, investigating the role and the effect of different lateral open boundary conditions, play an important role in the model performance assessment. As the exact solution is lacking, practical implementations of open boundary conditions in primitive equations for the oceans (e.g. Spall and Robinson, 1989) have been sought. The effectiveness of the specification adopted has to be evaluated with respect to the characteristics of the problem at hand and with regards to the spatial and temporal scales of interest. Even if the specification of prognostic variables on the open boundary is ill-posed in the pure mathematical sense, errors due to this ill-posedness may be insignificant for the flow space and time scales of interest. In this case, for any practical purpose, the boundary conditions specified may be considered viable.

If, on the other hand, the boundary conditions generate or reflect waves that propagate inside the domain, or if they do not effectively transmit information into the interior, or allow information to exit, then they are not considered satisfactory (Spall and Robinson, 1989).

The most popular open boundary conditions are derived from the Sommerfield radiation equation (1949) that provides a simple and stable extrapolation of the interior solution on the open boundary. This condition is based on the assumption that the interior solutions approaching the open boundary propagate through it in a wave-like form. A 2D Sommerfield radiation has been proposed by Raymond and Kuo (1984). The new derivation of the radiation condition takes into account both the normal and tangential component of the wave phase speed. The advantage resulting from this 2D calculation is the increased accuracy in the computation of the normal component of the phase speed, particularly when the direction of propagation has a significant tangential component. The idea proposed by Orlanski (1976) also provides the basis for other open boundary conditions accounting for a selective treatment of inward and outward fluxes. An interesting and useful solution for the open boundary conditions was proposed by Flather (1976). The Flather (1976) condition originates from an attempt to simulate the principal semi-diurnal tide on the north-west European continental shelf using a limited-area 2D numerical ocean model. This condition can be obtained by combining the Sommerfeld condition for the surface elevation with a 1-D approximation of the continuity equation. While the radiation boundary conditions worked well for non-dispersive waves, the application of these boundary conditions to systems which admit dispersive waves (e.g. Rossby waves for which the group velocity and phase velocity may be in drastically different directions) has encountered difficulties (e.g. Cummins and Mysak, 1988). Consequently, modelers often turn to the sponge layers (i.e. regions of heavy damping) to prevent reflection into the model interior (Cummins and Mysak, 1988), or to the grid-nesting method where a coarse grid model is matched to the finer grid model along the open boundary (Robinson and Haidvogel, 1980).

Modelling the dispersion of non-conservative tracers in the marine environment is a very difficult task. The knowledge of water movements is not sufficient to make predictions about the dispersion of such substances in the sea. Additionally to the complexity of the hydrodynamics, a set of processes have to be considered such as the biodegradation of waste. In this way, numerical models, as well as simulate circulation in realistic condition, can be assess the waste spread and their fate when reach sediments or coast. Moreover, models are a unique toll for evaluating proposed emission control techniques and strategy, and for selecting locations of sources of waste, in order to minimize their environmental impacts (Seinfeld, 1975). It is important to note that monitoring and modelling are both necessary and the solution is represented by a synergy of these two tools. In fact, monitoring data are indispensable for inferring theories or parameters and calibrating or validation computer simulation package. Only a well-tested and well-calibrated simulation model can be a good representation of the real world, its dynamics and its responses to perturbations (Zannetti, 1990).

The problem of the marine pollution is felt in particular near the coast. Indeed, as population growth and industrial development continue along the coastal zones, near-shore waters over the continental shelf being subjected to increasing environmental stresses from numerous sources. Discharge of municipal and industrial wastes, agricultural runoff, aquaculture waste, combined sewer overflows and waste spills of potentially toxic substance from coastal commerce contribute collectively to a host of water quality problems. The eventual impact of these discharges is the result of complex bio-chemical interactions and moreover the coastal hydrodynamics results very complex to understand and to model cause of the complex topography, wind variability and baroclinic instabilities (Blumberg et al., 1993).

In relation to the different anthropic activities acting on the coast, the mariculture represents the one with the most rapid grown in the world. Indeed, the increase in global fish consumption and the decrease of wild fish stocks are the main reasons behind the continuous development of marine aquaculture (FAO Fisheries Division, 2006, http://www.fao.org/docrep/009/a0874e/a0874e00.htm). The worldwide expansion of marine fish farms, however, has always been generating concern regarding the possible impacts on coastal ecosystems. Already in 1995, the Food and Agriculture Organization (FAO) of the United Nations adopted a Code of Conduct for Responsible Fisheries. The Code provided the necessary framework for national and international efforts to ensure sustainable exploitation of aquatic living resources. Particular attention was paid to the aquaculture growth in accord with the sustainable and integrated use of the environment, taking into account the fragility of coastal ecosystems, the finite nature of their natural resources and the needs of

coastal communities. In 2001, following the same direction, the European Union started to set up a strategy for sustainable aquaculture development with the Biodiversity Action Plan for Fisheries (COM, 2001a) and the European Strategy for Sustainable Development (COM, 2001b). These two documents led to the more recent and specific Strategy for the Sustainable Development of European Aquaculture (COM, 2002).

Marine aquaculture operations are still very expensive, and the only means by which profitability can be sustained is to intensify fish production. Unfortunately this intensification increases the already existing concerns about reaching and surpassing the natural capability of the environment. The scientific literature has identified the main environmental impact from fish farms to be the release of particulate waste products (Hall et al., 1990; Holmer and Kristensen, 1992; Karakassis et al., 2000; Cromey et al., 2002; Stigebrandt et al., 2004; Corner et al., 2006; Jusup et al., 2009; Reid et al., 2009). Particulate products increase the organic load on benthic environment and might result in changes in the structure and functions of the benthic ecosystem (Tsutsumi et al., 1991; Wu et al., 1994; Vezzulli et al., 2002, 2003; Pergent-Martini et al., 2006; Holmer et al., 2007; Hargrave et al., 2008). Therefore, we are in need for predictive tools able to assess whether or not the establishment of a new farm, or the permission for an increase in production of an already existing one, can result in a potential impact on the surrounding environment.

Numerical models can be used to perform environmental impact predictions and test different scenarios. The interest in tracking aquaculture wastes with numerical models has been rapidly increasing in time as a consequence (Henderson et al., 2001). In the past, we have moved from using analytical models describing oversimplified dispersion patterns in a constant flow in time and space (Gowen et al., 1989), to implementing equations with too many simplifying assumptions about hydrodynamics (Gillibrand and Turrell, 1997). Others have developed particle tracking models using hydrographic data and were therefore limited in their simulations by the sparse data in time and in space (Cromey et al., 2002). Ocean dynamics, instead, are usually very complex and ocean ecosystems are likely to experience current reversals and flow variability. Pioneering numerical studies used circulation models focusing on strongly tidally driven systems. In this case, the flow could have been considered obeying two-dimensional (2D) vertically averaged dynamics (Panchang et al., 1997; Dudley et al., 2000). Unfortunately, the 2D approximation can be inappropriate in more complex and dynamical systems where vertical phenomena affect the dispersion of different particles. More recently, Doglioli et al. (2004b) were the first ones to directly take into account the three-dimensional (3D) ocean circulation and its variability in tracking different aquaculture wastes.

For this kind of studies, I focus my attention on the dynamics and processes taking place in the coastal waters around the Promontorio of Portofino, an abrupt cape rising from the ocean with very steep slopes. It is located along the Ligurian coast in northwestern Mediterranean Sea. The presence of the cape and the complex bathymetry generate current separation, high flow variability and formation of instability like eddies (Doglioli et al., 2004a) that strongly influence the tracer dispersion (Doglioli et al., 2004b). Moreover, this area is characterized by a great importance both for tourism and commercial activities as well as for its great natural environmental value. Since 1998, the Promontorio and its surroundings have been declared Marine Protected Area. Many political and social conflicts have arisen since then, from the contrast between the high tourist pressure and the need for a sustainable management of natural resources (Salmona and Veradi, 2001). In particular, near here is located an off-shore fish farm and it is thought-provoking for the possible impacts that the release of waste might generate on the surrounding environment.

The core and the original intent of this work concern the study and the understanding of three main scientific questions, regarding: the effect of the degradation on the fate of aquaculture waste, the importance to taken into account local Mediterranean condition for the impact predictions and the role played by the wind on the coastal dynamics. The research tool is represented by an advanced set of numerical models.

In regard to the first question, following only the fate of the waste is not sufficient to correctly assess possible impact due to the organic load released by the cages. It should be considered the natural capability of the benthic environment in reacting and absorbing fluctuations in the organic load. For this reason, the model framework composed by a coastal circulation model POM (Princeton Ocean Model, Blumberg and Mellor, 1987) and a dispersion model LAMP3D (Lagrangian Assessment for Marine Pollution 3 Dimensional model, Doglioli et al., 2004b) is here integrated with an additional new numerical benthic degradative model, the Finite Organic Accumulation Module (FOAM). FOAM computes an index of impact based on the ratio between the quantity of oxygen supplied to the sediment and the quantity of oxygen demanded by the

sediment, that is strongly related to the microbial benthic metabolism rate (Findlay and Watling, 1997). On the basis of this index, the sediment stress level and the net organic accumulation on the sea-floor are evaluated.

On the whole, model results are often significantly sensitive to parameterization choices and parameter values (e.g. Pérenne et al., 2001), so that there is a real need for systematic testing and comparisons of numerical model results. Indeed, ocean models, especially ocean biological models, have many uncertain parameters, which should be identified from data or the physics (Lozano et al., 1996; Fulton et al., 2004; Lermusiaux et al., 2006, among others). In many cases, change in certain parameters (non-control parameters) causes only little change in model output. Therefore, these parameters can be approximately determined and then fixed. Change in other parameters (control parameters) causes large change in model output. Thus, the control parameters have to be determined in a very accurate manner because they affect the model predictability. Here, a phenomenological approach may be used to detect model sensitivity to the control parameters, if the number of control parameters is not large. It determines the control parameters, which contribute most to output variability (Chu et al., 2007). Established the control parameters, it may be necessary to determinate them by experiments *in situ* or in the laboratory because the model results are very dependent on the application of the right parameters (Jø rgensen and Bendoricchio, 1994). The second question arises from these considerations. Indeed, the mineralization rates and the oxygen demand are key parameters for the accuracy of the model prediction. Nevertheless, the lack of data collected in Mediterranean conditions forced to use the only available values, i.e. the ones measured under Salmon rearing cages along the Maine coast (Findlay and Watling, 1997). The results of two sampling campaigns performed in a typical Mediterranean fish farm, are employed to fill this gap. Moreover, these specific observations are used to provide new parameter values to FOAM model. Then, an accurate comparison between results with the different parameterizations is performed, together with an assessment of the model prediction capability.

The third question arises from the requirement to moves toward a more realistic scenario for the circulation model. The relation between wind forcing and eddy formation is analysed as a function of the wind flow resolution. The importance of the wind forcing is recognized by many authors (e.g. Castelao and Barth, 2006), but its effect on the coastal circulation is not quantified yet. Moreover, complex orography in coastal area can strongly influence the local wind (Esposito and Manzella, 1982) and the associated oceanic circulation. The hydrodynamical POM model, forced at the inflow open boundary with the data of a coarser regional model SYMPHONIE (Marsaleix et al., 2008), is run between 2001 to 2003. The role of the wind and its resolution on the coastal circulation has been evaluated forcing POM with an atmospheric model BOLAM (BOlogna Limited Area Model, Buzzi et al., 1994). Two different versions of BOLAM model, with different horizontal spatial resolutions, are considered. Moreover, in order to test the sensitivity of the circulation model to the drag coefficient parameterization, different values of this coefficient are used. Furthermore, a cluster analysis performed separately on the wind and current data has allowed to identify the typical wind and current regimes of the area under study.

On the basis of these considerations, the work of this thesis has been undertaken and it is organized as follows. In chapter 2, a general overview of main atmospheric and ocean circulation in the western Mediterranean area is reported. Moreover, wind and ocean circulations characterizing the Ligurian region and, in particular, the eastern Ligurian Sea are analyzed.

In chapter 3, a description of the main features of POM-LAMP3D advection-dispersion model and the degradative one, FOAM, is provided. Moreover, application to aquaculture waste is described investigating the environmental impacts due to the marine fish farm located near the Promontorio of Portofino.

The sampling campaigns performed during 2006, in order to measure benthic degradation parameters in typical Mediterranean conditions and re-parametrize FOAM model, are described in chapter 4. Additionally, new simulations of re-parametrized FOAM are performed in the same Ligurian fish farm. The results are so compared with the ones of the previous chapter, in order to assess the role of the local Mediterranean benthic conditions on the environmental impact evaluations.

In chapter 5, the effect of wind and its resolution on the coastal circulation in the waters around the Promontorio of Portofino is analyzed. Two versions with different horizontal spatial resolutions of the atmospheric model BOLAM are considered to force the high-resolution coastal circulation model POM. Moreover, typical wind and current regimes of the area under study are identified performing a cluster analysis both on the wind data and on the current ones.

The conclusions and the possible future outlooks are explained in chapter 6.

Finally, appendix A summarizes the main features of the numerical models used in this work and in appendix B the FORTRAN code of the developed FOAM model is reported.

2

Atmospheric and ocean-circulation patterns

2.1 Main atmospheric patterns of northwestern Mediterranean

Climatological studies, aimed at defining recurrent weather patterns for the climate classification and climate change monitoring, highlight that both the western and eastern Mediterranean sub-basins are particularly sensitive to the interannual variability of midlatitude cyclones trajectories (Lionello et al., 2006). Moreover, some of the synoptic-scale wind climate regimes of the Mediterranean are expected to show a direct connection with the Mediterranean cyclogenetic activity. This activity is well documented in a number of papers concerning the classification of Mediterranean cyclones (Gleeson, 1954; Campins et al., 2000, 2006) as well as their climatology (Trigo et al., 1999; Maheras et al., 2001; Trigo et al., 2002; Trigo, 2006; Homar et al., 2007).

Burlando (2008) performers a climatological analysis of the large-scale recurrent wind patterns in the Mediterranean Basin. Following this author, the western Mediterranean Basin is characterized by Mistral events and strong cyclogenesis activity over the Balearic Sea and in the lee of the Alps during winter, and extended high-pressure situations all over the Mediterranean during summer, related to the summer monsoons over west Africa, East Africa, and Asia. These patterns correspond to the main topographical and thermal forcing of this region.

The Mistral wind regime usually appears when a lee cyclogenetic event takes place south of the Alps in response to the presence of a parent cyclone over central Europe (Buzzi et al., 1994). This wind is the predominant air mass blowing over the western Mediterranean Basin in winter and it is a cold, dry, continental wind initially blowing over the Gulf of Lions and the Ligurian-Provençal basin (May, 1982). The Alps also plays a crucial role in determining the Mistral pattern as well as the orographic cyclogenesis in the Ligurian Sea. Reaching the sea surface of a warmer sea, the Mistral wind becomes unstable in the lower layer and causes intense air-sea interactions processes at the sea interface that are most intense in the northern part of the Mediterranean Sea. The heat, water vapor and momentum fluxes associated with the Mistral events are much greater than the fluxes resulting from any other flow from other directions. For these properties the Mistral is considered also the most important factor conditioning the physical properties of the water mass of the northern Mediterranean Basin in winter (Bunker, 1972).

2.1.1 Ligurian wind circulation

Liguria, having a surface of about 5100 km^2, is placed in northwest Italy and creates an ample gulf in the Mediterranean Sea. Its landscape is dominated by the mountains of the Maritime Alps in the western part and of northern Apennines in the east. These mountains reach as much as 2200 m in the Alps and about 1700 m in the Apennines, usually fairly close to the coast. The valleys are short, irregular, and deeply sloped, making Liguria orography very complex. Liguria has a mild climate, where the role of the sea and the interaction between the movement of air masses and orography is very important. The chains of mountains, surrounding the northern part of Liguria Gulf, create a shield against cold northern winds, that can penetrate the region mainly through valleys and depressions, for instance near Genoa and Savona (Conte et al., 1998). In such a

narrow region, squeezed between the sea and the mountains, with few flat areas and with short valleys the wind strongly depends on the topography and its variability is stronger in a region such as Liguria with its sharp reliefs and long meandering coastline.

The orographic cyclogenesis in the Ligurian Sea is more frequent from October to May (Gleeson, 1954). A statistical analysis performed by Esposito and Manzella (1982) of the wind measured in Genoa shows that in winter the winds are generally north or north-westerly, while in summer the prevailing winds are southerly. Moreover, as expected, the comparison among the wind speed and direction distributions corresponding to measurements recorded at Genoa, Pisa and Nice shows that they are strongly influenced by the surrounding orography (Alps and Apennines). All the aforementioned wind regimes are thought to be tightly connected to the characteristics of the water mass in the Ligurian Sea.

2.2 General ocean circulation in the northwestern Mediterranean Sea

The circulation in the western Mediterranean Sea exhibits strong seasonal and interannual variability. The circulation is extremely complex, consisting of numerous eddies and current meanders, particularly along the north African coast and in the Algerian basin. There are many physical factors which exert an influence on the dynamics of the circulation of the western Mediterranean Sea; wind stress, hydraulic controlled inflow-outflow through the Straits of Gibraltar, thermohaline forced circulation and topography.

The large-scale cyclonic circulation in the northwestern Mediterranean is, at least in the upper layers, less coherent in winter and spring than in summer and autumn. Moreover, the mesoscale structure (eddies and meanders) is, during all year, a significant dynamic characteristic in this region of the Mediterranean Sea. Concerning the circulation in the lower layers, Levantine Intermediate Water and Western Mediterranean Deep Water follow essentially a cyclonic path during all year. Indeed, as aforementioned, the entire region is affected by very severe weather conditions in winter, which are most intense in the Gulf of Lions. These are mostly caused by the periodic intrusions of the cold continental winds, Mistral and Tramontana, that blowing over the warmer sea, induce relevant air-sea interaction processes that subtract heat and water to the involved regions. With reference to the Gulf of Lions, Bunker (1972) has estimated that the winter (February) evaporative rates are 0.54 g cm^{-2} day^{-1}, with peaks of 2.30 g cm^{-2} day^{-1} during the strongest Mistral event. These values largely exceed those of the adjacent regions, in particular the Tyrrhenian Sea that because of the blockage of the mountains of Corsica and Sardinia, is outside the direct influence of these air masses. The monthly values of evaporation, and the sensible and latent heat loss from the Gulf of Lions show that the transfers are low during summer and gradually increase from October through February with a maximum in December. Bunker (1972) had considered this the major factor conditioning the surface layer to become dense enough to sink. A cyclonic gyre about 100 km wide is then generated (probably influenced by the Rhone River fan, Swallow and Canston, 1973), and is inscribed into the general cyclonic circulation. This gyre defines the specific area for the Deep Water Formation (DWF) processes. These processes affect the Gulf of Lions, even though they can also develop in the Ligurian Sea and the Catalan Sea at a more reduced rate. Outside the less accessible subpolar regions, this is one of the few places in the world ocean where DWF occurs and this widely explains the general attention rendered to this region.

2.2.1 Northern Current

In the north of the western Mediterranean Sea, water circulation takes the form of a rim current, the Northern Current (NC), forced, for at least a year, by increase in density caused by wintertime air-sea interactions and the sinking of surface waters (Crépon and Boukthir, 1987). Thus, the NC flows anticlockwise along the slope, i.e. roughly towards the west.

In the Ligurian Sea, especially off the Côte d'Azur, there is almost no shelf; hence, the NC is of major importance in the coastal zone circulation. Here, the NC is generally (spring to autumn) wide (40-60 km) shallow (100-150 m) and located relatively far from the coast. In winter, it becomes narrower ($<$30 km), deeper ($>$200 m) and lies closer to the coast (Albérola et al., 1995). Instability processes have been shown to generate steep mesoscale meanders (of a few 10's km, in both amplitude and wavelength); these propagate downstream, at 10-20 km/day, particularly in winter (Crépon et al., 1982). This mesoscale activity markedly increases from autumn to winter, then progressively decreases (Taupier-Letage and Millot, 1986; Albérola

et al., 1995). From spring to autumn, phenomena, with time-scales ranging from 1-2 to 20-40 days, have been shown to propagate downstream at speeds ranging from 10-12 to 3-7 km/day, respectively (Sammari et al., 1995). NC interactions with the canyon topography probably generate currents of a relatively small scale, which can reach easily the coastal zone and lead to very complex circulation patterns. In the Ligurian Sea, seasonal and mesoscale variabilities are characterised by a NC more intense, narrower and deeper, lying closer to the slope and being more unstable in winter.

2.2.2 Coastal circulation in the eastern Ligurian Sea

The Ligurian coastal circulation is part of the general cyclonic circulation of the Mediterranean Sea (Castellari et al., 2000; Molcard et al., 2002), which affects both the surface layer of Modified Atlantic Water and the underneath Levantine Intermediate Water layer, with a thermal front dividing the warmer coastal water from the colder water in the interior. The eastern part of the Ligurian sea appears to play an important role for the comprehension of the dynamic characteristics of the basin. Astraldi et al. (1990) show that two currents converge in that region, coming from the north-west side of Corsica (West Corsican Current) and the Corsican Channel (Tyrrhenian Current). Though both flowing northward, they differ in some basic properties: whereas the West Corsican Current maintains almost stable features year round, the warmer Tyrrhenian Current is more energetic in winter than in summer, which gives it a strong seasonal signal. A marked frontal structure found nearly parallel to the coast over the shelf, divides this coastal current from the basin's interior, characterized by a doming of the internal hydrologic structure extending from the Catalan Sea to the Ligurian Sea. Although basically cyclonic year-round, this pattern undergoes significant changes from winter to summer, when the circulation appears to be divided into two major structures inherent to the two sub-basins.

Historical measurements of the coastal current upstream of the Promontory of Portofino are available in terms of long currentmeter time series and hydrographic surveys (Esposito and Manzella, 1982; Astraldi and Manzella, 1983; Astraldi and Gasparini, 1986). They indicate the existence of a northwestward current flowing approximately along the isobaths and following the narrow shelf. The current appears well organized and consistent, at least during the winter period when the wind blowing from north direction reinforce the general circulation of the Ligurian Sea. The transport is approximately of 0.3 Sv on the shelf. Moreover, the *in situ* measurements (Astraldi and Gasparini, 1986) and the numerical study (Doglioli et al., 2004a) highlight the presence of an anticyclonic eddy in the lee of the cape. The eddy appears persistent for a period of the order of a month, at least in the winter period. A coastal southeastward countercurrent is present during the summer in the Gulf of Genoa and it is associated to periods of prevailing southerly winds. It is a drift current which characteristics depend on the coastal curvature (Esposito and Manzella, 1982). Moreover, Esposito and Manzella (1982) find that the shelf circulation is forced by the deep basin circulation and the local wind that has a high variability both in intensity and direction, largely to be attributed to the land morphology (Bruschi and Manzella, 1980).

3

FOAM model

This chapter takes place following the continuous effort in improving the framework initially set up by Doglioli et al. (2004b). The improvements and the assessment of their relative importance have been done mainly in three areas and represent the core and the original intent of this chapter. Namely, I

(a) improved the hydrodynamics using real historic current-meter data to force the simulations;

(b) improved the dispersion using a larger number of particles and updating the settling velocity values specifically for Mediterranean fish species and for their feed;

(c) added a new coupled benthic module to consider the environmental response to the organic load from the cages.

Doglioli et al. (2004b) used idealized winds to force simulations. The choice of the winds was based on a statistical treatment of 34 years of wind data and it allowed to carry out a complete 12-day hydrodynamic simulation during which wind direction and speed were changing according to a typical local meteorological sequence. In a later paper, Doglioli et al. (2004a) successfully used historical current-meter data to study the hydrodynamic characteristics of the area under examination. Since the focus of this work is to move toward a more realistic scenario, I decided to implement the already validated forcing setup used in Doglioli et al. (2004a). This mainly implies that the open boundary conditions and the forcing evaluation are improved by applying realistic current measurements.

On the other hand, settling velocity values for uneaten feed and faeces represent key parameters for aquaculture waste dispersion models. The lack of values specifically targeting Mediterranean fish and their feeds obliged Doglioli et al. (2004b) to use the only values available in the literature, i.e. the ones measured for salmonids (Chen et al., 1999a,b). However, two recent works filled this important gap. On one side, Vassallo et al. (2006) presented the settling velocities of a feed usually utilized in Mediterranean farms (the 'Marico Seabass and Seabream' pellets produced by Coppens International), while on the other side, Magill et al. (2006) measured the settling velocities of Gilthead Sea Bream and Sea Bass faecal particles collected in sediment cores in a Greek fish farm. A second original aspect of this chapter is that it uses these new values, paying particular attention to the role they play in the overall results.

Finally, following only the fate of the particles as in Doglioli et al. (2004b) is not sufficient to correctly assess the organic load on the sea bottom. The modeling effort should consider the natural capability of the benthic environment in reacting and absorbing fluctuations in the organic load. For this reason, the model framework is integrated with an additional new numerical benthic degradative module, the Finite Organic Accumulation Module (FOAM). FOAM is mainly based on the ideas expressed in the work of Findlay and Watling (1997). They proposed an index of impact based on the ratio between the quantity of oxygen supplied to the sediment and the quantity of oxygen demanded by the sediment. The oxygen supply is a function of the near bottom flow velocities and is calculated by the empirical relation put forth by Findlay and Watling (1997). The oxygen demand is based on the organic load from the cages and it is strongly related to the microbial benthic metabolism rate. As pointed out by the same authors, the equations proposed by Findlay and Watling (1997) can be easily exploited by numerical modelers since the only needed input

variables are the bottom flow velocities and the organic flux toward the seabed. Since the model does consider the vertical dimension, it is also able to provide these important required data. Furthermore, its intrinsic Lagrangian nature allows a simple numerical implementation of the ideas proposed in Findlay and Watling (1997).

3.1 Numerical methods

The simulations are carried out for the offshore fish farm located east of Lavagna in the Ligurian Sea, already considered by Doglioli et al. (2004b) (Fig. 3.1). The sea cages are located at about 1.5 km from the coast

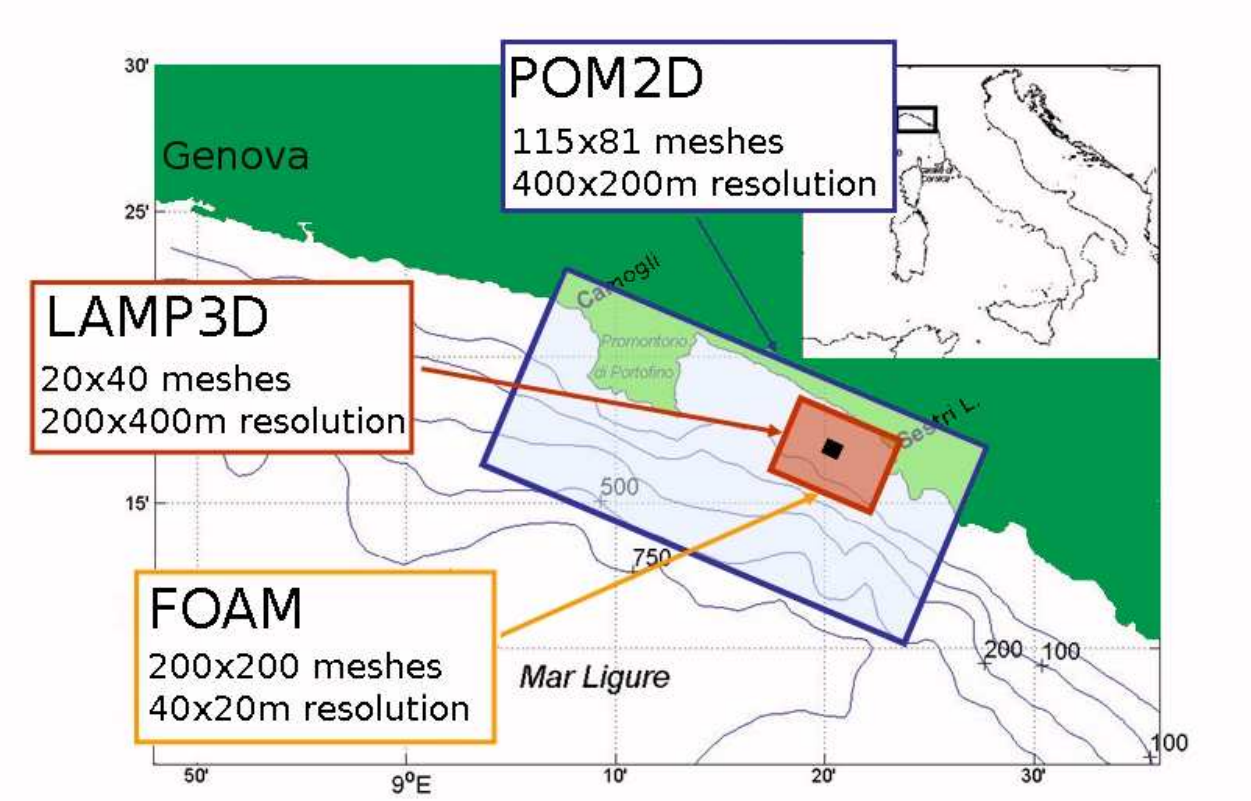

Figure 3.1: Study area, position and dimensions of the three different model grids. The lines are the isobaths in meters while the black square represents the fish farm position.

and they cover an area of 0.2 km^2. The bottom depth ranges between 38 m and 41 m. The farm is composed of 8 fish cages with a capacity of 2000 m^3 each. The reared biomass is 20 kg m^{-3} for an annual mean production of about 200 ton year^{-1}. The fish in the cages are Gilthead Sea Bream (*Sparus aurata*) and Sea Bass (*Dicentrarchus labrax*).

The modeling framework consists of different models which are coupled together into a single functional unit (Fig. 3.2). The hydrodynamic model is the Princeton Ocean Model (POM) and it is used to derive space and time information of the circulation of the coastal area. POM (Blumberg and Mellor, 1987) is primitive equation, free surface, sigma coordinate ocean model, based on Boussinesq and hydrostatic approximations. In our implementation the horizontal components of depth-averaged current are computed on an Arakawa-C grid and the vertical turbulence closure is based on the Mellor and Yamada (1982) model. POM is coupled on-line with the three-dimensional Lagrangian Assessment for Marine Pollution model (LAMP3D).

LAMP3D (Doglioli et al., 2004b) is single particles Lagrangian model providing the particle positions by so-called "random walk" approach. In this kind of model at each time step, the particle position is calculated on the basis of the flow velocity (here computed by POM) representing the transport process and a random

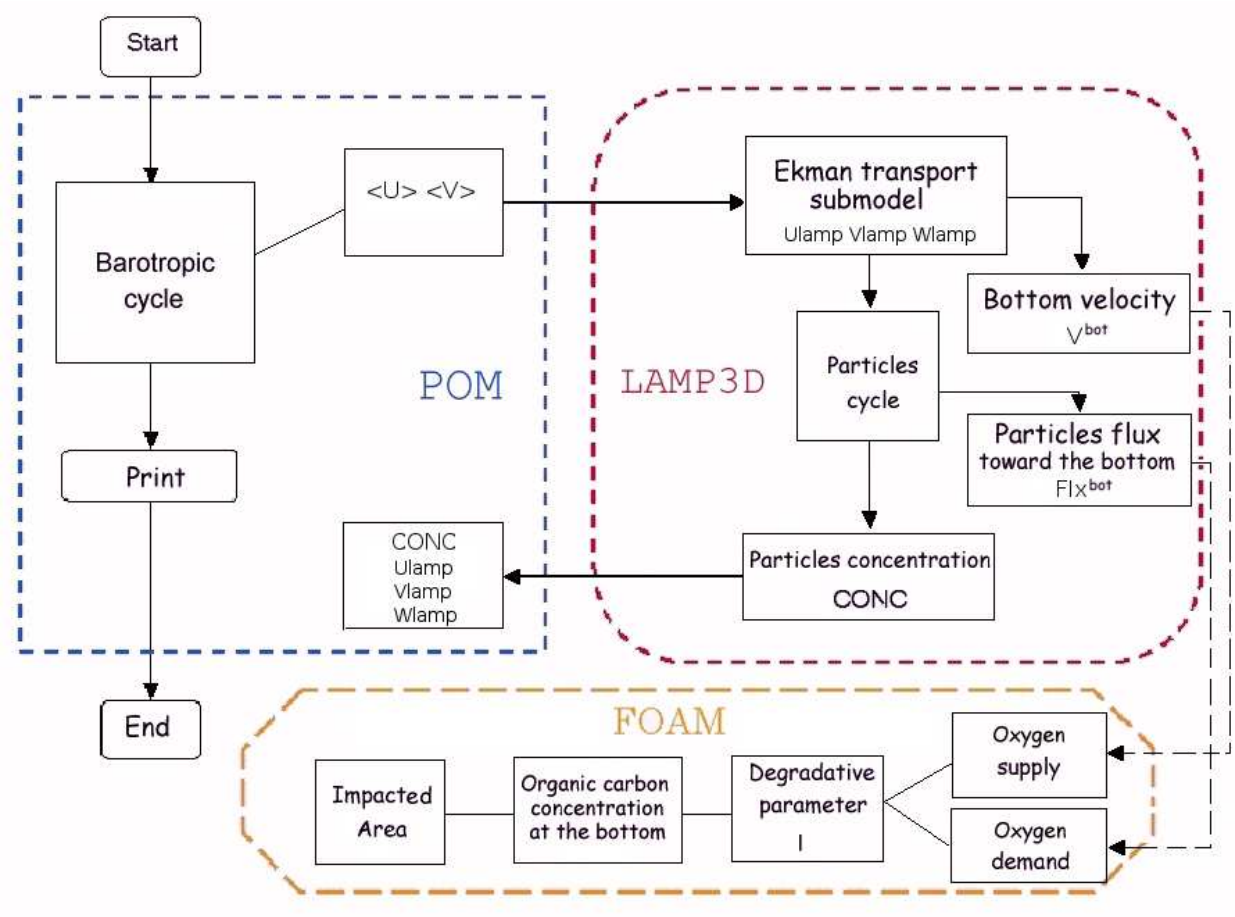

Figure 3.2: Model flow chart. Thick solid arrows represent on-line connections, while thick dashed lines represent off-line connections. FOAM reads bottom velocity and particles flux and computes oxygen supply and demand. The two parameters give information on the sediment and on the benthic stress.

jump representing the turbulent diffusion. An interesting aspect of that approach is the possibility of assigning different characteristics at each numerical particle in both hydrodynamical behaviour and in biogeochemical content. Therefore, LAMP3D is used to track the particle positions in time and space.

The Finite Organic Accumulation Model (FOAM) represents the biochemical component of the modeling system and it uses POM and LAMP3D outputs to estimate the potential environmental impact due to the organic load from the cages. POM and LAMP3D calculate the bottom velocities and the particle fluxes to the bottom and these values are then used by FOAM to calculate the final organic load in each mesh of its numerical domain.

The following part of this section gives more details of the entire modeling framework. For an exhaustive description both of POM and LAMP3D models, see sections A.1 and A.3 of appendix A, respectively.

3.1.1 Implementations of the advective-dispersive models

Some historical measurements of the coastal current in the area are available in terms of current-meter time series and hydrographic surveys, covering a total of 10 months during 1978 - 1979 (Astraldi and Manzella, 1983). Data are archived in the SIAM database (http://www.santateresa.enea.it/wwwste/siamen/home.htm), and they have been kindly provided to us by the Italian National Agency for New Technologies, Energy and Environment (ENEA) and the National Research Council (CNR). I concentrate on the winter-spring period, when the currents are stronger and better defined and the stratification is being formed. The period from 8 February 1979 to 30 June 1979 is selected and the model on the eastern (incoming) boundary is forced. At the western (outcoming) boundary a radiation condition is imposed to radiate barotropic velocity. Finally, at the southern boundary, considering negligible the interaction with the open sea, a free sleep wall is posed. The described setup is the same used and validated in Doglioli et al. (2004a).

Here, complete four-month simulations are carried out, obtaining current data necessary for the dispersion-degradation runs. The first velocity value (U=-0.19 m s^{-1}), measured on 8 February 1979, is provided on the whole domain as an initial condition for all the simulations. Since the objective is simulating longer time periods, the real current-meter data as boundary conditions to force the runs are cyclically repeated. Consequently, the organic matter accumulation on the seabed can be estimated for longer time periods and the dependence of the model results on the initial condition can be reduced.

Moreover, since the primary focus of this chapter is the organic load on the seafloor and not the fate of the dissolved nutrients, a new setup is adopted with respect to that used in Doglioli et al. (2004b) for the hydrodynamical model POM and the dispersive model LAMP3D. The POM grid has 115 $\times$ 80 meshes with a spatial resolution of 400 m along the x-direction and 200 m along the y-direction (Fig. 3.1). This resolution reflects the best available bathymetric data in the area. The LAMP3D numerical domain, instead, is smaller (8 km $\times$ 4 km), and it is nested in the POM grid with the same spatial resolution (400 m $\times$ 200 m).

The other dispersive parameters are unchanged with respect to Doglioli et al. (2004b), with the exception of the Lagrangian particle number that was increased to 620000 for greater precision and better rendering. The Doglioli et al. (2004b)'s assumptions on the organic carbon concentration in feed and faecal waste are adopted. In particular, the value of 5% for the feed loss was recently confirmed by results of MERAMED project (http://meramed.akvaplan.com). Nevertheless, since the number of particles is increased with respect to Doglioli et al. (2004b), new conversion factors for uneaten feed and faecal waste (Table 3.1) are calculated. I also keep calculating nitrogen loading rates for validation purposes (see section 3.2) using the same conversion factors used in Doglioli et al. (2004b) for nitrogen.

The lack of data for Mediterranean species obliged Doglioli et al. (2004b) to use the values proposed by Chen et al. (1999a) and Chen et al. (1999b) for salmonids. Recently, Magill et al. (2006) have measured the settling rates of faecal material of Gilthead Sea Bream and Sea Bass, while, under laboratory conditions reproducing the Mediterranean sea water, Vassallo et al. (2006) have provided the settling velocity values of a typical growing sequence of feed pellets for the same species. Therefore, the values of these recent works in the simulations are used.

All the parameters used in the hydrodynamic and dispersive models are summarized in the upper part of Table 3.1, while the different settling velocity values are reported in Table 3.2.

POM-LAMP3D parameters	**value**
POM physical domain (km)	46x16
LAMP3D physical domain (km)	8x4
Horizontal resolution (m)	400x200
Vertical resolution (m)	10
Barotropic cycle time step (s)	1
Smagorinsky diffusivity coefficient	0.1
Asselin filter coefficient	0.05
Ekman depth δ_E (m)	50
Wind drag coefficient C_d	0.001
Horizontal standard deviation $\boldsymbol{\sigma}$ (m)	3.46
Particle cycle time step (s)	60
Number of particles	620000
Feed conversion factor for organic carbon w^C_{feed} (mmolC particle^{-1})	308.6
Faeces conversion factor for organic carbon w^C_{faeces} (mmolC particle^{-1})	5.8
Feed conversion factor for nitrogen w^N_{feed} (mmolN particle^{-1})	167.8
Faeces conversion factor for nitrogen w^N_{faeces} (mmolN particle^{-1})	66.4

FOAM parameters	**value**
Physical domain (km)	8x4
Horizontal resolution (m)	40x20
O_2 supply parameter A (mmolO_2 m^{-2} d^{-1})	736.3
O_2 supply parameter B (mmolO_2 s m^{-3} d^{-1})	672.5
O_2 demand parameter C (mmolO_2 mmolC^{-1})	1.07
O_2 demand parameter D (mmolO_2 m^{-2} d^{-1})	-32.6
Settled matter non-stress N_s (mmolC m^{-2} d^{-1})	27.53
Settled matter intermediate-stress I_s (mmolC m^{-2} d^{-1})	57.50
Settled matter hyper-stress H_s (mmolC m^{-2} d^{-1})	30.59
I range amplitude parameter Δ_{fw}	0.5

Table 3.1: Input parameters for POM-LAMP3D and FOAM.

Feed pellets		**Faecal pellets**	
Diameter (mm)	V_{sed} (m s^{-1})	Fish species [size (g)]	V_{sed} (m s^{-1})
3	0.087 ↓	*S. Aurata* [380]	0.004 ↓
3.5	0.118	*S. Aurata* [60]	0.005
4.5	0.103	*D. Labrax* [280]	0.006
5	0.144 ⇓	*D. Labrax* [80]	0.007 ⇓
6	0.088		

Table 3.2: Settling velocity values for feed and for faecal pellets . The arrows indicate the values used in the experiments: slowly (↓) and quickly (⇓) sinking particles.

3.1.2 The benthic module: FOAM

A new bottom boundary condition is implemented in the model. When a numerical particle touches the seabed, it is considered as biodegradable settled matter and it is treated by the benthic module FOAM. FOAM covers the same area of the dispersive model but its resolution is 10 times higher, namely 40 m $\times$ 20 m (Fig. 3.1). This resolution adequately represents the known processes of degradation and is acceptable in terms of computational time. In the case of FOAM, a higher resolution is feasible because its calculations are performed off-line.

According to Findlay and Watling (1997), the organic accumulation on the bottom leads to different rates of mineralization in relation to the level of stress the seabed is exposed to. In order to simulate the biological reaction of the microbial benthic community to the variations in the organic enrichment, the status of the sediment in each grid mesh according to the ratio between the benthic oxygen supply and the demand, is assigned.

In FOAM, the same equations and constants proposed by Findlay and Watling (1997) are used. The oxygen supply is a function of the near bottom velocities and can be calculated by simple Fickian diffusion arguments and expressed by the empirical relation

$$\mathrm{O}_2^{sup} = A + B \cdot \log(V^{bot}) \tag{3.1}$$

where A and B are constants (see Table 3.1) and V^{bot} is a time averaged current velocity taken at 1 m from the bottom. It is important to note that V^{bot} is just the numerical value of the bottom flow velocity when it is expressed in cm s^{-1}. In the model this value is obtained by linear interpolation of the velocity in the deepest vertical grid cell and by using an average time interval of $\Delta t = 2$ hours. This choice was already made by Findlay and Watling (1997) to describe oxygen supply to the benthos. Moreover, this time interval seems to be critical, since a 2 hour exposure to reduced oxygen and elevated hydrogen sulfide concentrations causes permanent damage to the gill tissues of sensitive infauna (Theede et al., 1969). The same choice of $\Delta t = 2$ hours is also supported by the more recent work by Morrisey et al. (2000).

The oxygen demand, instead, is a function of the organic carbon flux toward the sea bottom Flx^{bot} according to the relation

$$\mathrm{O}_2^{dem} = C \cdot Flx^{bot} + D \tag{3.2}$$

where, again, C and D are just constants (Table 3.1; for more details refer to Fig. 2 and Fig. 3 in Findlay and Watling (1997)).

If i and j are the grid mesh indexes in the x and y directions respectively, the carbon flux Flx^{bot} in each grid mesh (i, j) at the instant k is calculated on the basis of the number of particles reaching the bottom, $n_{i,j}^{bot}$, during an integration time interval dt, i.e.

$$Flx_k^{bot} = \frac{n_{i,j}^{bot} \cdot w^C}{dt \cdot \Delta x \cdot \Delta y} \tag{3.3}$$

In the equation (3.3), Δx and Δy are the horizontal grid sizes while w^C stands for the adopted organic carbon conversion factor. w^C varies considering feed or faeces and the different values are listed in Table 3.1.

Once the model provides O_2^{sup} and O_2^{dem} for each grid mesh, the index of impact I can be calculated as suggested by Findlay and Watling (1997) as

$$I_{i,j} = \frac{O_2^{sup}}{O_2^{dem}} \tag{3.4}$$

Based on I, three different levels of stress can be identified: non-stressed sediments, intermediately-stressed sediments and highly-stressed sediments. Findlay and Watling (1997) suggested that when $I > 1$, the supply of oxygen is in excess of the demand and therefore the impact is minimal. When $I \approx 1$ the impact can be moderate while when $I < 1$, the sediment exhibits the azoic sediment endpoint and the resulting impact is high. In the model the discrete Findlay and Watling (1997) criterion for the different levels becomes:

- no stress, if $I_{i,j} > 1 + \Delta_{fw}$;
- medium stress, if $(1 - \Delta_{fw}) \leq I_{i,j} \leq (1 + \Delta_{fw})$;
- high stress, if $I_{i,j} < 1 - \Delta_{fw}$.

Sensitivity tests on the Δ_{fw} parameter are performed in a range varying from $\Delta_{fw} = 0.05$ to $\Delta_{fw} = 0.5$. No meaningful differences have been observed, so, for precautionary reasons, the value of $\Delta_{fw} = 0.5$ is adopted.

When the level of stress is decided according to the value $I_{i,j}$, different rates of mineralization are used in each grid mesh. In the code, this is obtained by subtracting different quantities to the already calculated organic carbon concentration fluxes. The subtracted amounts are the same as Findlay and Watling (1997) and are shown in the lower part of Table 3.1. On the basis of the obtained fluxes, the organic carbon concentration $Conc^{bot}$ in each grid mesh (i, j) is calculated as

$$Conc^{bot} = \sum_{k=1}^{NT} Flx_k^{bot} \cdot dt \tag{3.5}$$

where NT is the number of the time intervals of the simulation.

All the parameters used in the benthic module are summarized in the lower part of Table 3.1.

3.2 Results

The modeled water circulation is in agreement with the past literature in the area: the simulations show the presence of the observed westward transport (Astraldi and Manzella, 1983; Astraldi et al., 1990), persisting for almost the entire simulated period (winter-spring). The obtained general circulation also agrees with other numerical experiments such as Baldi et al. (1997) and Doglioli et al. (2004b). It is also possible to observe current separation and eddy formation behind the Portofino Promontory as in Doglioli et al. (2004a). For a more quantitative hydrodynamic validation, the same approach as in Doglioli et al. (2004b) is used. Current data simulated by the model are compared with data collected by one current meter, C1, located at 2 km to the west of the farm (Fig. 3.3). Current speed and direction were sampled every hour at 20-m depth from February 1993 to March 1994. Table 3.3 shows current data from C1 and the model outputs.

When only one cycle at the eastern boundary is used and the first velocity value on the whole domain as an initial condition is prescribed, the seasonal averages from the observations are systematically lower than the model ones (see values for the first cycle). When the boundary conditions to force the runs are cyclically repeated and the last velocity field of the previous cycle is used as the initial condition, the comparison with the C1 data improves (see the values for the fifth cycle). The larger discrepancy observed in the first cycle is due to the artificial highly energetic initial condition. Therefore, I decide to run five cycles of linked simulations and subsequently neglect the first two in order to reduce the sensitivity to the initial conditions. The three linked cycles account for a total of 430 simulated days and their averages are also reported in Table 3.3. In this case, the data are very close to the values calculated by the model. Current direction agrees

	Observations (m s^{-1})				
	Winter average (std)	Spring average (std)	Summer average (std)	Autumn average (std)	Annual average (std)
C1	0.066 (0.057)	0.075 (0.065)	0.063 (0.052)	0.070 (0.052)	0.069 (0.057)
	Model Output (m s^{-1})				
	Winter average (std)	Spring average (std)	Summer average (std)	Autumn average (std)	Overall average (std)
1st cycle	0.076 (0.051)	0.103 (0.084)	- -	- -	0.088 (0.047)
5th cycle	0.059 (0.034)	0.082 (0.066)	- -	- -	0.057 (0.034)
3th → 5th cycles	0.064 (0.042)	0.078 (0.050)	- -	- -	0.061 (0.034)

Table 3.3: Comparison between current measurements and model outputs at 20-m depth.

with the observed along-shore water movement. Sporadic current reversals are also simulated thanks to the inversions of the direction of the velocity at the inflow boundary condition.

At the same time, sediment observations around the cages are used to validate the dispersive runs. A Van Veen grab was used to collect sediment samples in three repetitions in each of the four stations surrounding the fish farm (Fig. 3.3).

With respect to Doglioli et al. (2004b), additional recent data were collected in the same stations. All the samples were analyzed for total nitrogen and total phosphorus. The comparison between absolute values of these data and the model outputs is not possible since, in order to express both of them in the same units, we would need to make strong assumptions on the sediment density as well as on the sampling methodology. Therefore, the same approach utilized in Doglioli et al. (2004b) is used. Fig. 3.4 shows the agreement between the field and modeled data. In particular, field sediment nutrients are highest in station S2 and lowest in station S4, which agrees with model output for total nitrogen under westward transport.

To facilitate the comparison of results, in the same Fig. 3.4, the performance of the old setup adopted in Doglioli et al. (2004b) and the field data as they were at that time are also reported.

The above comparison with the only data available in the area, allows us to focus on the dispersion model and on the benthic modeled impact. The time series of the dispersion model output are also referred to the three last cycles of linked simulations. In order to explore the differences in the runs by varying waste typology, release condition and settling velocity, the following experiments are performed:

A1) slowly sinking feed in continuous release;

A2) quickly sinking feed in continuous release;

B1) slowly sinking feed in periodical release;

B2) quickly sinking feed in periodical release;

C1) slowly sinking faeces (continuous release);

C2) quickly sinking faeces (continuous release).

Periodical release means that the feed is supplied twice a day, and slowly and quickly sinking are referred to the minimum and maximum values listed in Table 3.2 for the two different waste typologies. In Table 3.2

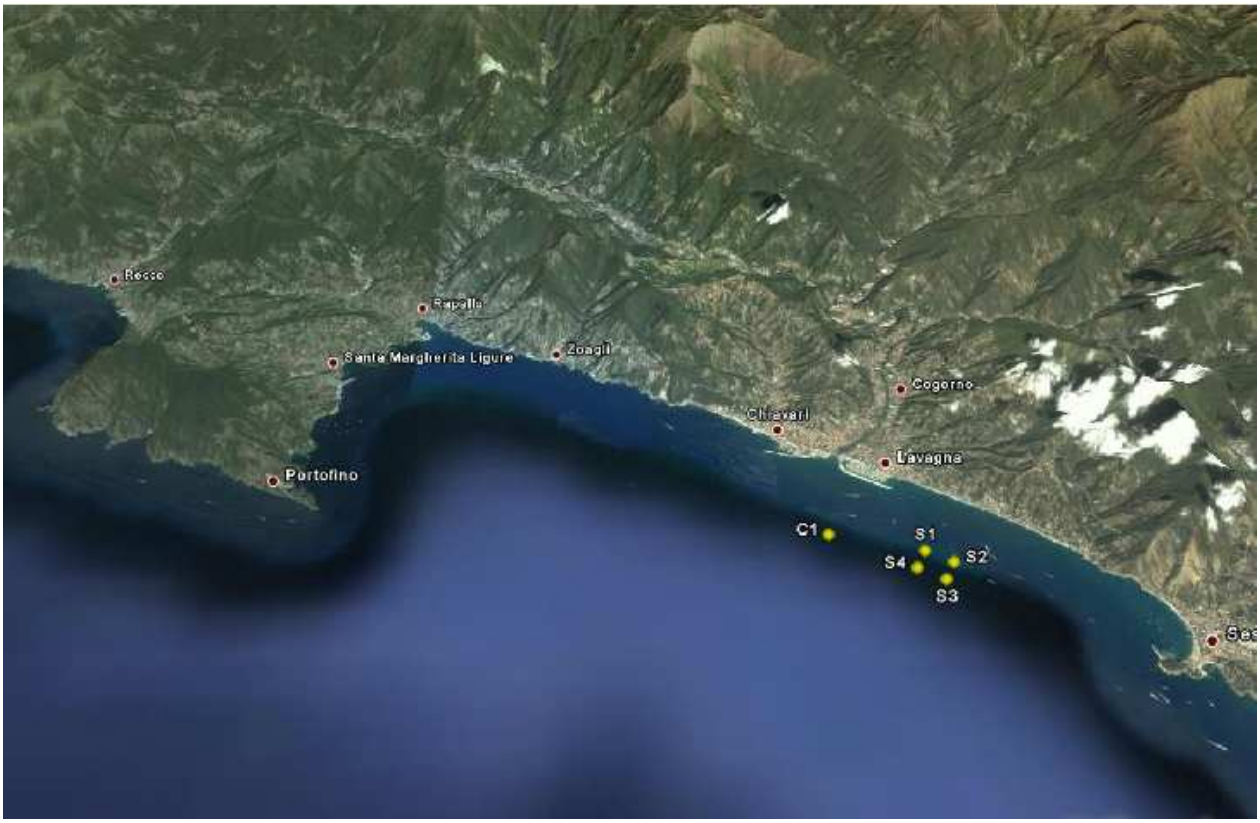

Figure 3.3: Location of the four sampling stations for collection of experimental data near the net-pen system and location of the current meter C1.

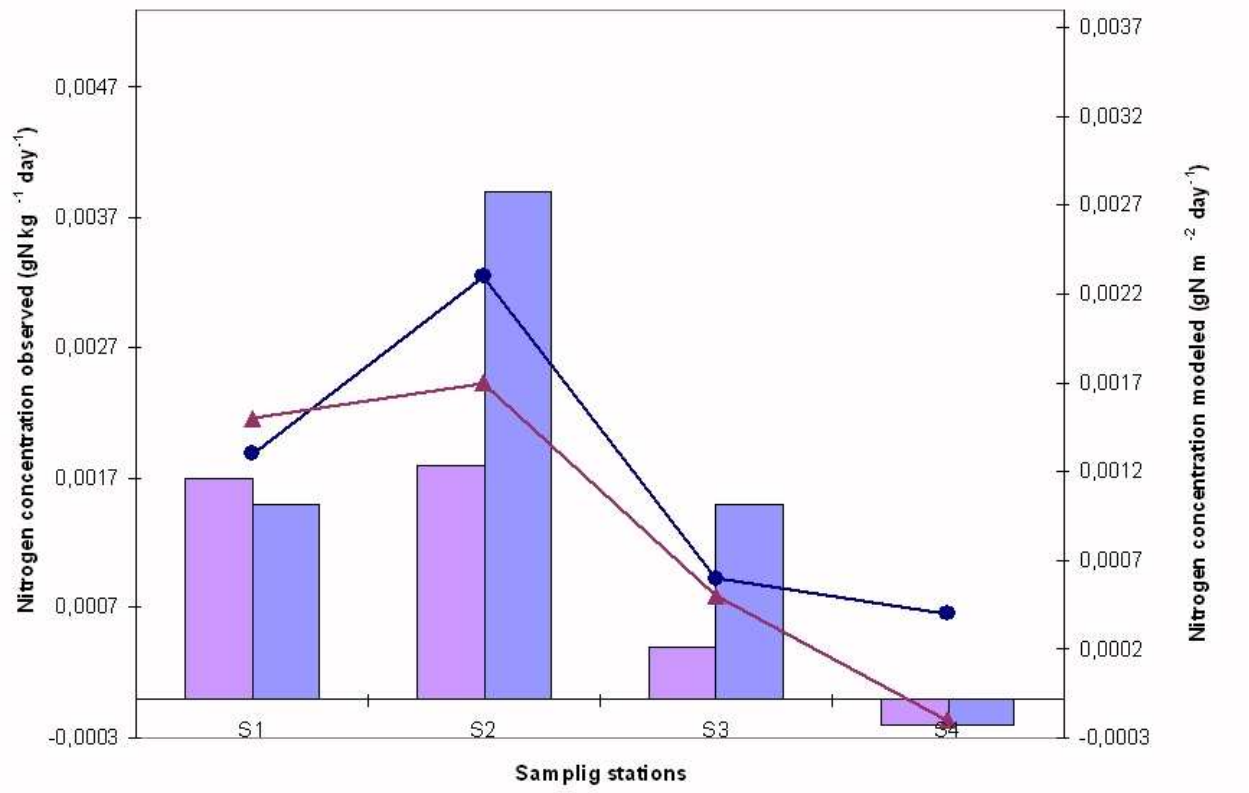

Figure 3.4: Daily nitrogen loading rate observation in gN kg^{-1} day^{-1} (light violet bar is referred to 2000-2005 data, dark violet bar to 2000-2002 ones) and modeled in gN m^{-2} day^{-1}(magent line is referred to FOAM outputs, blue line to Doglioli et al. (2004b) ones) in the four sampling stations around the fish farm.

the slowly sinking values are indicated with a single arrow pointing toward the bottom (↓), while the quickly sinking values with a double one (⇓).

Results from the benthic module are presented in relation to (i) the extension of the impacted area, (ii) the position of this area in terms of its barycenter, (iii) the benthic trophic conditions and (iv) the predicted organic concentration at the barycenter. The choice of these parameters allows the simple and objective estimation of the degree and the location of the potential impact.

The impacted area is the sum of the areas of the grid meshes where particles are still present even after the benthic degradation activity. The position of the barycenter (x_b, y_b) of this area is basically a position weighted by the number of particles left in each cell after the degradation. It is simply expressed as

$$x_b = \frac{\sum_{j=1}^{N} \sum_{i=1}^{M} i \cdot n_{i,j}^{left}}{n_{Tot}^{left}} \tag{3.6}$$

$$y_b = \frac{\sum_{j=1}^{N} \sum_{i=1}^{M} j \cdot n_{i,j}^{left}}{n_{Tot}^{left}} \tag{3.7}$$

where M and N are the numbers of meshes in the x and y directions, $n_{i,j}^{left}$ is the number of particles left on the bottom in the mesh (i, j) and $n_{Tot}^{left} = \sum_{j=1}^{N} \sum_{i=1}^{M} n_{i,j}^{left}$ is the total number of particles left on the bottom after the degradation. The benthic trophic condition and the predicted organic concentration at the barycenter are simply given by the parameter I and $Conc^{bot}$ in the grid mesh corresponding to the barycenter position.

Initially, the effects on the extension of the impacted area are described. Fig. 3.5 shows the time series of the calculated extensions in the different experiments and the temporal variations of the modeled current velocity near the cages (Fig. 3.5D).

The slowly sinking feed particles continuously released (Fig. 3.5A, solid black line) are dispersed by the current a little bit more than the quickly sinking ones (dashed red line). This is also confirmed by the time averages and the standard deviations for the experiments A1 and A2 (see Table 3.4). The situation changes when periodical release is considered (Fig. 3.5B). In this case both slowly and quickly sinking particles are dispersed on a larger area than in the continuous case. However, while for slowly sinking particles this area is much larger and less variable in time than in the continuous release, for quickly sinking ones, the area is just a little bit bigger and more variable (see Table 3.4). The variability of the dispersion is therefore associated with the current velocity and it increases both with periodical release and with decreasing settling velocity values.

For faecal pellets (Fig. 3.5C), the impacted area is smaller than in the previous cases. Moreover, faecal wastes show greater time variability than the uneaten feed, no matter what the feed release is. The slowly sinking faecal particles impact smaller areas with respect to the quickly sinking ones, and also the variability is smaller than the quickly sinking ones (Table 3.4).

Fig. 3.6 gives a better visualization of what has been stated so far and, at the same time, it shows the position of the barycenter of the impacted area. In this figure, the extension of the impacted area is schematized with a circle centered in the barycenter and having an area equivalent to the one already calculated. The colored scale represents the time evolution of the results every sixty days (blue represents the initial time, green the final one), while a circle is drawn every ten days. In the case of feed, for both continuous and periodical releases, the barycenter of the impacted area is found at approximately 25 m southwestward from cages. For the same simulations, a less significant time variability is observed (Fig. 3.6A1, A2, B1 and B2) and this means that the impacted area is always larger and that higher stress levels are expected.

In the case of faecal wastes, instead, the barycenter shows greater time variability, according to changes in current direction and intensity (Fig. 3.6C1 and C2). This variability results in a dispersion of the faecal particles in different areas and therefore lower stress levels are expected.

To better emphasize these results, we can look at the scatter diagram of the parameter I at the barycenter position in time (Fig. 3.7). For clarity, all values greater than 2 are artificially assigned to 2 in this figure. For feed particles continuously released (Fig. 3.7A), I mainly stays in the non-stressed range (i.e. $I > 1.5$),

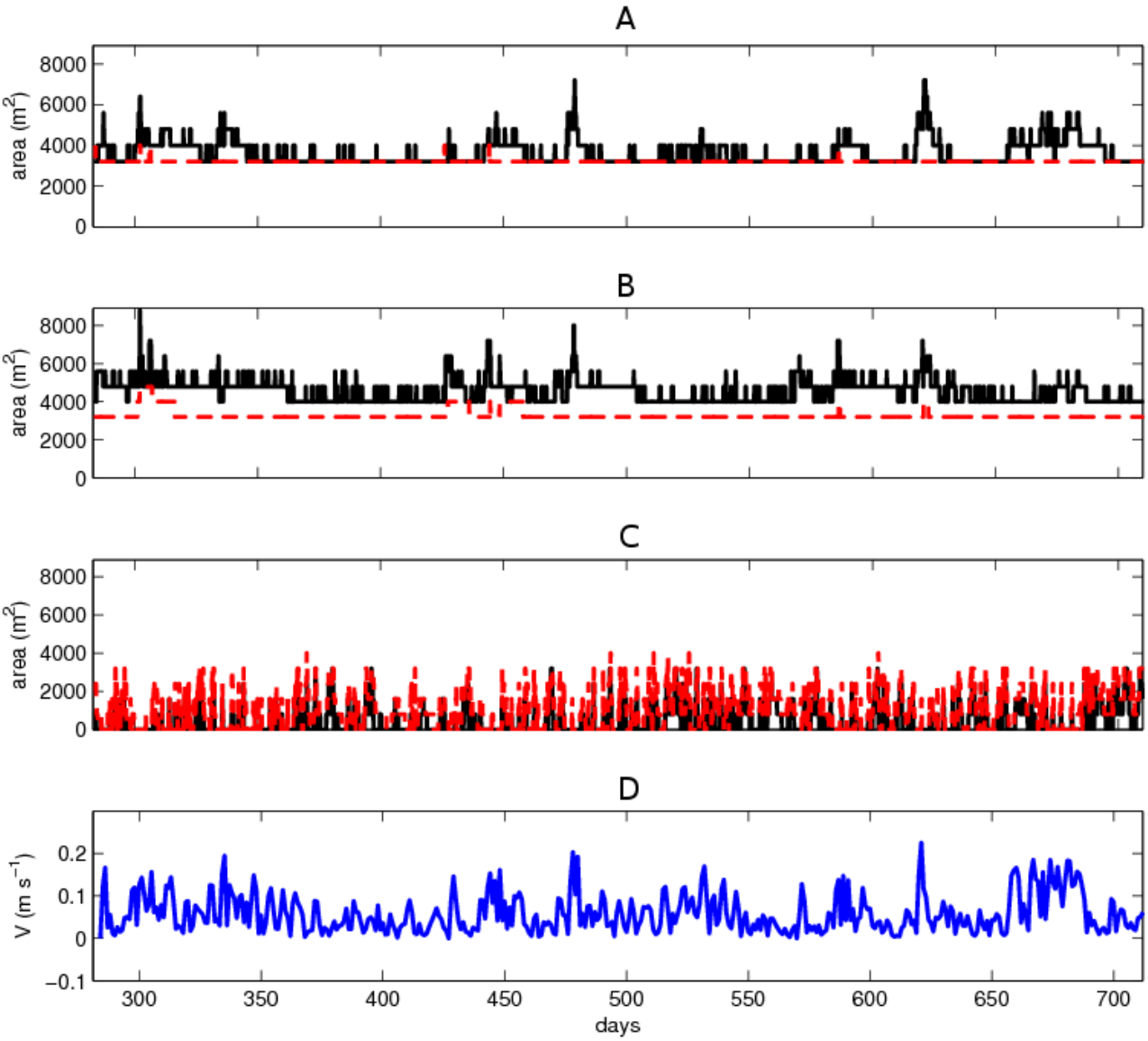

Figure 3.5: Time series of impact area for: A) continuously released feed pellets B) periodically released feed pellets C) faeces and D) computed current velocity near cages. Solid black line represents slowly sinking wastes, dashed red line quickly ones.

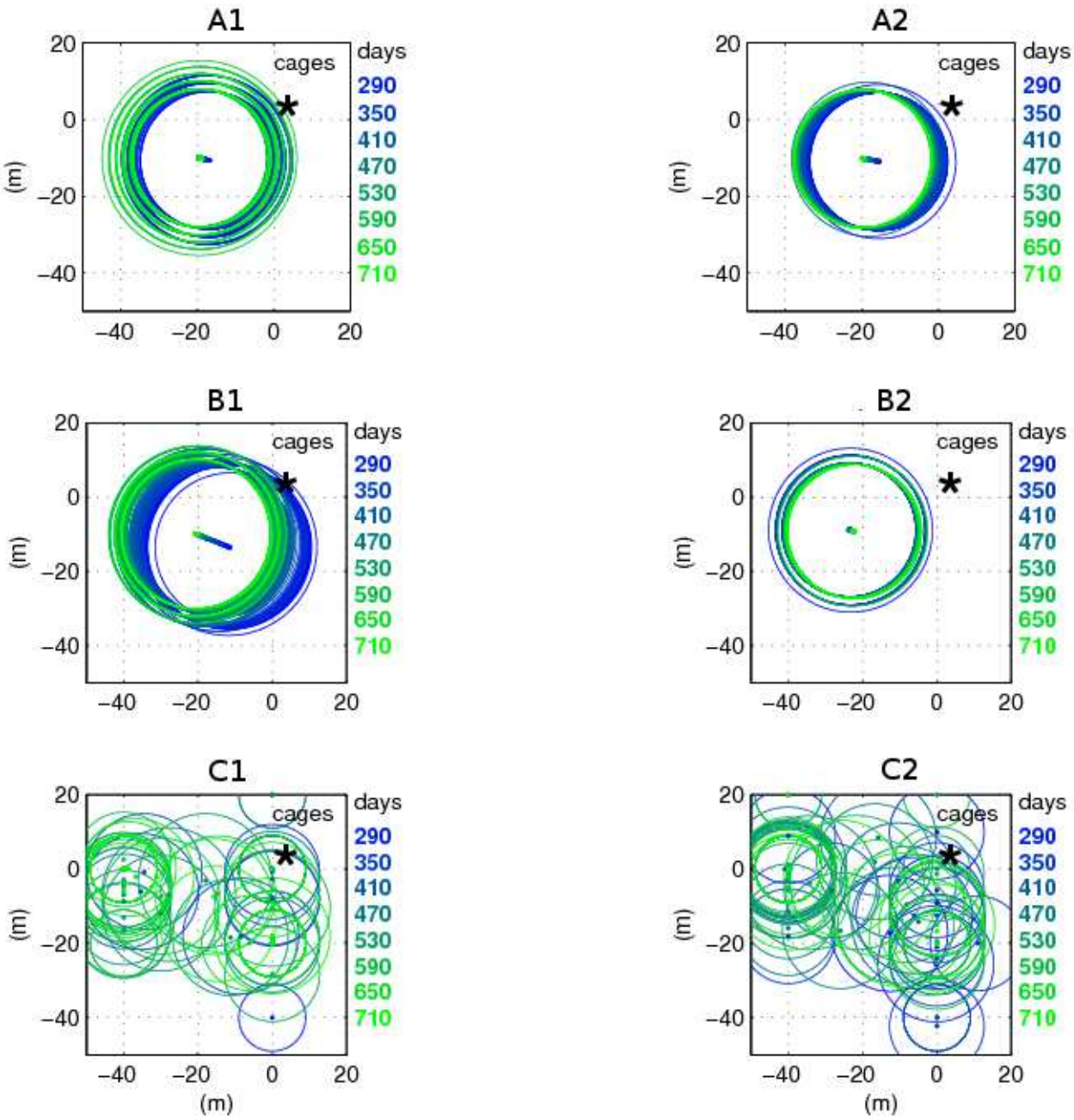

Figure 3.6: Time trend of impact area (circles) and barycenter (dots). A) continuously released feed pellets B) periodically released feed pellets C) faeces. Left column slowest particles and right column fastest particles of each kind of waste. In the adopted schematization the area of circles is equivalent to the impact area. Colored scale represents the time evolution of the results every sixty days (blue represents the initial time, green the final one), while a circle is drawn every ten days.

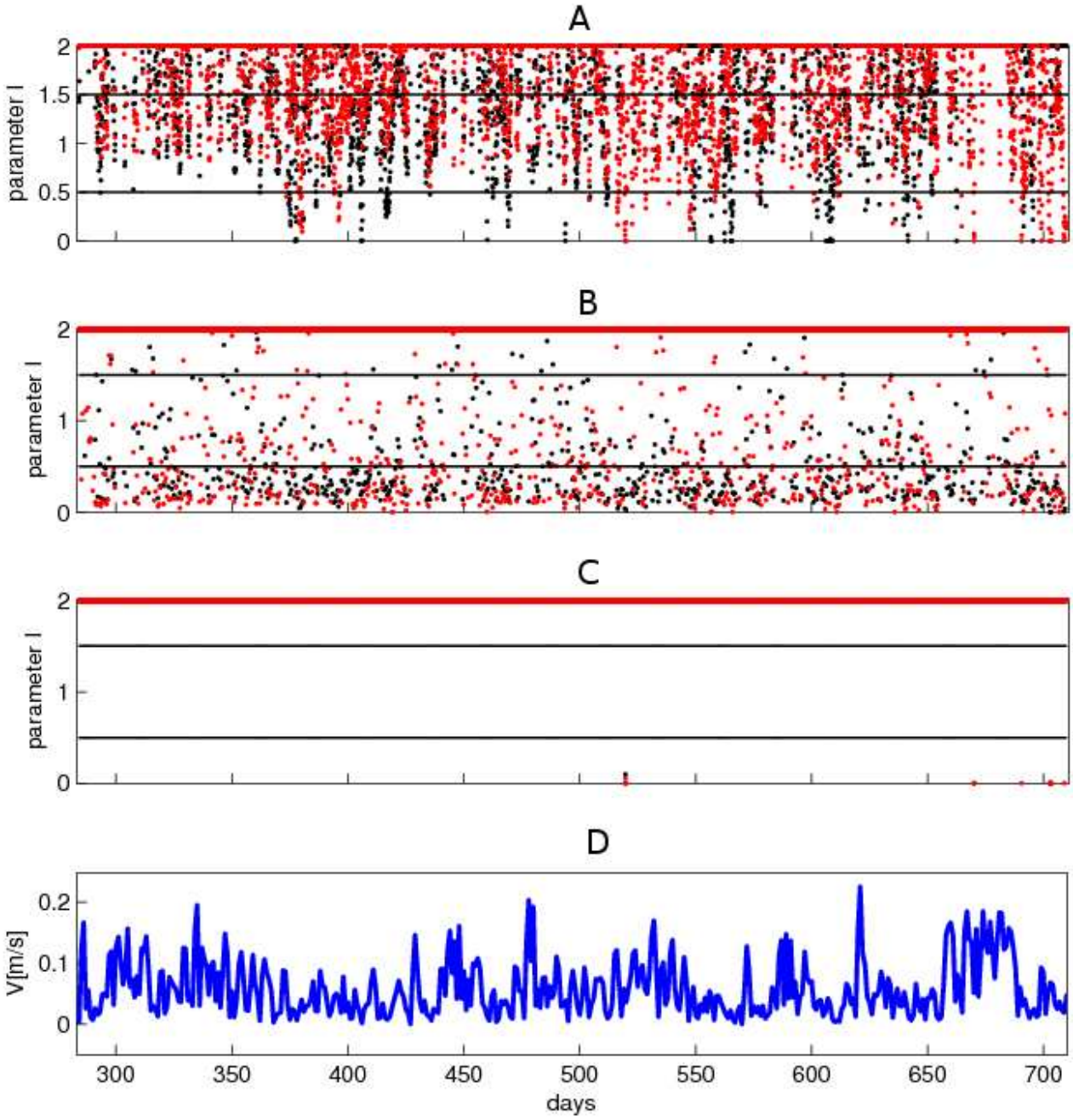

Figure 3.7: Spread diagram of the parameter I at the barycenter position. All values greater than 2 are fixed to 2. A) continuously released feed pellets B) periodically released feed pellets C) faeces D) current velocity near cages. The black dots are used to slowest particles, red ones to fastest particles of each kind of waste. The black lines represent the stress level thresholds.

sometimes goes up to the intermediately-stressed range, but the highly-stressed level is rarely reached. There is a slight tendency for quickly sinking particles to stay more in the intermediate regime than the slow ones (Table 3.4). For periodical release (Fig. 3.7B), I is often in the non-stressed range, very rarely in the intermediately-stressed range but it reaches the highly-stressed level more frequently than before. An easy and quick check shows that the highly-stressed values are registered, in this case, in the period going from 2 to 4 hours after the release. No significant difference can be observed between slowly and quickly sinking particles.

For faecal wastes (Fig. 3.7C), the parameter I is practically always greater than 2 (for this reason in the plot all dots are squeezed in the top) for both slowly and quickly sinking particles.

Finally, the mean values of the computed organic matter concentration $Conc^{bot}$ remaining on the seabed at the barycenter position after the degradation are reported in the last column of Table 3.4. The organic carbon amount due to feed waste almost linearly increases with time and the maximum values are reached in the case of the most quickly sinking feed particles in periodical release.

The faecal waste instead seems to be completely degraded and it does not contribute to organic carbon concentration at the bottom.

All the results are summarized in Table 3.4.

Exp.	**Simulation typology** (release)	**Impacted area** mean $\pm$ std (m^2)	**Parameter *I*** stress (% days) no	medium	high	**Organic concentration** mean $\pm$ std (gC m^{-2})
A1	Slow feed (continuous)	3576 ± 582	74	22	4	1450 ± 404
A2	Quick feed (continuous)	3202 ± 41	71	27	2	1490 ± 453
B1	Slow feed (periodical)	4513 ± 563	87	4	9	895 ± 380
B2	Quick feed (periodical)	3277 ± 266	88	4	8	1590 ± 387
C1	Slow faeces	377 ± 656	99	0	1	< 1
C2	Quick faeces	941 ± 962	99	0	1	< 1

Table 3.4: Time-averaged impacted area, benthic trophic conditions and organic concentrations at the barycenter position for the different experiments.

3.3 Discussion

The new model setup is shown to better reproduce both the hydrodynamics and the dispersion in the investigated area. This is mainly due to the new forcing which is based on current meter data and leads to more realistic results. As already remarked in previous works (Findlay and Watling, 1997; Morrisey et al., 2000),

current direction and intensity strongly influence the position of the impacted area and the degradation of the settled matter. Nevertheless, the processes involved are strongly non-linear and it is difficult to assess the role played by each parameter in the model.

When particles sink relatively quickly (settling velocities are one order of magnitude less than the current velocity, as a lower limit) the impacted area does not vary and the barycenter position depends on the main direction of the current. Instead, for relatively slowly sinking particles, the variability of the current starts to play a major role. This different behavior explains why the barycenter of the uneaten feed remains practically motionless, while the one for the faeces is very mobile.

At the same time, current intensity reduces bottom degradation thanks to two different processes. On one hand, a stronger current brings more oxygen to the sediment and makes degradation more efficient. On the other hand, the same stronger current increases waste dispersion resulting in a wider impacted area and in lower waste concentrations on the bottom. Faeces do not contain much organic carbon and the strong degradation is able to remove almost all the settled matter. Uneaten feed contains more organic carbon and sinks more rapidly than faeces. As a result, much more carbon accumulates on the sea floor and it is only partially degradated even in presence of strong currents. This also explains the observed small variability of the size and position of the impacted area.

Since the settling velocity values used for faeces are measured by Magill et al. (2006), it is particularly interesting to compare our results with theirs. In order to do this, I calculated the accumulation rates in the barycenter for different sinking faeces. Values of 11 g faeces m^{-2} $year^{-1}$ and 19 g faeces m^{-2} $year^{-1}$ for slowly and quickly sinking particles are obtained, respectively. These values are about two orders of magnitude smaller than the ones reported in Magill et al. (2006). Two arguments can be provided to explain this discrepancy. Firstly, the total fish biomass in the cages is not reported in Magill et al. (2006) and this does not allow for a correct quantitative comparison. The policy of the fish farm here studied is to keep low biomass per cage (Roberto Co', AQUA s.r.l., personal communication). It is likely that the Greek fish farm studied by Magill et al. (2006) has a high biomass value per cage. Secondly, with the new module FOAM, we introduced the degradation of the settled organic carbon which is not considered instead by Magill et al. (2006). However, since I adopted the degradation rates proposed by Findlay and Watling (1997) for Atlantic fish farm, it is also possible that these values are too high with respect to the Mediterranean ones. Unfortunately, until now, no values of the mineralization rates for the Mediterranean fish farm are available in literature.

On the other hand, our results agree with the work of Magill et al. (2006) in predicting a greater impact for the faeces of *D. Labrax* respect to *S. Aurata*'s ones. The same results also agree with previous studies and confirm the uneaten feed to be the primary cause of ecological impact on the benthos community (Beveridge et al., 1991; Vezzulli et al., 2003).

For this reason, I studied in more detail the feed release conditions. I found that a release occurring twice a day results in i) more frequent conditions of highly-stressed sediments and ii) larger impacted areas than a continuous release. These results support the idea already proposed in previous studies of using self-feeders to reduce the uneaten feed loss without affecting fish growth rates (Azzaydi et al., 1998, and references therein).

3.4 Conclusions

Aquaculture is the food-related activity with the most rapid growth in the world. Since this growth produces an immediate concern, it is necessary to develop tools to predict the environmental impacts coming from intensive marine fish farms.

In this chapter, the improvements on the capability of the POM-LAMP3D model have been shown . These include both a more realistic advection-dispersion setup and a new benthic model, the Finite Organic Accumulation Model (FOAM). Using the empirical relations put forth by Findlay and Watling (1997), FOAM calculates the organic carbon degradation for three different levels of sediment stress. Several runs are performed to simulate different scenarios by varying waste typology (faecal or feed), settling velocity of particles (on the basis of feed dimensions, fish size and reared species) and release conditions of feed (periodical or continuous).

At the same time, the same runs allowed to test the stability of the model which appears very satisfactory.

More satisfactory results for the hydrodynamics and dispersion are obtained than in Doglioli et al. (2004b). Moreover, FOAM revealed its ability to simulate different scenarios by switching suitable parameters.

The results presented in relation to the extension of the impacted area and the position of its barycenter show that the continuously released feed settles within a narrow area near the cages (impact area maximum 6500 m^2; barycenter shifting amplitude 10 m; cages maximum distance 25 m); while the feed released twice a day spreads on a larger area centered near the cages (maximum area 8500 m^2; barycenter shifting amplitude 15 m; cages maximum distance 25 m). Faecal pellets accumulate on a smaller area within a greater and more variable range from the cages (maximum area 4000 m^2; barycenter shifting amplitude 100 m; cages maximum distance more than 50 m) with respect to uneaten feed. Maximum impacts, in terms of both stress parameter I and organic carbon concentration are due to the quickly settling feed, released in periodical mode and during slow current periods. Some mitigation of the impact is observed if feed is continuously released. The use of self-feeders has therefore been suggested to the farmers.

To further improve the prediction capability of the model, the results highlighted that specific in-situ measurements are required for evaluate the values of the mineralization rates in Mediterranean conditions.

4

FOAM Re-parameterisation by *in situ* measurements

In the previous chapter, we have seen as the mineralization rates and benthic metabolism values are key parameters for the aquaculture impact model. Therefore, the lack in literature of these data for Mediterranean conditions influences the accuracy of the prediction capability of the degradation model. For this reason, two sampling campaigns have been performed during 2006 in a Mediterranean fish farm. In particular i) we measured the carbon flux to the sediment and the surface sediment respiration rate under floating cages for Sea Bass and Sea Bream rearing; ii) we differentiated the sea floor into a three-state categorization according to measured variations in the respiratory quotient and iii) we estimated per each sediment state, the different rates of organic matter degradation through CO_2 production. In this mode, we can fill this gap by re-parameterizing FOAM with data from the *in situ* measurements.

The resulting newly re-parametrized version of FOAM has been applied to the studied area presented in the previous chapter (Fig. 3.1), and the same numerical experiments are performed in order to allow a better comparison of the numerical results uniquely introducing variations in the parametrization of FOAM for the benthic metabolism modelling. In this regard, recall that different types of released waste coming from the cages (i.e. uneaten feed and faecal pellets) are considered. Moreover, different settling velocity values measured specifically in the Mediterranean conditions (for the feed Vassallo et al., 2006; Magill et al., 2006, for the faecal pellets) are employed considering the maximum and the minimum values of settling velocity both for feed and for faeces (Table 3.2). Faecal pellets release is simulated considering a continuous release. While, for the feed release, two different typologies are considered: continuous release, as the feed self-serviced, or periodical release, as the feed is supplied manually by an operator twice in a day.

4.1 Experimental field

The *in situ* measurements were aimed to:

i) measure carbon flux to sediment;

ii) determine three different benthic states below and around the fish farms and

iii) estimate, for each sediment state, the rates of organic matter degradation.

Survey campaigns were performed in 2006 in the *Tortuga srl.* off-shore fish farm located in the Manfredonia Gulf in the South Adriatic Sea (Fig. 4.1). The farm is composed of 16 floating cages for the rearing of Gilthead Sea Bream (*Sparus aurata*) and Sea Bass (*Dicentrarchus labrax*) and has a production of about 650 ton year^{-1}. The sea cages are located at about 3 km from the coast on a water column ranging from 8 to 12 m. For its features (reared species, farm dimensions and yearly production), this farm can be considered a typical Mediterranean off-shore fish farm (Basurco and Lovatelli, 2003; UNEP/MAP/MED, 2004; Dalsgaard

Figure 4.1: Fish farm location and sampling station positions.

and Krause-Jensen, 2006). Moreover, this site allows to measure, in a relatively small area, sediments characterized by quite different loads of organic carbon and associated microbial activities. The expected large range of C input, benthic O_2 and CO_2 fluxes allows to collect in the Mediterranean Sea a reliable set of data.

During the pre-survey activity carried out in May 2006, thirty stations along a transect in the direction of the main water current were investigated for organic matter content in sediment. Successively in order to reduce costs but cover a broad range of conditions (i.e. heavily to moderately organic load), six sampling stations (Fig. 4.1) were chosen between the thirty ones and investigated in July and October 2006.

At each of the six stations, the water temperature was measured by means of a multiparametric probe (YSI, mod 556), which has got an accuracy of 0.001°C. Moreover, three sediment traps were deployed at about 1 m from the bottom. These traps were left *in situ* for 48 hours. After recovery, trap sample portions were filtered on fiberglass membranes (Whatman GF/F diameter 25 mm, nominal porosity 0.45 μm) by a vacuum pump, with pressure not exceeding 25 kPa to avoid particles breaking on the filter and matter loss in the dissolved phase. In order to determine the carbon flux to the sediment (φ_C mmolC m^{-2} d^{-1}), the recovered material was then analyzed for particulate carbon by a CHN elemental analyzer (mod. CHNS-O EA 1108, Carlo Erba).

Respiration rates and inorganic carbon production were measured by means of intact cores incubation. To this purpose, sediment cores (i.d. 0.08, length 0.40 m, n = 4) were collected in the six sampling stations by scuba divers. All cores were brought to the laboratory within a few hours from sampling for further processing and incubation procedures, described in detail in Dalsgaard et al. (2000). The day after the sampling, the water in the tank was exchanged and the cores incubated in the dark at the same *in situ* temperature for measuring dissolved oxygen flux (φ_{O_2} mmolO_2 m^{-2} d^{-1}) and total inorganic carbon flux (φ_{CO_2} mmolCO_2 m^{-2} d^{-1}). Water samples were collected at regular time intervals with plastic syringes. Samples for φ_{O_2} determinations were transferred to glass vials (Exetainers, Labco, High Wycombe, UK) and Winkler reagents were added immediately (Stigebrandt et al., 2004). Samples for φ_{CO_2} were also transferred to glass vials and immediately titrated with 0.1 N HCl following the Gran procedure (Anderson et al., 1986).

In order to evaluate the status of the sampled sediment, the respiratory quotient *RQ* was computed. The respiratory quotient is defined as the ratio between measured total inorganic carbon and dissolved oxygen fluxes, as suggested by Dilly (2003):

$$RQ = \frac{\varphi_{CO_2}}{\varphi_{O_2}} \tag{4.1}$$

On the basis of the calculated *RQ*, three categories of sediment states was defined as in Table 4.1. The rationale behind this classification is that along a gradient of organic enrichment, the relative proportion of aerobic to anaerobic degradation changes, with implication for the accumulation of reducing power at the sediment level (Therkildsen and Lomstein, 1993; Boucher et al., 1994; Hargrave et al., 2008).

Sediment states	**RQ values**
$\alpha \Longrightarrow$ Limited organic load	RQ < 0.8
$\beta \Longrightarrow$ Moderate organic load	$0.8 <$ RQ < 1.2
$\gamma \Longrightarrow$ Elevated organic load	RQ > 1.2

Table 4.1: Sediment state identification as a function of sediment respiratory quotient (*RQ*).

4.2 Results

4.2.1 Experimental field results

The variation range (minimum, maximum and average value) of carbon flux to the sediment φ_C, oxygen demand φ_{O_2} and total inorganic carbon flux φ_{CO_2} measured in the six sampling stations during July and October campaigns are reported in Table 4.2. Moreover, the Atlantic values collected by Findlay and Watling (1997) are also reported.

			min	**max**	**mean ± std**
φ_C (mmolC m^{-2} d^{-1})	July		1.3	60.6	23.4 ± 26.0
	October		8.8	106.9	60.3 ± 38.7
	Atlantic		80	540	310.0 ± 141.4
φ_{O_2} (mmolO_2 m^{-2} d^{-1})	July		32.7	144.5	88.2 ± 43.4
	October		36.2	100.9	56.4 ± 23.0
	Atlantic		55.4	561.4	308.4 ± 155.6
φ_{CO_2} (mmolCO_2 m^{-2} d^{-1})	July	α	3.6	87.2	45.1 ± 26.8
		β	56.2	80.2	68.2 ± 16.9
		γ	140.9	242.2	188.6 ± 47.1
	October	α	0.2	94.1	31.1 ± 27.7
		β	20.7	66.2	47.8 ± 21.3
		γ	44.2	141.8	89.9 ± 34.8
	Atlantic	α	10.9	57.1	27.5 ± 15.2
		β	12.9	106.3	57.5 ± 38.4
		γ	18.8	53.6	30.6 ± 17.8

Table 4.2: Ranges of carbon flux to the sediment (φ_C), oxygen demand to the sediment (φ_{O_2}) and carbon dioxide emissions from sediment (φ_{CO_2}) detected in the two sampling campaigns and in the Atlantic conditions.

The carbon flux to the sediment φ_C measured in July is smaller than in October (t-test, $p < 0.01$). While, the oxygen demand φ_{O_2} and the respiration rates φ_{CO_2} in July assessed greater values than in October (t-test, $p < 0.01$). The same metrics measured by Findlay and Watling (1997) in Atlantic fish farm displayed higher values in terms of carbon fluxes to the sediment (t-test, $p < 0.01$) and oxygen demand (t-test, $p < 0.01$), but Atlantic sediment showed lower average degradation capability assessing lower values of respiration rates than Mediterranean values in the three sediment states even if significant differences are only found for elevated organic load sediment conditions (t-test, $p < 0.01$).

It is important to note that, as stated by Findlay and Watling (1997), the equation for the oxygen supply, Eq. (3.1), may be considered *robust across a variety of geographical or hydrological regions* universally valid, while the oxygen demand one, Eq. (3.2), is strongly dependent on environmental conditions where the organic matter is accumulated. Hence, only the relationship between oxygen demand φ_{O_2} and carbon flow to the sediment φ_C is evaluated and displayed in Fig. 4.2.

Unlike to what showed for Atlantic conditions (dashed gray line), in Mediterranean Sea the relationship between φ_{O_2} and φ_C results affected by changes in water temperature. Both sampling campaigns show a positive relationship between φ_{O_2} and φ_C. In July (October) experiment, when the water temperature is around 27°C (18°C), the molar ratio is 1.4 (0.4) and the y-intercept is 54.5 (31.8). These values are adopted for the parameters C and D in Eq. (3.2).

Since temperature deeply affected the oxygen demand by the sediment, we analyzed the benthic metabolism rate separating data from the two sampling campaigns. In Fig. 4.3A (B), the data of φ_{CO_2} measured in July (October) are reported in relation to φ_{O_2}. These data are grouped according to the three categories of sediment state based on the *RQ* (Table 4.1), in order to determine the average mineralization rate per sediment

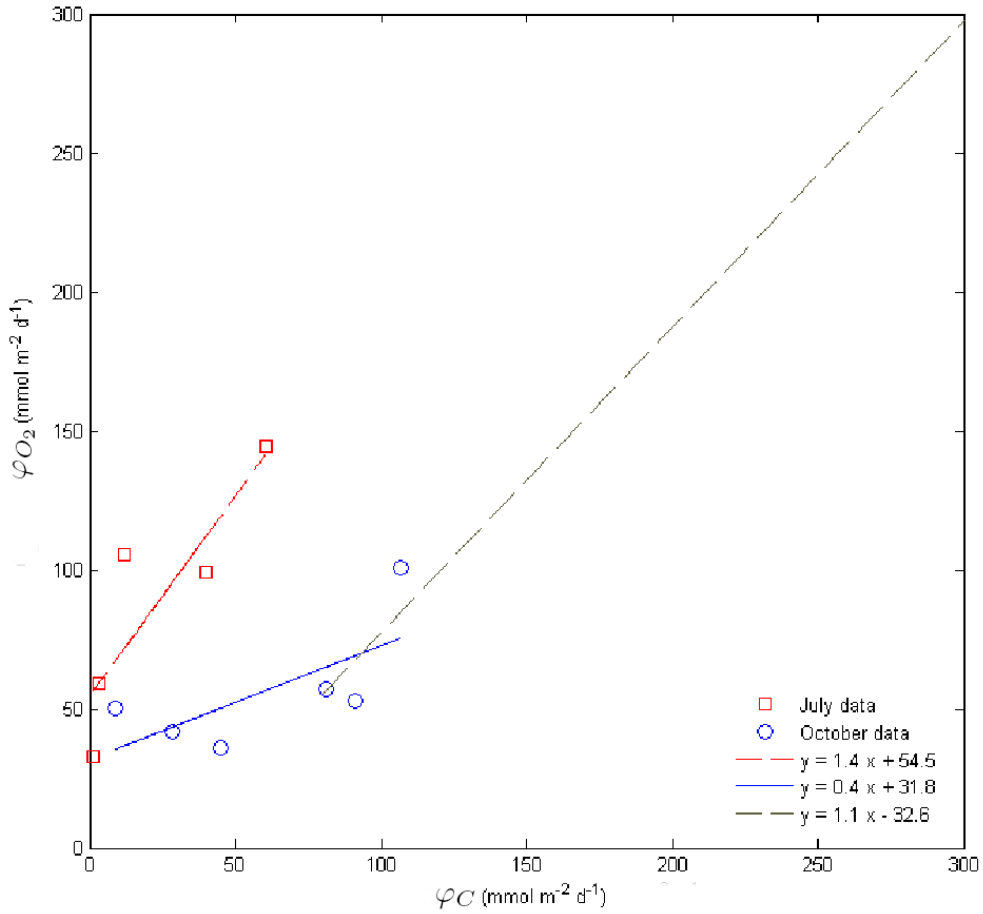

Figure 4.2: Relationships between the carbon flux to the sediment (φ_C) and the benthic metabolism as measured by O_2 consumption (φ_{O_2}). Solid blue line identifies the general trend of October samplings (○); dashed red line identifies the general trend of July samplings (□) and dotted gray line follows the trend assessed by Findlay and Watling (1997).

state and per sampling campaigns. The variation range of φ_{CO_2} for each state and campaign is summarized in the lowest part of Table 4.2.

FOAM assumes the degradation capability of sediment to be equal to the mean values of φ_{CO_2} for each sediment state and campaign (lowest part of the last column of Table 4.2 and big black crosses and stars in Fig. 4.3). For every sediment state, the mineralization rates measured in July are higher than ones measured in October.

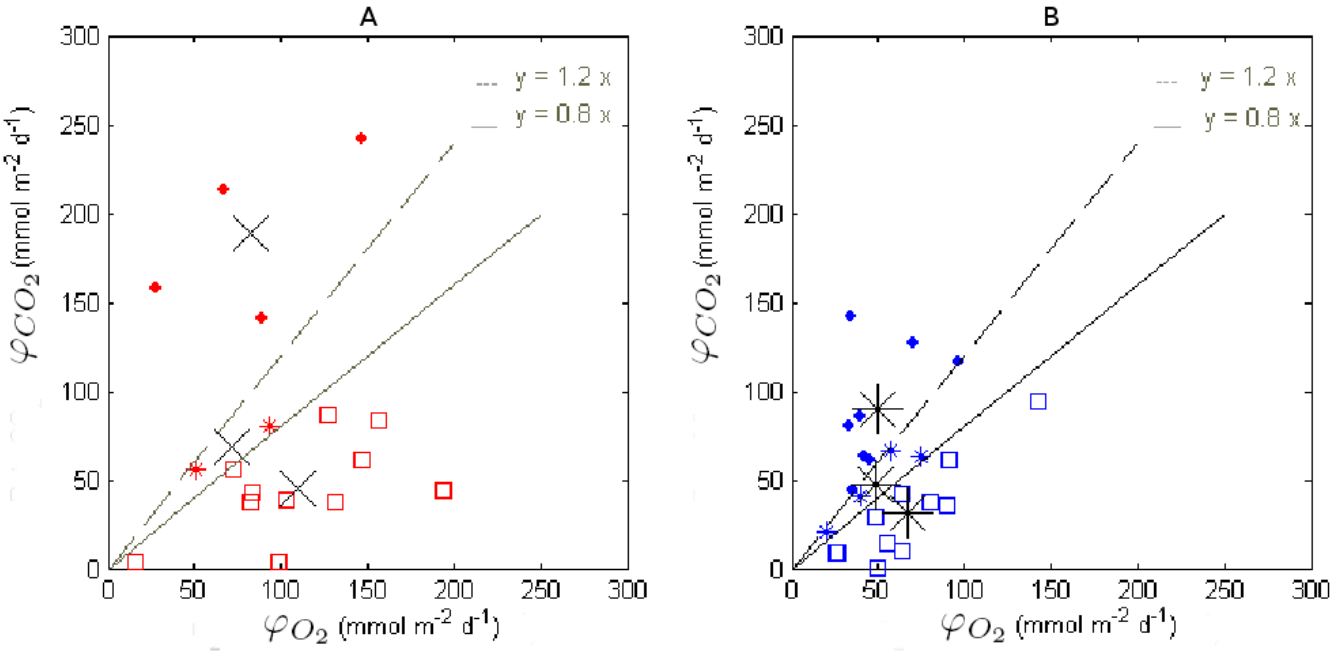

Figure 4.3: Relationship between measured dissolved oxygen flux (φ_{O_2}) and total inorganic carbon flux (φ_{CO_2}). A) July data; B) October data. Solid and dashed gray lines identify the threshold of limited and elevated organic load states of sediment ($RQ < 0.8$ and $RQ > 1.2$), respectively. • represent elevated, $\star$ moderate and □ limited organic load data. Big black crosses and stars represent the average mineralization rate per sediment state.

4.2.2 Numerical results

In the light of the obtained experimental results, two different scenarios have been simulated considering the parameter values obtained from July and October *in situ* experiments, respectively (Table 4.3).

For the two simulated scenarios, the simulation results are presented, as in the previous chapter, in relation to i) the extension of the impacted area, defined as the whole area where particles are still present even after the benthic degradation activity; ii) the organic carbon concentration, defined as the carbon quantity per impacted square meter of sediment and iii) the occurrence of the different categories of sediment states. For a direct comparison, the tables (Table 4.4, Table 4.5 and Table 4.6) show the new results together with the previous chapter ones in which we have been considered the Atlantic setup.

Largely, the impacted area is always smaller than in Atlantic setup. In the July setup smaller impacted areas are registered with respect to the October one (Table 4.4 and Fig. 4.4). A negligible impact is always associated to fish faeces compared to uneaten feed. For the slowly sinking feed particles both in periodical and in continuous release (Exp A1 and B1), the impacted area is always larger than for the quickly sinking ones. The slowly sinking feed particles released in periodical mode (Exp. B1) results in the widest impacted area.

FOAM benthic parametrization	**July**	**October**	**Atlantic**
O_2 demand parameter, C ($mmolO_2$ $mmolC^{-1}$)	1.4	0.4	1.1
O_2 demand parameter, D ($mmolO_2$ m^{-2} d^{-1})	54.5	31.8	-32.6
Mineralization rate in α state (mmolC m^{-2} d^{-1})	45.1	31.1	27.5
Mineralization rate in β state (mmolC m^{-2} d^{-1})	68.2	47.8	57.5
Mineralization rate in γ state (mmolC m^{-2} d^{-1})	188.6	89.9	30.6

Table 4.3: FOAM benthic parametrization as reported by Findlay and Watling (1997) for Atlantic conditions and as obtained for July and October in Mediterranean conditions.

IMPACTED AREA				
Exp.	**Simulation Typology (release)**	**July setup** mean $\pm$ std (m^2)	**October setup** mean $\pm$ std (m^2)	**Atlantic setup** mean $\pm$ std (m^2)
A1	Slow feed (continuous)	3393 $\pm$ 419	3521 $\pm$ 540	3576 $\pm$ 582
A2	Quick feed (continuous)	3200 $\pm$ 22	3202 $\pm$ 35	3202 $\pm$ 41
B1	Slow feed (periodical)	4118 $\pm$ 605	4451 $\pm$ 542	4513 $\pm$ 563
B2	Quick feed (periodical)	3245 $\pm$ 203	3268 $\pm$ 251	3277 $\pm$ 266
C1	Slow faeces	<1	51$\pm$ 200	377 $\pm$ 656
C2	Quick faeces	5 $\pm$ 59	342 $\pm$ 525	941 $\pm$ 962

Table 4.4: Time-averaged impacted area at the bottom for the different experiments considering July, October and Atlantic parameterizations.

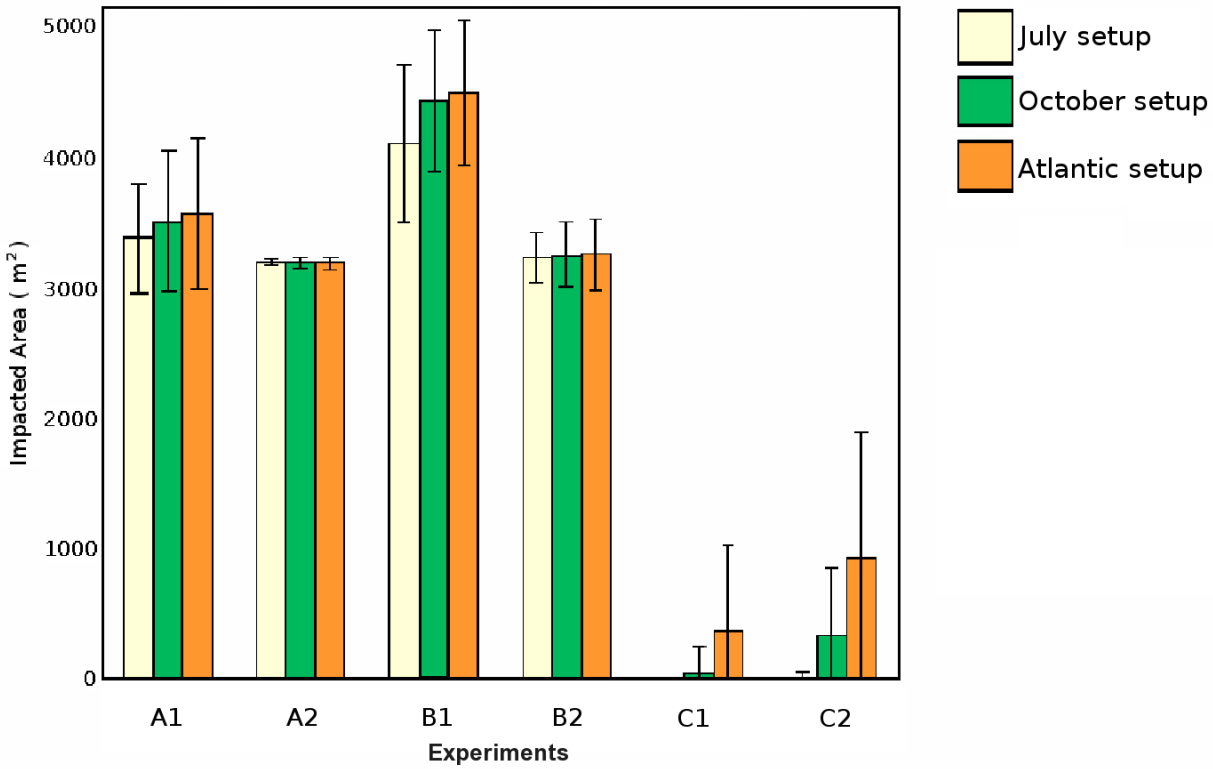

Figure 4.4: Time-average of impacted area for the different experiments considering July (white bar), October (green bar) and Atlantic (orange bar) setup. The vertical lines represent the standard deviations.

In all scenarios, the faeces result completely degraded (Table 4.5 and Fig. 4.5). The slowly sinking feed particles released in periodical mode (Exp. B1) result in the smallest organic carbon concentration. The quickly sinking feed particles release in the periodical mode (Exp. B2) result in the greatest organic carbon accumulation. The predicted organic carbon concentration due to the uneaten feed in the July setup is always smaller than in the October one. Moreover, with the exception of the quickly sinking feed particles released in the periodical mode (Exp. B2), the organic carbon concentration in the October setup is greater than in the Atlantic one.

ORGANIC CARBON CONCENTRATION				
Exp.	**Simulation Typology (release)**	**July setup** mean $\pm$ std (gC m^{-2})	**October setup** mean $\pm$ std (gC m^{-2})	**Atlantic setup** mean $\pm$ std (gC m^{-2})
A1	Slow feed (continuous)	1301 ± 357	1464 ± 408	1450 ± 404
A2	Quick feed (continuous)	1353 ± 417	1551 ± 464	1490 ± 453
B1	Slow feed (periodical)	1075 ± 331	1226 ± 372	895 ± 380
B2	Quick feed (periodical)	1405 ± 340	1560 ± 379	1590 ± 387
C1	Slow faeces	<1	<1	<1
C2	Quick faeces	<1	<1	<1

Table 4.5: Time-averaged organic carbon concentrations remaining at the bottom after degradation for the different experiments considering July, October and Atlantic parameterizations.

As expected in the above-mentioned results, for C1 and C2 experiments the sediment is practically always in the limited organic load category (Table 4.6 and Fig. 4.6). Considering the uneaten feed, in the October setup, the day occurrence of moderate and elevated organic load sediment states is lower than in the other scenarios. While in the July setup, the moderate and elevated organic load sediment states are higher. In all simulated scenarios, the maximum occurrence of the elevated organic load sediment state is due to the feed released in periodical mode (Exp. B1 and B2).

As in the previous chapter, the modelled average carbon flux on the seabed (gC m^{-2} d^{-1}) in the four stations around the farm (Fig. 3.3) are considered and compared with the *in situ* measurements. In Fig. 4.7, the modelled average carbon flux for the simulated scenarios with Atlantic and Mediterranean conditions are reported, for a direct comparison. Moreover the outputs of the setup used by Doglioli et al. (2004b), in which they do not considered the benthic degradation model, are reported.

The *in situ* measurements of carbon flux (gC $kg^{-1}d^{-1}$) are also reported (Fig. 4.7, bar). As already explained, a comparison between the absolute values of model outputs and *in situ* data is not possible because, in order to express both of them in the same units, strong assumptions on sediment density and sampling methodology have to be inferred. Hence, Fig. 4.7 shows the agreement between the field and modelled data. In particular, the measured carbon flux toward the sediment is highest in station S2 and lowest in S4 in agreement with all model outputs. Considering the degradation model the modeled results are in best agreement with the *in situ* data than considering Doglioli et al. (2004b) setup (continuous dark blue line). The higher degradation rates of the July setup result in the lowest values of organic matter flux to the bottom (continuous magent line). On the other hand, the October setup (dashed blue line) shows highest carbon fluxes only in the stations with the greatest organic accumulation (S1 and S2). These trends are in a better agreement with the measured pattern of accumulation with respect to the Atlantic setup (dashed black line).

This is also confirmed by the correlation values between *in situ* and modelled data (Table 4.7). Data are significantly correlated (n=5, $p < 0.01$) but Mediterranean parametrization (mainly July parametrization) allows higher correlation coefficient revealing better fit between model and real trends.

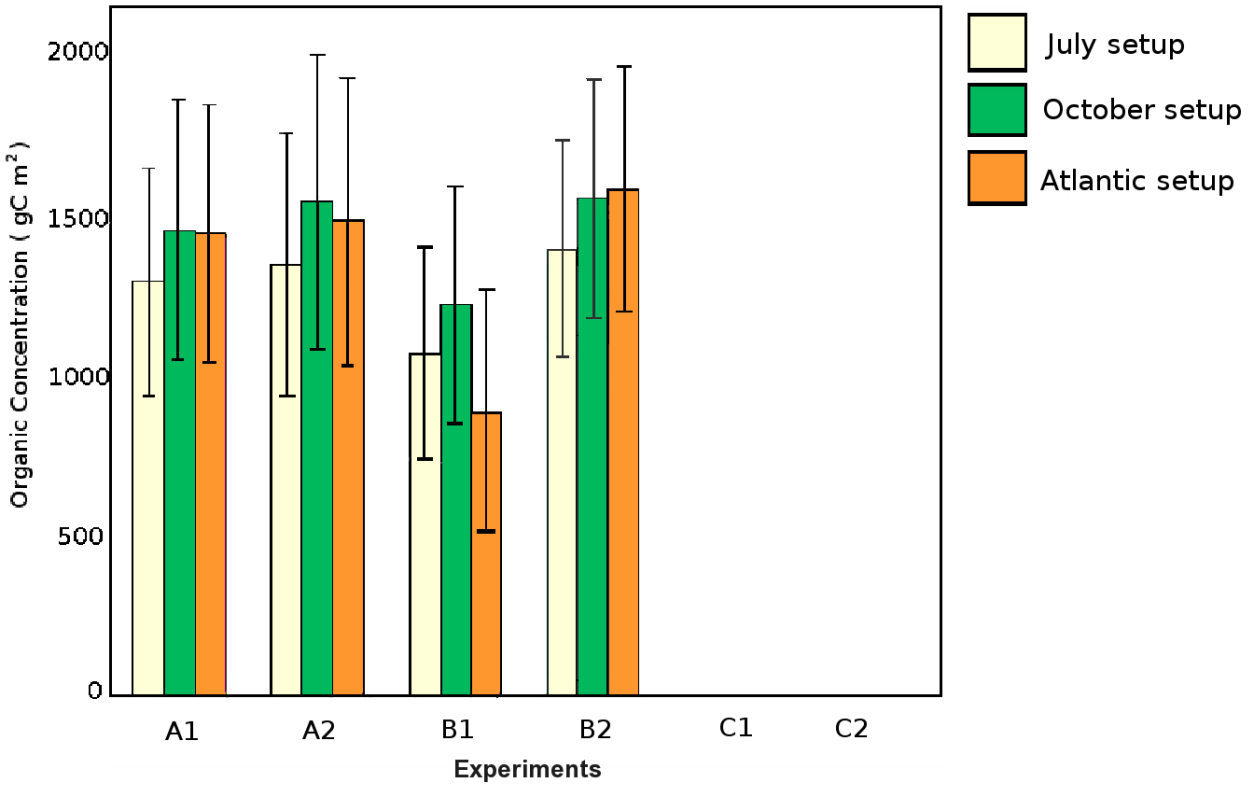

Figure 4.5: Time-average of organic carbon concentration for the different experiments considering July (white bar), October (green bar) and Atlantic (orange bar) setup. The vertical lines represent the standard deviations.

OCCURRENCE OF DIFFERENT SEDIMENT STATES										
Exp.	**Simulation Typology (release)**	**July setup** states (%days)			**October setup** states (%days)			**Atlantic setup** states (%days)		
		α	β	γ	α	β	γ	α	β	γ
A1	Slow feed (continuous)	49	44	7	94	5	1	74	22	4
A2	Quick feed (continuous)	43	52	5	96	3	1	71	27	2
B1	Slow feed (periodical)	85	4	11	89	8	3	87	4	9
B2	Quick feed (periodical)	86	4	10	90	6	4	88	4	8
C1	Slow faeces	100	0	0	100	0	0	99	0	1
C2	Quick faeces	100	0	0	99	1	0	99	0	1

Table 4.6: Time-occurrence of the benthic states for the different experiments considering July, October and Atlantic parameterizations.

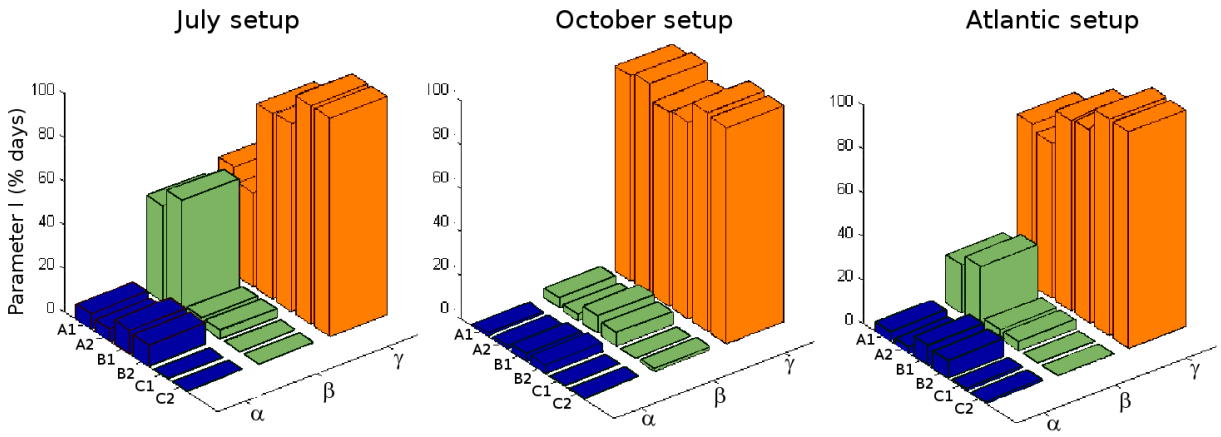

Figure 4.6: Time-occurrence of the different benthic states, α elevated (blue bar), β moderate (green bar) and γ limited (orange bar) organic load, for every experiment and setup.

CORRELATION VALUES	
	in situ data
in situ data	1
July setup	0.9994
October setup	0.9989
Atlantic setup	0.9958
Doglioli et al. (2004b) setup	0.9601

Table 4.7: Correlation values between *in situ* and modelled data of daily organic carbon loading rate in the four sampling stations around the fish farm.

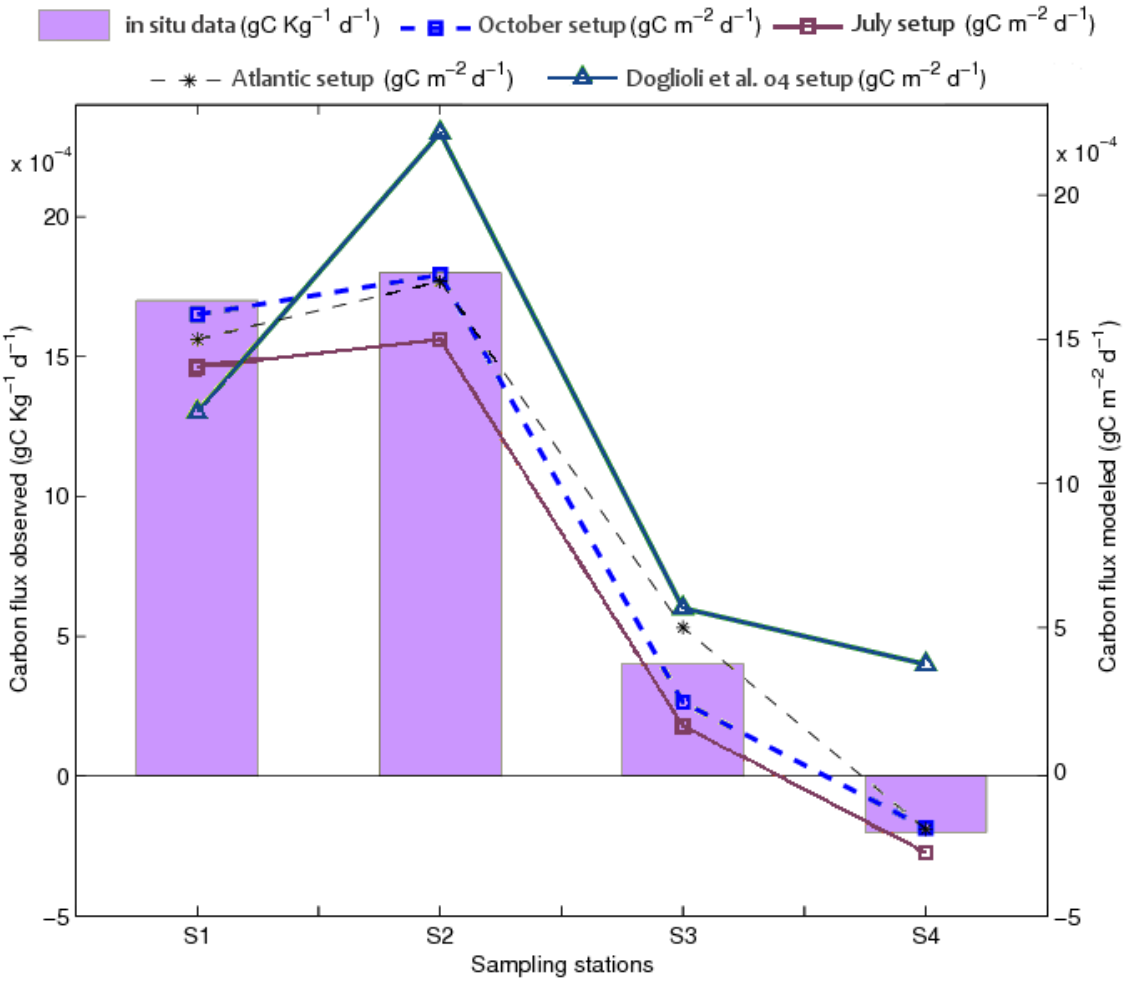

Figure 4.7: Daily organic carbon loading rate in the four sampling stations around the fish farm. Data from sampling observation are reported in gC kg^{-1}d^{-1} and are referred to 2000-2005 (light violet bar). Results obtained by FOAM simulations with the three applied settings are reported in gC m^{-2}d^{-1}: July (magent), October (blue) and Atlantic (black) setup. Doglioli et al. (2004b) setup outputs (dark blue) in gC m^{-2}d^{-1} are also reported.

4.3 Discussion

The values of carbon flux to the sediment measured using sediment traps range between 1.3 and 107.0 mmol m^{-2} d^{-1} and include the range reported for other Mediterranean areas with cage fish farming (1 - 45 mmol m^{-2} d^{-1} Pusceddu et al., 2007). Despite significantly higher than background sedimentation, such organic carbon flux to the sediment (φ_C) is anyway moderate and does not result in excess oxygen demand at the benthic level. Respiratory quotients, calculated from φ_{O_2} and φ_{CO_2}, are in fact quite below those reported for more sheltered and organic rich Mediterranean coastal lagoons, where anaerobic mineralization rates play a major role in the overall microbial respiration activity (Bartoli et al., 2005).

One of the main assumptions behind the calculation, which is the linearity between oxygen demand and carbon input, is thus likely to be satisfied. In the previous chapter, we have been considered the Atlantic data, where organic carbon flux is significantly higher and range between 80 to 550 mmol m^{-2} d^{-1} (Findlay and Watling, 1997). This is not surprising as Mediterranean fish farms are generally smaller in comparison with the Atlantic ones and able to produce lower quantities of fish per year. Differences in the carbon flux can be also due to the employed feed: the new generation feed has, in fact, increased floating properties (Vassallo et al., 2006), allowing fish to better exploit the provided pellets and therefore minimizing wastes. Despite the fluxes of organic matter to the sediment tend to be lower than in Findlay and Watling (1997), experiments A1 and A2 indicate, for more than 50% of the simulated period, a moderate to elevate organic enrichment state of the benthic compartment. This is possible because the area, in which the measurements are performed, near the coast and relatively shallow, is characterized by weak currents regime which means in turn a moderate supply of oxygen to counterbalance respiratory needs. The relationship between the carbon flux to the sediment and the oxygen consumption found by Findlay and Watling (1997), is here re-evaluated for the Mediterranean aquaculture average conditions. Mediterranean temperature variations force this relationship. Two different linear trends are assessed during July and October sampling campaigns. The July trend implies greater values of oxygen demand than in Findlay and Watling (1997), while the October one shows lower. This is not surprising and has been recently reviewed by Guld (2008), who shows how measurements of oxygen demand coupled to carbon input to the sea floor are still very limited. He also underlines the need for seasonal studies, as it is likely that carbon sedimentation and oxygen respiration rates are probably partially uncoupled. Organic carbon sedimentation, measured via traps, is in fact a sort of instantaneous measurement whilst oxygen demand reflects and integrates the occurrence of processes with a longer time scale (Guld, 2008). With equal carbon flux to the sediment and water circulation regime, the higher oxygen demand of July setup forces the model towards a larger occurrence of the moderate organic load conditions (β category of sediment state) compared to the Atlantic setup. The opposite is observed in October setup when the occurrence of an elevated re-oxidation of anaerobic metabolism end-products (limited organic load condition) increases.

The mineralization rates result higher than what previously assessed by Findlay and Watling (1997) apart from the October setup intermediate organic load state that shows lower ability to degrade organic load. Moreover, the mineralization rates measured in July are the highest. This gives rise to higher degradation and consequently lower organic accumulation on the bottom and smaller impacted area than in the other scenarios.

Therefore, the new parameters allow a better discrimination between the two scenarios evidencing the temperature-dependence of the processes involved. This dependence also influences the impact typologies: July is characterized by a more frequent occurrence of moderate and elevate organic load and by a higher degradation causing lower organic carbon concentration on the sea bed and smaller impacted area. Managers and policy makers may take care of these differences in planning the installation of new fish-farms or the expansion of existing ones. A balance among the organic matter spread or load and the occurrence of different sediment states may be accurately evaluated with the application of the model.

4.4 Conclusions

The new FOAM simulations are shown to better reproduce the nutrient load on the seabed in the investigated area than considering the Atlantic setup. The new setup which is based on the Mediterranean benthic

metabolism, leads to more realistic results. The obtained results confirm what already assessed in previous chapter: the feed particles are the primary cause of ecological impact to the benthos community and the more frequent conditions of high sediment stress level and the higher values of organic carbon concentration on the seabed are due to the feed particles released in periodical mode (twice in a day). Furthermore, the new results highlight that water temperature is a key parameter for the simulation of the responses of the marine environment to organic load. In fact, during the July setup the sediment is more likely to show the occurrence of disturbed states. However the impact, in terms of concentration and extension, is reduced thanks to the increased ability to mineralize organic loads (resilient ecological system). On the contrary, in the October setup, undisturbed sediment states and a lower ability to mineralize organic matter are registered. This leads to higher concentrations and higher impacted areas on the benthos (resistant ecological system).

It is important to note that the entire model framework is driven by the circulation model. Additionally, it influences the dispersion of the waste and the state of the sediment, as already underlined in the previous chapter. For this reason, in the next chapter, I focus the attention on the improvements of the coastal circulation model. In particular, in order to increase the reliability of the circulation model, I find that the wind is the main forcing of the circulation in the area under study and, then, I evaluate its effect on the circulation.

5

Effects of wind forcing and its resolution on coastal circulation

The importance of the wind speed and wind stress curl on the formation of basin-scale gyres is already shown by several authors as Moskalenko (1974); Malanotte-Rizzoli and Bergamasco (1989, 1991); Herbaut et al. (1996); Pinardi and Navarra (1993). More recently, Molcard et al. (2002) shows that the wind forcing can generate upper ocean gyres of observed structure and strength. As the wind forces the coastal circulation, the interaction between the wind and the coastal topography, such as headlands and capes, is shown to have a strong effect on shallow water hydrodynamics (e.g. Castelao and Barth, 2007, 2006). In particular, topographically-induced changes in wind speed and wind stress curl are usually associated with flow variability, formation and growth of instabilities around promontories. Moreover, the coastal circulation is highly influenced by the shape of the coastline. Leeward eddies are observed behind topographic structures like prominent headlands and capes (e.g. Pattiaratchi et al., 1986; Farmer et al., 2002; McCabe and Pawlak, 2006). These eddies have a strong impact on the dynamics of coastal systems, playing a role in biological, ecological, and geological processes. Leeward eddies affect the dispersion of dissolved pollutants (Hayward and Mantyla, 1990; Doglioli et al., 2004b; De Gaetano et al., 2008), floating organisms (Chiswell and Roemmich, 1998; Roughan et al., 2005; Rankin et al., 1994; Murdoch, 1989), nutrients (John and Pond, 1992), and sediments (Pingree, 1978; Bastos et al., 2002, 2003; Jones et al., 2006). From a dynamical point of view, capes and headlands are important for the circulation because they are associated with enhanced mixing, drag and dissipation (Farmer et al., 2002; Pawlak et al., 2003). All the processes usually observed around capes, like current separation, formation of eddies and generation of lee waves, also affect the larger-scale coastal currents through the enhancement of the drag force.

A very large branch of the scientific literature focuses on the phenomenon of coastal current separation and eddy formation behind capes, in terms of experimental, numerical and theoretical investigations (e.g. Boyer and Tao, 1987; Freeland, 1990; Geyer, 1993; Denniss et al., 1995; Sadoux et al., 2000). Some of these studies, which mainly regard the effect of islands on the flow, focus on the limit of very deep water (e.g. Coutis and Middleton, 2002). However, most of the literature focuses on the eddy formation in shallow-water environments, where vertically averaged 2-dimensional dynamics is an appropriate approximation (e.g. Verron et al., 1991; Davies et al., 1995), often considering highly energetic, time-dependent tidal currents and idealized smooth cape structures (Signell and Geyer, 1991). The present chapter follows this kind of mathematical approach. In particular, I want to study the relation between wind forcing and eddy formation as a function of the wind flow resolution. The importance of the wind forcing is recognized by many authors, but its effect on the coastal circulation is not quantified yet. Moreover, complex orography in coastal area can strongly influence the local wind (Esposito and Manzella, 1982) and the associated oceanic circulation. These features are present in the studied coastal area, i.e. the Promontorio of Portofino. Indeed, this is blunt headland with an abrupt rising from the ocean with very steep slopes. Moreover, this area has a great importance both for tourism and commercial activities as well as for its great natural environmental value. As already reminded, since 1998 the cape and its surroundings have been declared Marine Protected Park, with the intent of preserving the coastal and marine ecosystem. Many political and social conflicts

have arisen since then, due to the contrast between the high tourist pressure and the need for a sustainable management of natural resources (Salmona and Veradi, 2001). In this framework, an understanding of the local coastal circulation and its impact on the transport of pollutants deriving from antrophogenic activities (e.g. Aliani et al., 2003; Doglioli et al., 2004b; De Gaetano et al., 2008) is of great importance in order to correctly manage the maritime an coastal areas of the park.

For these reasons in this chapter, several numerical simulations of the coastal model in the investigated area are performed considering different resolutions of wind model. Particularly, I want to understand the orography effect on the wind and the repercussion on coastal circulation and eddy formation. As it is well known, the coastal ocean is one of the most challenging marine environment to understand and to model (e.g. Haidvogel and Beckmann, 1999). Results are often significantly sensitive to parameterization choices and parameter values (e.g. Pérenne et al., 2001), so that there is a real need for systematic testing and comparisons of numerical model results. So, I compare the results also varying the drag coefficient values considering a constant value or a value depending on wind speed.

In this framework, the present investigation is expected to provide a contribution in two different directions. On the one hand, it will contribute to our understanding of the rule played by the wind resolution for resolve coastal circulation and eddy generation mechanism in presence of shelf and steep slope. On the other hand, it will provide indications on the appropriate model configuration and parameter ranges to be used as a basis for future realistic modelling of the specific area.

Moreover, considering the peculiarity of the studied area, a cluster analysis of the wind and of the current is performed in order to evaluate the typical wind and current regimes.

5.1 Numerical and statistical methods

The outputs of two versions with two different horizontal resolutions of the atmospheric model are used to force the coastal ocean model. In the following, an overview of the main characteristics of these models and their interaction is given (section 5.1.1 and 5.1.2), while for a more detailed description, see appendix A (section A.4 and A.1, respectively). Moreover, in section 5.1.3 the methodology adopted to perform the cluster analysis is shortly described.

5.1.1 Atmospheric modelling setup

The atmospheric model BOLAM (BOlogna Limited Area Model) is a hydrostatic primitive equation meteorological model, developed at the Institute of Atmospheric Sciences and Climate (ISAC) of the Italian National Research Council (CNR) of Bologna (Buzzi et al., 1994). It is used for weather forecasting at the Meteo - Hydrological Centre for Civil Protection (CFMI-PC) of the Ligurian Region, at the Department of Physics of the University of Genoa, and at the National Observatory of Athens. It is a grid point, hydrostatic model in sigma coordinates, computing zonal and meridional wind components, potential temperature, specific humidity and surface pressure as prognostic variables. Horizontal discretization adopts the Arakawa C-grid, while the vertical discretization is of Lorenz type, with a variable spacing such as to give higher resolution near the surface and, to a smaller extent, near the tropopause. The boundary-layer scheme parameterizing momentum, latent and sensible heat turbulent fluxes at the surface is based on the drag coefficient formulation. Exchange coefficients are represented by analytic formulae dependent on the Richardson number and on the roughness and mixing lengths (Louis et al., 1982).

Surface roughness length is different for momentum and latent-sensible heat over land. It is also dependent on orography height in order to parameterize aerodynamic drag. Charnock's (1955) formula is used to parameterize roughness length over sea and is the same for both momentum and heat parameters. Geleyn (1988) vertical interpolation scheme is used to find wind at 10 m height using surface pressure and the wind, temperature and specific humidity at the lowest model level and at the surface. A fourth-order horizontal diffusion term (for numerical stability) based on the spatial operator is added to all prognostic equations except for the tendency of surface pressure (Buzzi et al., 1998). This procedure, adopted by all numerical modelers, has strong impact on surface wind, leading to a systematic underestimation of the wind speed (Chèruy et al., 2004). For more details, see section A.4 of appendix A.

For the time period of the present analysis, namely from January 2001 to December 2003, two versions of this model running at CFMI-PC with different computational domain (Fig. 5.1) and horizontal resolutions are used:

- a coarser version covering all the western Mediterranean basin with a horizontal resolution of 21 km (BOLAM 21 hereafter), running with analysis and forecasts of the ECMWF operational model as initial and boundary conditions;
- a finer version covering the Northern Italy with a horizontal resolution of 7 km (BOLAM 7 hereafter), one-way nested into the BOLAM 21 version.

Both models provided the wind forcing to the ocean model with a time-step of three hours (at 00, 03, ..., 21 UTC).

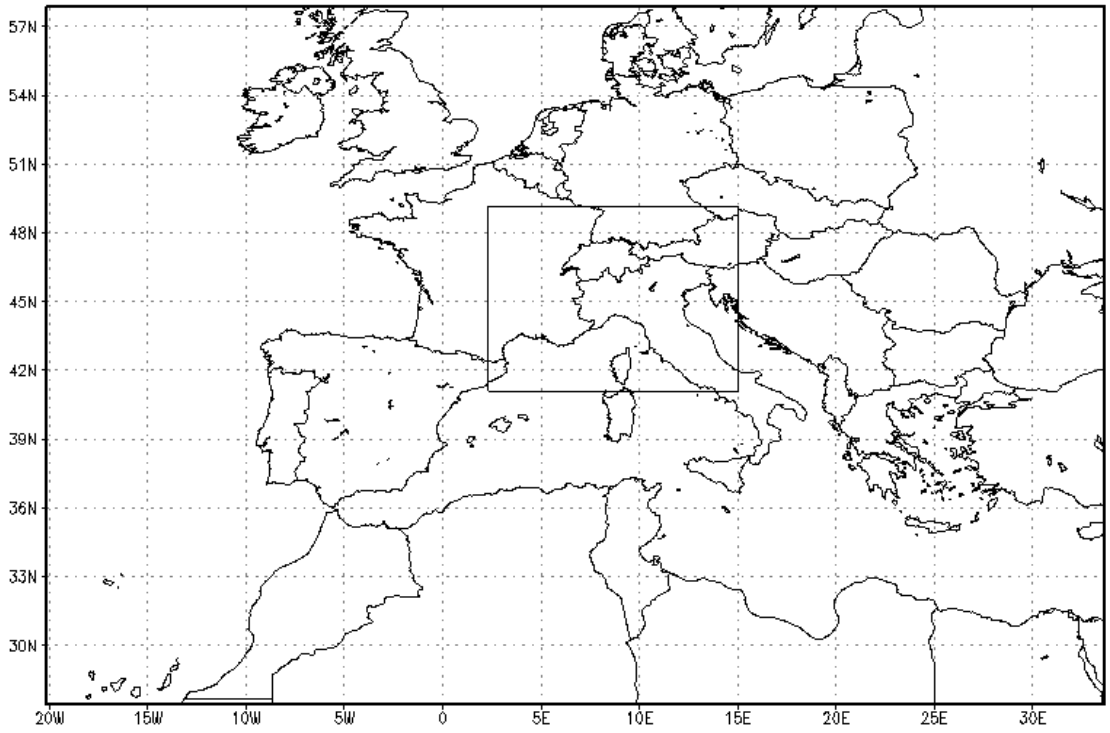

Figure 5.1: BOLAM 21 domain and within the black rectangle BOLAM 7 domain. BOLAM 7 is one way nested into BOLAM 21.

5.1.2 Coastal ocean modelling setup

The coastal-circulation high-resolution numerical model POM (Blumberg and Mellor, 1987), in its barotropic version, is used to simulate the circulation around the Promontorio of Portofino (Fig. 5.2). As already see in section 3.1, POM is a primitive equation, free surface, sigma coordinate ocean model, based on Boussinesq and hydrostatic approximations. Sigma coordinates are particularly useful in coastal applications because they resolve bottom boundary layer processes. In our implementation, the horizontal components of depth-averaged current are computed on an Arakawa-C grid and the vertical turbulence closure is based on the Mellor and Yamada (1982) model. For more details, see section A.1 of appendix A.

Since the primary focus of this study is to assess the effect of wind resolution on coastal currents and since the circulation in this area is mainly barotropic (Bruschi and Manzella, 1980; Astraldi and Manzella, 1983), we choose to consider the barotropic version of the POM model.

The numerical mesh, rotated by 27 degrees anti-clockwise with respect to the true north, consists of 200 x 100 grid points. The coastline and bathymetry data were downloaded on the web site `http://rimmer.ngdc.noaa.gov/mgg/coast/getcoast.html` and `http://pdas.navo.navy.mil`, respectively. The horizontal resolution varies in the numerical domain: a finer resolution of 500 m is used in the area closer to the headland to better resolve the dynamics around Portofino.

In Fig. 5.2 the POM domain is shown and following the Doglioli et al. (2004a) setup, a buffer zone for the boundary condition is considered.

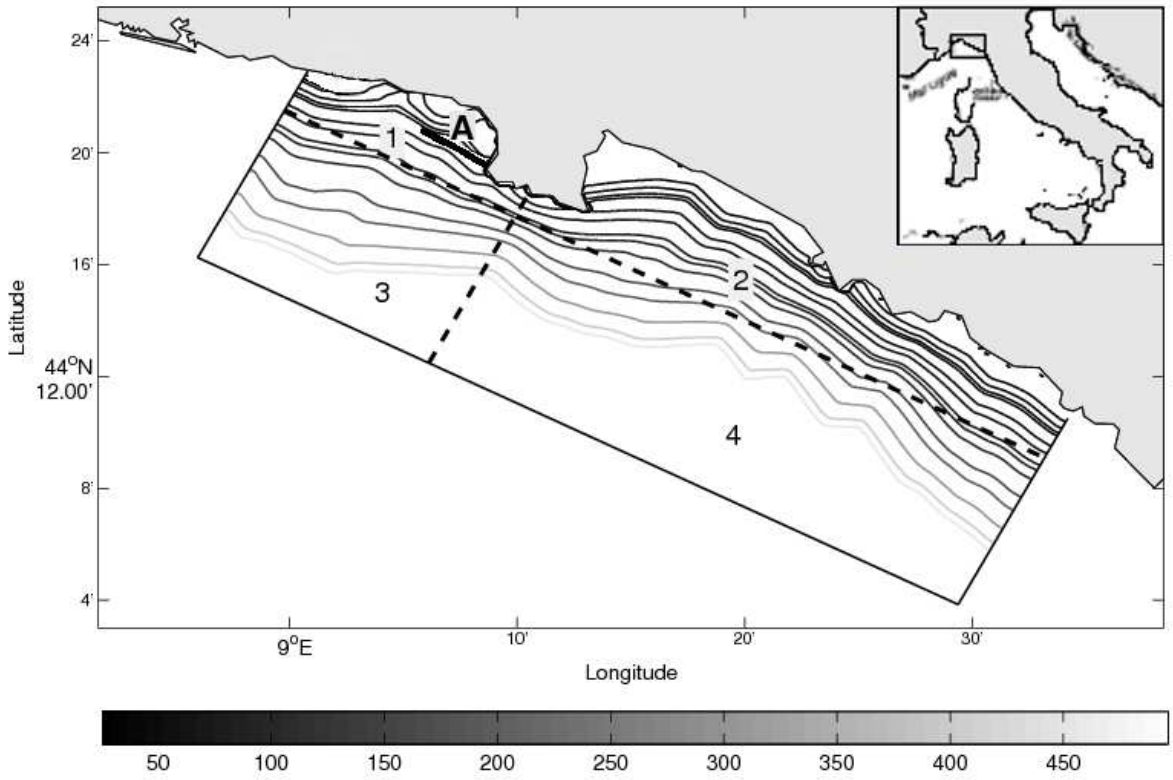

Figure 5.2: Coastal model domain. Contour lines show the bathymetry (m). Black line A represents the transport section. Numbers indicate the different zones of the model domain divided by the dashed black lines: (1) in-W, in-shore west (2) in-E, in-shore east (3) off-W, off-shore west and (4) off-E, off-shore east zone.

The POM numerical domain has three open boundaries and the following boundary conditions are considered : i) at the western (outcoming) boundary, radiation boundary conditions are used to radiate the barotropic velocity; ii) at the southern boundary, considering negligible the interaction with the open sea, a free slip wall is posed. Finally, iii) at the eastern (incoming) boundary the upstream inflow and the surface elevation are specified using the along shore component of the depth average velocity and the elevation data computed by regional model Symphonie (Hu et al., 2009), respectively.

The Symphonie model is an hydrostatic sigma-coordinate free-surface ocean model developed at the Pole Oceanographie Cotiere (CNRS & Université de Toulouse, Marsaleix et al., 2008). It computed the Western Mediterranean circulation from 2001 to 2003 with a horizontal spatial resolution of 3 km. Symphonie is itself forced by MFS model (Pinardi et al., 2003). A more detailed description of the Symphonie model is given in section A.2 of appendix A.

For all the three years simulated by Symphonie, the computed surface elevation and depth averaged velocity values in the grid meshes nearer to the eastern boundary of POM domain are extracted.

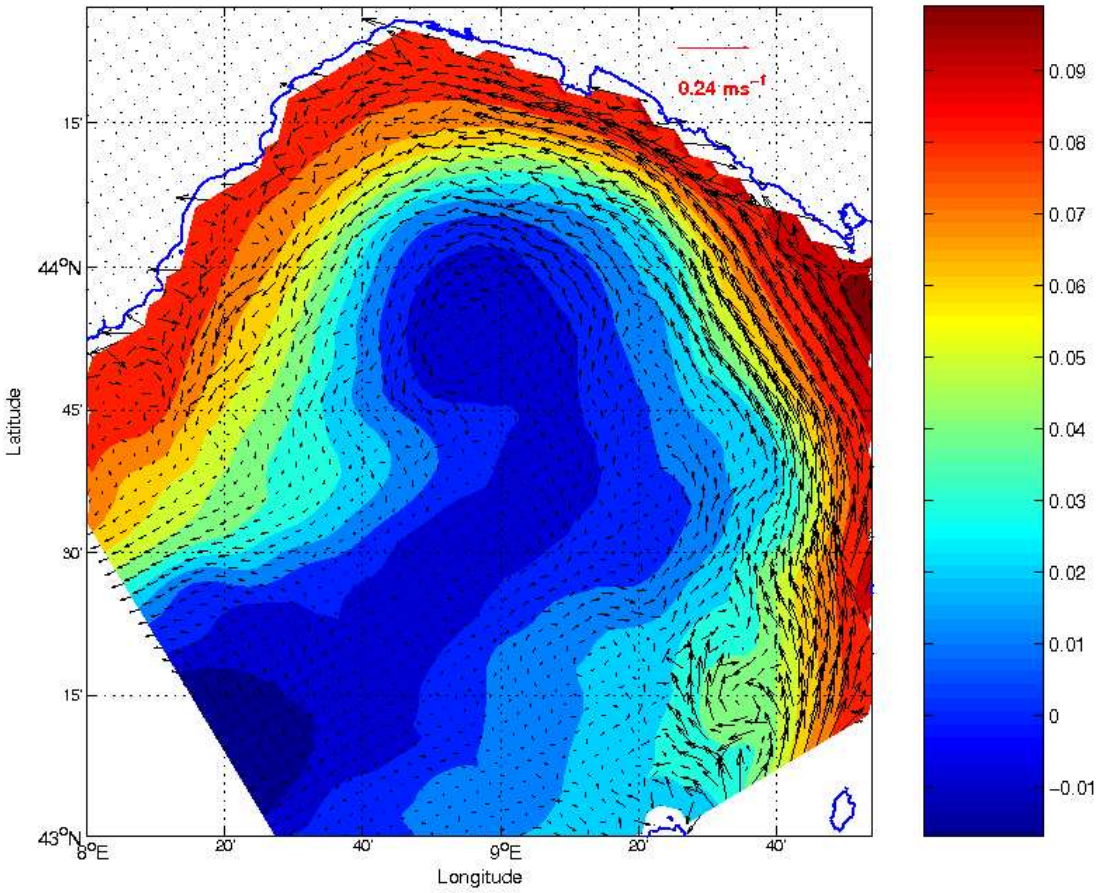

Figure 5.3: An example of the depth-averaged current field (ms^{-1}) and surface elevation (m) computed by Symphonie model in the Ligurian sea (February 2, 2001).

The Symphonie value nearest to the coast has been excluded because it has a low reliability (Fig. 5.3). Indeed, the smallest deep value for the Symphonie numerical simulations is setting to 3 m. This value is good for simulate the circulation in an area such as the Lion Gulf. While, for well resolved an area characterized by a narrow shelf and steep slope as the Ligurian Sea one, a precautionary value of minimum depth of 10 m would should be adopted. Since only few points nearest to the coast present this abnomalus value of current velocity, this does not invalidate the goodness of the Symphonie results.

Afterwards, the along-shore and cross-shore components of the current velocity computed by the Symphonie model are calculated, following the same method as in Astraldi and Manzella (1983) for the *in situ* measurements. Then, a cubic spline interpolation of the surface elevation and velocity component data is used to obtain the values for every grid mesh of POM open boundary. The choose of this interpolation is done in order to obtain a much realistic profile to force the simulations. The values of the elevation, along and cross-shore current utilized as boundary conditions (Table 5.1), range between -0.01 m to 0.12 m, between -0.37 ms^{-1} to 0.22 ms^{-1} and between -0.08 ms^{-1} to 0.06 ms^{-1}, respectively. The along-shore component is positive towards the south-east, the cross-shore towards the north-east.

Only the along-shore velocity component is used to force POM simulations at the eastern open boundary, in light of the low values of the cross-shore velocity component.

Symphonie outputs				
		2001	2002	2003
ssh (m)	min	-0.01	-0.02	-0.01
	max	0.12	0.11	0.09
	mean $\pm$ std	0.07 $\pm$ 0.00	0.04 $\pm$ 0.00	0.04 $\pm$ 0.00
along-shore (m s $^{-1}$)	min	-0.37	-0.30	-0.32
	max	0.21	0.11	0.22
	mean $\pm$ std	-0.06 $\pm$ 0.03	-0.06 $\pm$ 0.03	-0.04 $\pm$ 0.03
cross-shore (m s $^{-1}$)	min	-0.03	-0.01	-0.08
	max	0.08	0.06	0.05
	mean $\pm$ std	0.00 $\pm$ 0.01	0.00 $\pm$ 0.01	-0.00 $\pm$ 0.01

Table 5.1: Minimum, maximum and time and space average values of surface elevation and current velocity computed by Symphonie along the easter boundary of POM grid for the three simulated years.

The circulation in the study area is characterized by the presence of a northwestward current flowing approximately along the isobath and following the narrow shelf, with some periods of reversal (Astraldi and Manzella, 1983; Astraldi et al., 1990; Baldi et al., 1997). These characteristics are well reproduced by Symphonie model. In fact, the values of ssh, along and cross-shore velocity components in the cross-shore transect representing the POM eastern boundary, show a prevalence of the westward transport with some period of reversal especially in the summer period. For example, in a typical winter situation the along-shore component of velocity has a negative value and it is associate with a negliable cross-shore component (Fig. 5.4). While in a summer period the along-shore component is posivite and the associate cross-shore component remain negliable (Fig. 5.5).

In order to build a realistic initial condition, a spin-up simulation is run. In this simulation, the along-shore velocity component computed by Symphonie model for the first simulated day, January 1^{st} 2001, and the elevation computed with the geostrofic approximation are considered as initial condition. The simulation is carried out until it is reached the stationarity, i.e. when the total kinetic energy is constant (Fig. 5.6).

The last field of this simulation (Fig. 5.7) is used as initial condition for the run of 2001. As initial condition for the next years, the last ssh and current velocity fields of the previous simulated year are utilized.

In Doglioli et al. (2004a), the same POM setup is used and validated with the difference that the inflow is specified using the condition in Flather (1976) on the along-shore component of the depth-averaged current and the elevation is computed using the geostrophic approximation. Therefore, considering Symphonie outputs to force POM simulations, we can improve the reliability of the model and highlight the seasonal nature and the high temporal variability of the coastal current.

Surface condition

The wind fields at 10 m above the sea level provided by BOLAM model, are utilized as surface condition for the POM model. The wind data computed by BOLAM 21 and BOLAM 7 also over the POM domain, are horizontally interpolated to match the POM resolution. In Fig. 5.8 is reported an example of the obtained wind field considering the BOLAM 21 model, in Fig. 5.9 one considering the BOLAM 7 model.

The wind stress $\boldsymbol{\tau}_w$ is computed using the classical bulk formula:

$$\boldsymbol{\tau}_w = \frac{\rho_{ar}}{\rho_{wr}} C_D \, \mathbf{w}_{10}^2 \tag{5.1}$$

where $\mathbf{w}_{10}$ is the interpolated wind speed at 10 m above the sea level, ρ_{ar} and ρ_{wr} are the air and water density, respectively.

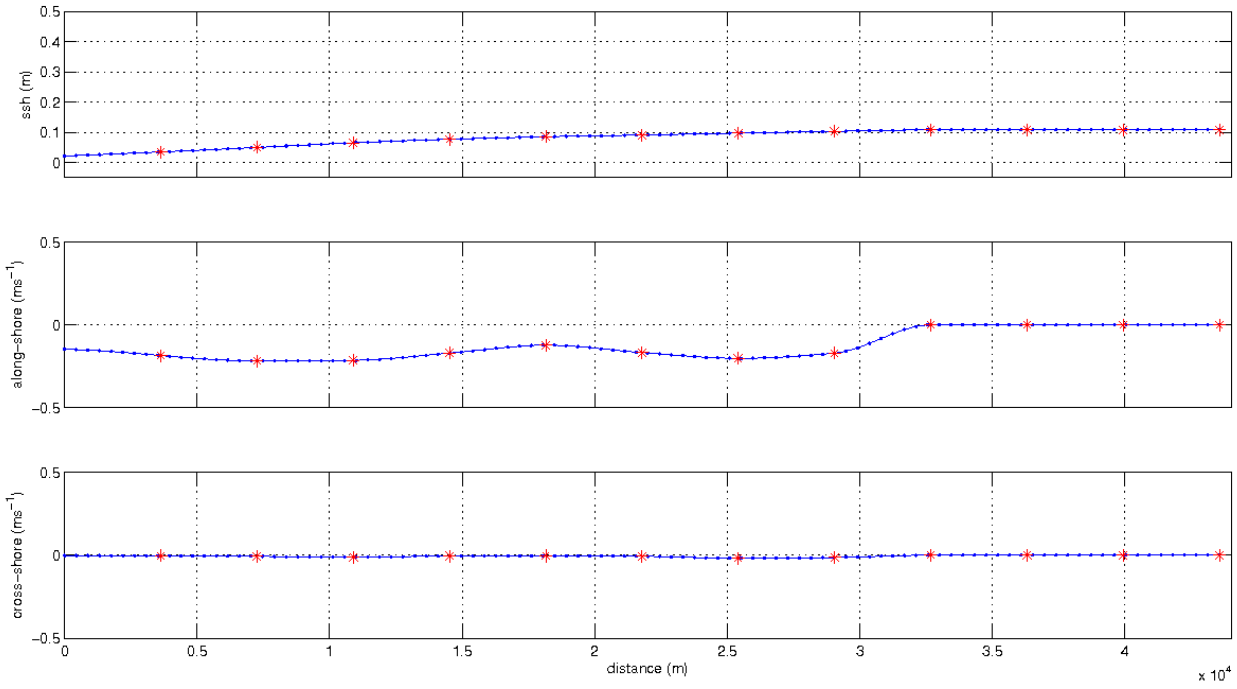

Figure 5.4: Free surface elevation (m), along and cross-shore components (ms^{-1}) of current velocity computed by Symphonie (red asterisks) for February 3, 2001 and interpolated on the POM easter boundary (blue points and line).

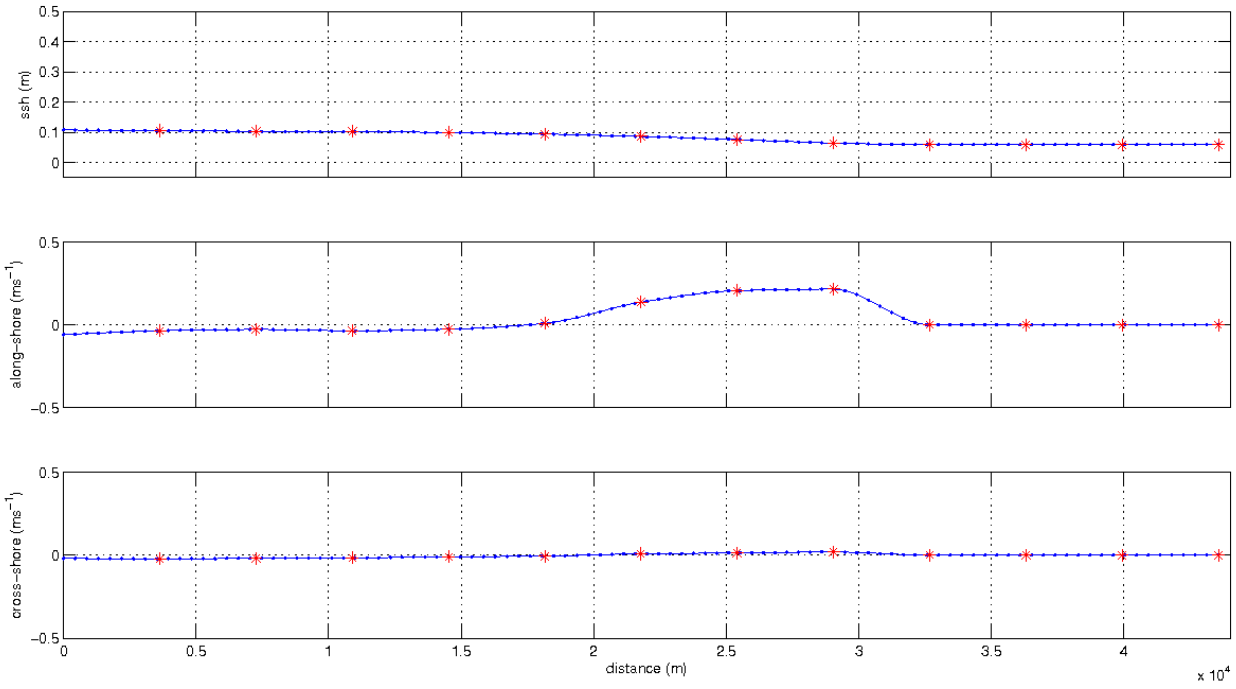

Figure 5.5: Free surface elevation (m), along and cross-shore components (ms^{-1}) of current velocity computed by Symphonie (red asterisks) for August 16, 2001 and interpolated on the POM easter boundary (blue points and line), in a period of current reversal.

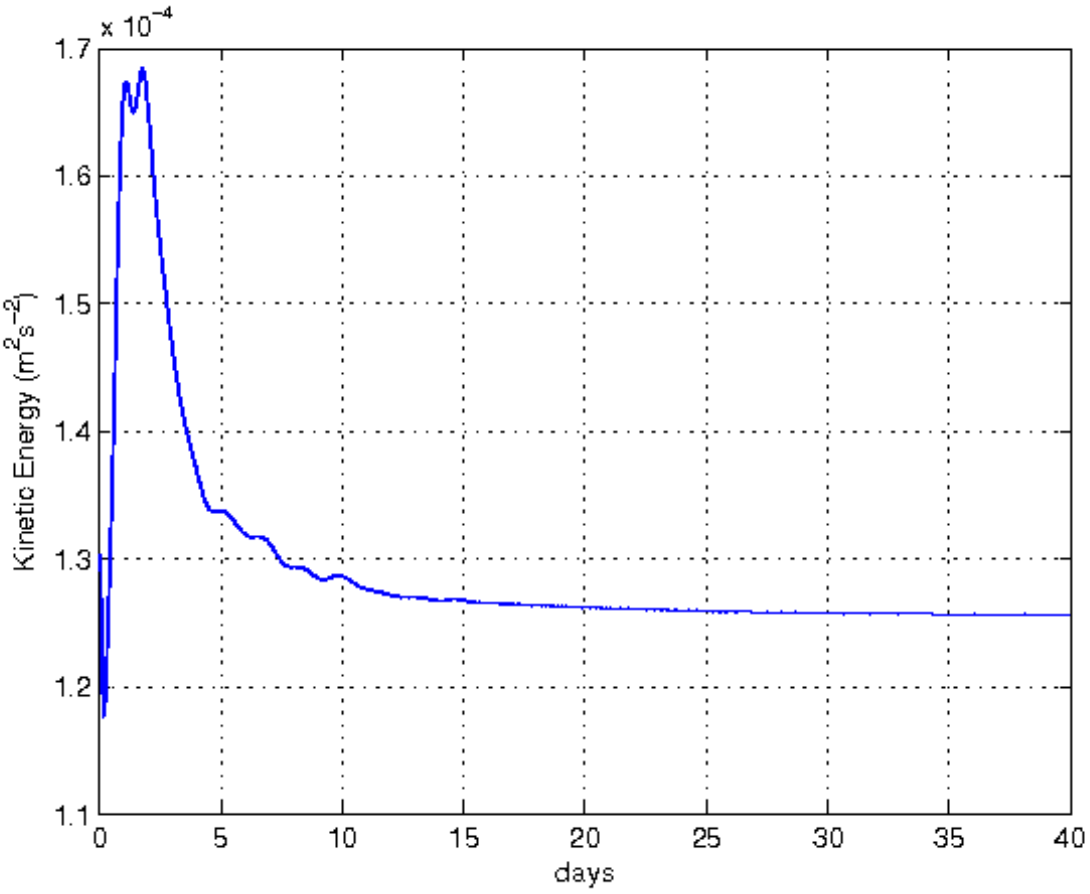

Figure 5.6: Kinetic energy (m^2s^{-2}) of the spin-up simulation.

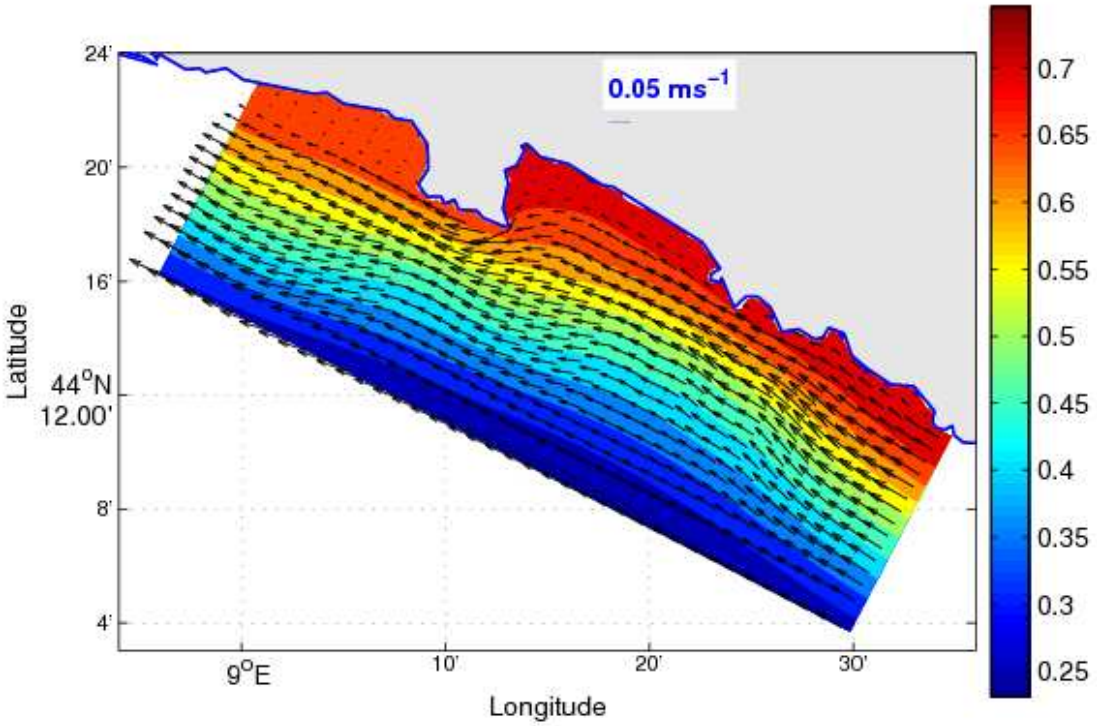

Figure 5.7: Depth averaged velocity field (m s^{-1}) and elevation anomaly (m) simulated by the spin-up simulation for February 9, 2001.

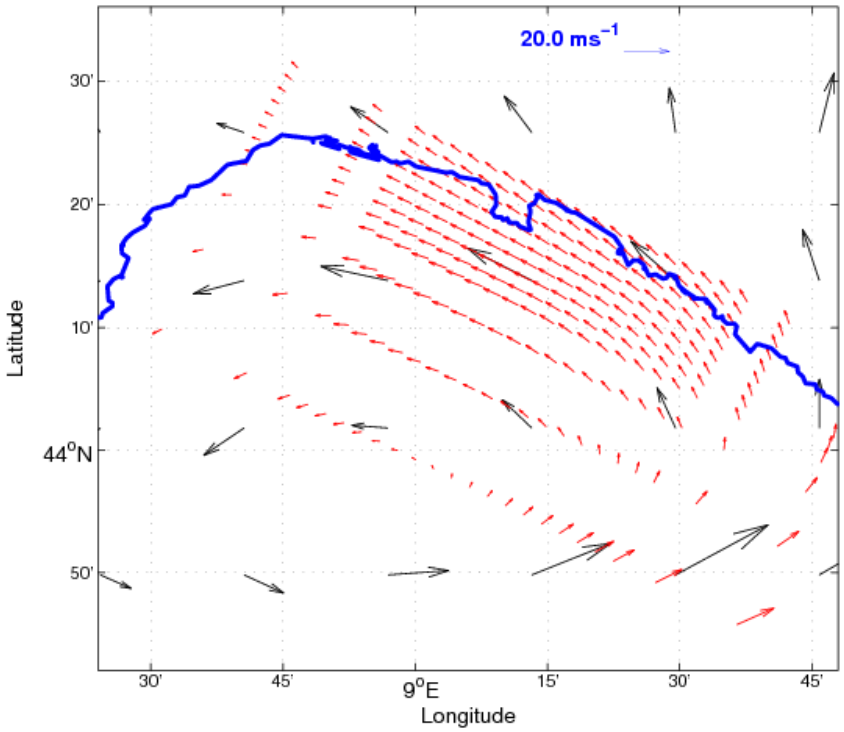

Figure 5.8: Wind velocity computed by BOLAM 21 model (black arrows) for March 6, 2001 and interpolated in the POM domain and in the buffer zone (red arrows).

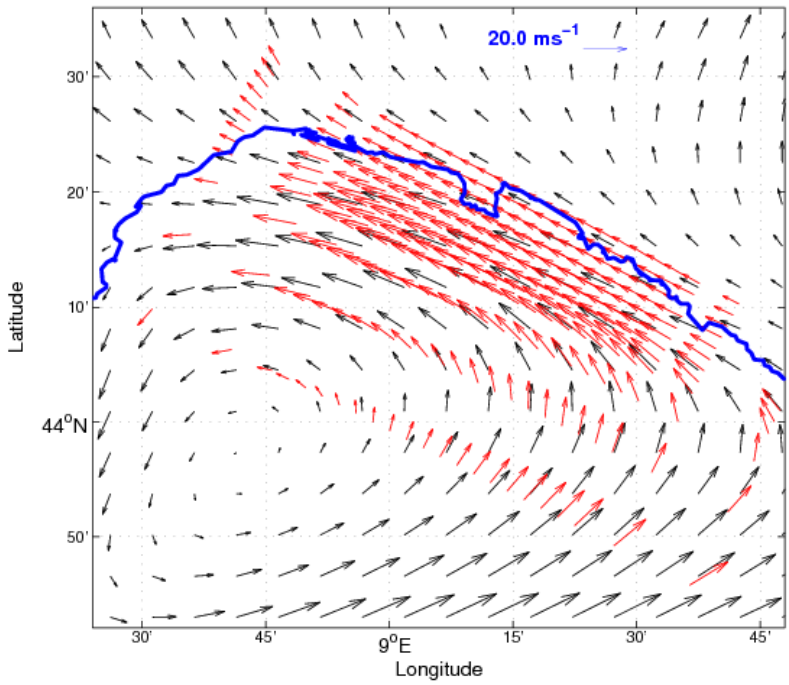

Figure 5.9: Wind velocity computed by BOLAM 7 model (black arrows) for March 6, 2001 and interpolated in the POM domain and in the buffer zone (red arrows).

Two different simulation sets are performed varying the drag coefficient C_D value. In the first set, the drag coefficient is fixed to the value $C_D = 10^{-3}$. In the second set, the drag coefficient value varies with the wind speed variations as proposed by Csanady (1982):

$$C_D = 1.6\ 10^{-3} \qquad w_{10} \leqslant 7\ ms^{-1} \tag{5.2}$$

$$C_D = 2.5\ 10^{-3} \qquad w_{10} > 10\ ms^{-1} \tag{5.3}$$

To fill the wind values between 7 and 10 ms^{-1}, the C_D value is calculated linearly:

$$C_D = 1.9\ 10^{-3} \qquad 7\ ms^{-1} < w_{10} \leqslant 8.5\ ms^{-1} \tag{5.4}$$

$$C_D = 2.2\ 10^{-3} \qquad 8.5\ ms^{-1} < w_{10} \leqslant 10\ ms^{-1} \tag{5.5}$$

In summary, five runs of the POM model are taken place from January 2001 to December 2003:

- a reference simulation without wind forcing,
- two runs forced by BOLAM 21 wind, with the constant and the variable value of the drag coefficient,
- two runs forced by BOLAM 7 wind, again with the same constant and variable value of the drag coefficient.

5.1.3 Cluster analysis

Cluster analysis is a numerical technique which tries to allocate objects into groups, or clusters, following some kind of similarity criterion based on the definition of a distance metric measure between two objects

and an aggregation algorithm, such that a couple of objects in the same cluster can be considered more similar than a couple of objects belonging to distinct clusters (Everitt, 1977).

Cluster analysis is widely adopted in climatology for grouping stations or grid points to define climate regions and for the classification of wind regimes (e.g. Weber and Kaufmann, 1995). More recently, a two-stage clustering technique has been developed for the classification of mesoscale wind fields in both station and model data (Burlando et al., 2008; Burlando, 2008, respectively).

As regard oceanography, several studies apply cluster analysis to hydrological data. For example, Becker and Pauly (1996) propose a regional classification of the SST anomaly fluctuations patterns in the North Sea. Warn-Varnasa et al. (2005), defining a water mass as a cluster of points consisting of temperature, salinity and depth values, study the water mass characteristics and distributions of the Wilkinson Basin area in the northwest corner of the Gulf of Maine.
To our knowledge, there are not yet applications of the cluster analysis on current velocity data. Nevertheless, there is no theoretical constraint to apply the same cluster methodology already used for the wind data to the current ones, in order to identify and classify the typical current regimes of the studied area. This approach allows to identify both the typical wind regimes and the current ones, then, linking the results, helps to understanding the influence of the wind regimes on the circulation patterns.

Therefore, the cluster analysis is performed on the two data sets of wind (i.e. BOLAM 21 and BOLAM 7 runs) and on the five data sets of coastal current (i.e. no-wind forcing, BOLAM 21 wind forcing with the constant and the variable drag coefficient value, BOLAM 7 wind forcing with the same constant and variable drag coefficient value). For each BOLAM simulation, we have 8696 wind patterns (i.e. one output every three hours for three years), while for each run of the POM model, the number of current patterns is 1087 (i.e. one output every day for three years).

Each data set is partitioned into k clusters, following the clustering procedure applied by Burlando et al. (2008). This methodology is based on a two-stage clustering procedure as suggested by Kaufmann and Weber (1996) (see also Weber and Kaufmann, 1995; Kastendeuch and Kaufmann, 1997; Kaufmann and Whiteman, 1999):

- in the first stage a hierarchical cluster analysis is adopted to obtain a first-guess classification into k groups;

- in the second stage the centroids of the first-guess clusters become initial seeds for the k-means partitional clustering which is used to rearrange the patterns into an optimal final classification.

In particular, the hierarchical aggregation method is based on Ward's minimum variance technique applied to a Euclidean distance, while the partitional method consisted of the k-means method with minimization of the total variance, in order to assume the same metric to define clusters during the first and second stage.
The main advantage of using a hierarchical followed by a non-hierarchical clustering is that, in purely hierarchical clustering, if an erroneous classification groups two clusters in an early stage of the process, there can be no reclassification at any later stage. Partitional methods, which do not involve the tree-like construction process, allow elements to be reassigned inside clusters until some metric relative to the centroids of the clusters is minimized.
Therefore, this procedure produces firstly a tree-like structure (dendrogram) corresponding to the successive hierarchical merging of the patterns into a single final cluster. The choice of the final number of clusters representative of the main regimes is made on the basis of the values of the total variance, i.e. the sum of the cluster variances, when clusters merge along the tree-like structure of the dendogram. Indeed, as suggested by Kaufmann and Weber (1996), the value of the metric associated to the clustering algorithm, which is an indicator of information loss when two clusters gather together, can be assumed as an objective meter for this purpose.
To have a deeper understanding of the obtained clusters, the components of the horizontal vectors are recovered and the corresponding average vectors, i.e. the vectors of the average components, are calculated for every cluster.

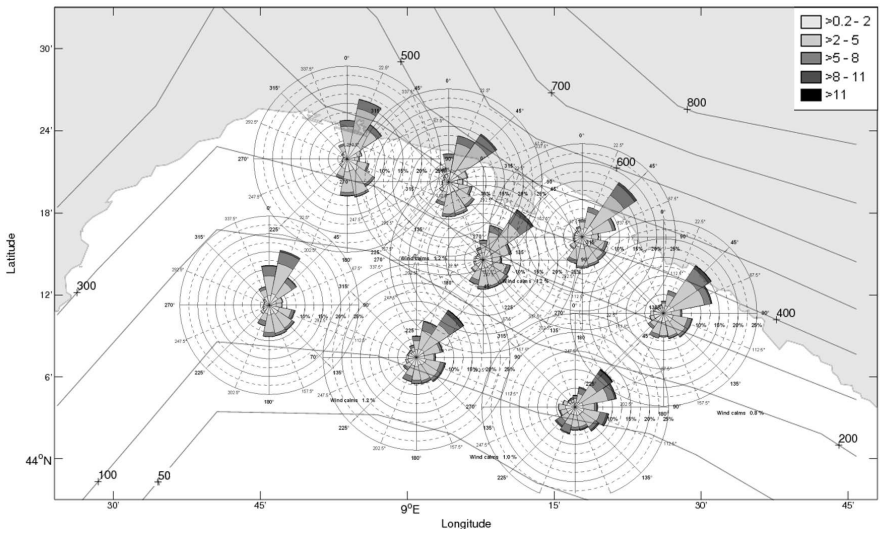

Figure 5.10: Wind roses of the complete time series of the BOLAM 21 wind at 10 m above the sea level in the eight considered stations. All the wind roses are drawn considering the same frequency scale i.e. between 0 % and 25 %. Contour lines represent the orography used by the model (m).

5.2 Results

The results are shown in five in-shore and three off-shore stations in the studied area (Fig. 5.13).

5.2.1 Atmospheric model results

The distributions of the amplitude and direction of the wind at 10 m above the sea level provided by BOLAM 21 and BOLAM 7 for the three years at the eight stations, are computed and showed in Fig. 5.10 and Fig. 5.11, respectively. In the figures, the orography used by the model is also reported. Obviously, BOLAM 7 better resolves the orography than BOLAM 21. For example, the mountain pass of the Ligurian Appennines northeast of the Promontorio of Portofino is completely smoothed out in BOLAM 21. Nonetheless the coast line of both BOLAM 21 and BOLAM 7 is about one hundred kilometers south of the real one. This diminishes the wind amplitude computed by the atmospheric model in the corresponding POM domain area, because the surface roughness of the sea is less than the land one.

All BOLAM 21 wind roses present two preferential wind sectors centered around the northeast and south-southeast. Instead, BOLAM 7 wind roses present greater geographical variability. Offshore, the south-southeast component increases. Inshore, the frequent north-easterly wind rotates clockwise from station 1 to station 5, following the topographical forcing. Moreover, the wind blowing from the south-west shows greater frequency and intensity than in the BOLAM 21 simulations.
The results of the statistical analysis depicted in Fig. 5.10 and Fig. 5.11 fit the wind climatology of the northern Tyrrhenian Sea as reported by Burlando et al. (2008), who studied the main wind regimes of this area. Indeed, the winds blowing from northeast and southeast, which are respectively known as grecale and sirocco, are commonly due to the presence of a synoptic bi-polar structure consisting of a high-pressure in northwestern Europe and a low-pressure over the western or central Mediterranean. The wind blowing from the south-west can be due, in the area under study, to different synoptic forcing. On the one hand, it can be due to a mistral event, corresponding to north-westerly winds over the western Europe induced by a high-pressure over mid-latitude North-Atlantic coupled with a low pressure over central Europe. The mistral wind usually turns anticlockwise around the Alps and blows from west or southwest in the eastern Liguria. On the other hand, the Libeccio wind, which also comes from the south-west, is caused by a completely different synoptic pattern when a dipole of high-pressure over Greenland and low-pressure over mid-latitude North

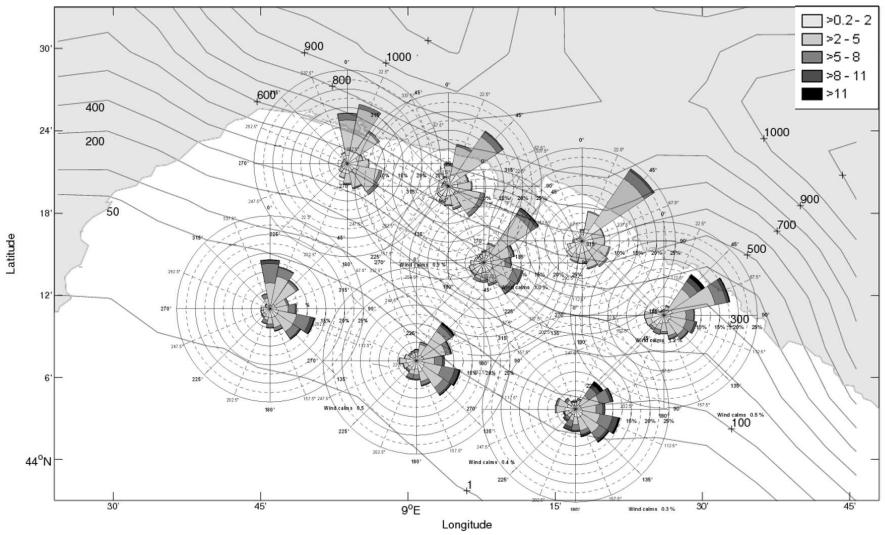

Figure 5.11: Wind roses of the complete time series of the BOLAM 7 wind at 10 m above the sea level in the eight considered stations. All the wind roses are drawn considering the same frequency scale i.e. between 0 % and 25 %. Contour lines represent the orography used by the model (m).

Atlantic causes south-westerly winds over the western Mediterranean.

Progressive vectors are used to demonstrate the difference between the two wind forcings (Fig. 5.12). Indeed, BOLAM 7 progressive vectors generally cover $13 \cdot 10^4$ km in 1087 days for $9 \cdot 10^4$ km in the BOLAM 21 cases. At stations 3, 6 and 7, the BOLAM 7 have a stronger northward component than their BOLAM 21 counterparts.

5.2.2 Coastal circulation model results

In regard to the POM results, progressive vectors of velocity of the simulated current without wind forcing in the aforementioned stations for the three simulated years, are showed in Fig. 5.13. Full dots represent the initial position of the current vectors and the progressive vector displacements are shown to scale. All off-shore stations show the north-westward transport observed in the past literature (Astraldi and Manzella, 1983), while stations 1, 2 and 4 reveal current separation and eddy formation around the cape (Doglioli et al., 2004a).

For the following three scenarios, no-wind, BOLAM 21 and BOLAM 7 wind forcing with the constant value of C_D, the progressive vectors of the simulated current in the in-shore and off-shore stations are showed in Fig. 5.14. Black circles represent the initial positions of the progressive vectors. A cross, full dot and star are drawn every ninety days, starting from January 1^{st}, 2001 for no-wind, BOLAM 21 and BOLAM 7 wind forcing, respectively. The greater differences between the different forcing are seen in the in-shore stations, where the effect of the wind favors the countercurrent and the eddy formation. Considering the high resolution of wind forcing, it is possible to note greater rotation of the current in the in-shore stations especially in the 1, 3 and 4 ones. In the off-shore stations the higher resolution of the wind forcing does not seem to have an important effect.

In Fig. 5.15 the simulated current velocity progressive vectors considering the no-wind forcing, already showed in Fig. 5.14, and the BOLAM 21 and BOLAM 7 wind forcing with the variable drag coefficient value, are reported. At the in-shore stations, the difference between no-wind and wind forcing is greater than in the previous case (i.e. the constant C_D value). Moreover, in this case, while the difference between the wind

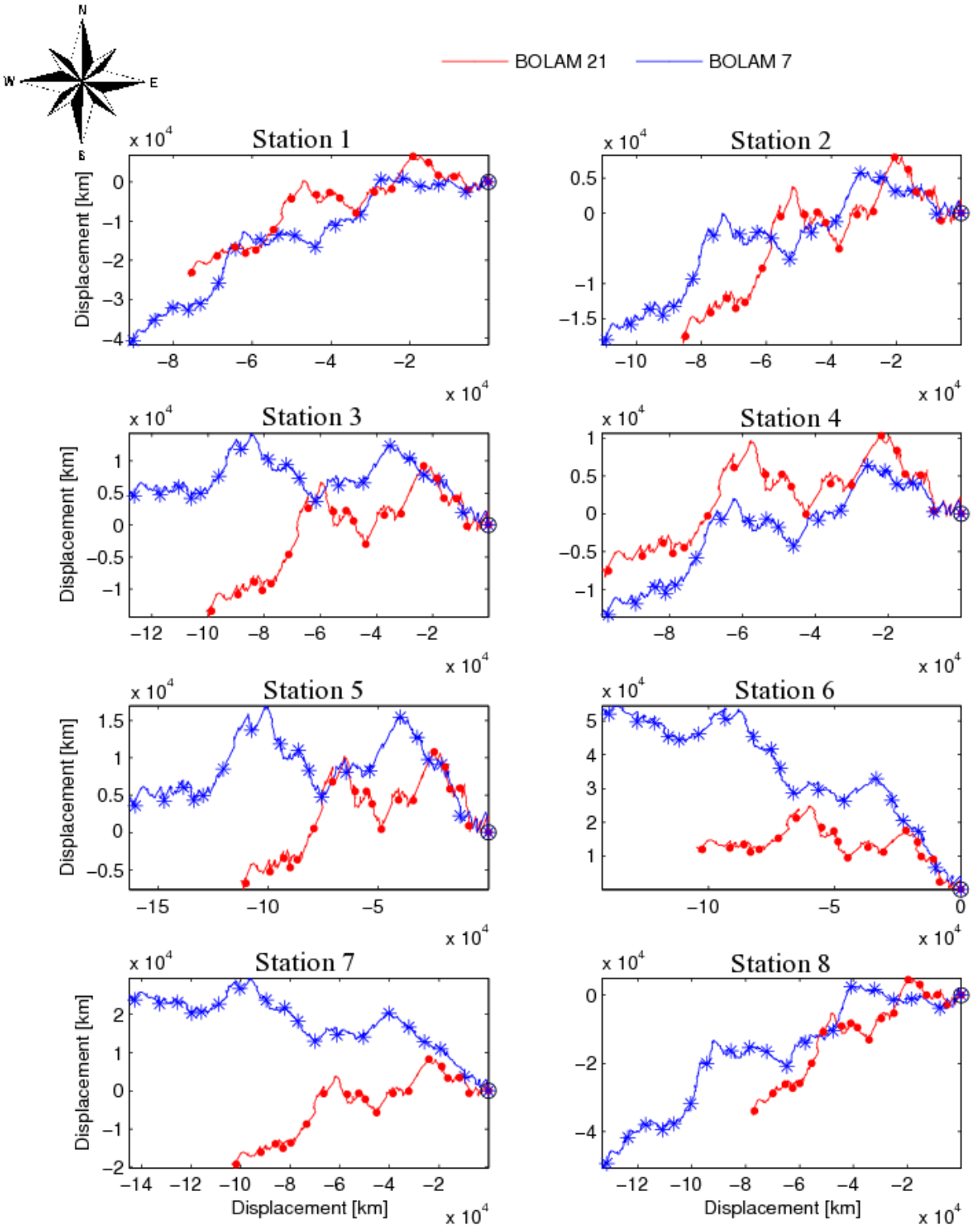

Figure 5.12: Progressive vectors of the wind simulated by BOLAM 21 (red line) and BOLAM 7 (blue line) model in the in-shore and off-shore stations. The circles represent the starting positions. A full dot (BOLAM 21) and star (BOLAM 7) are drawn every 90 days starting from January 1^{st}, 2001.

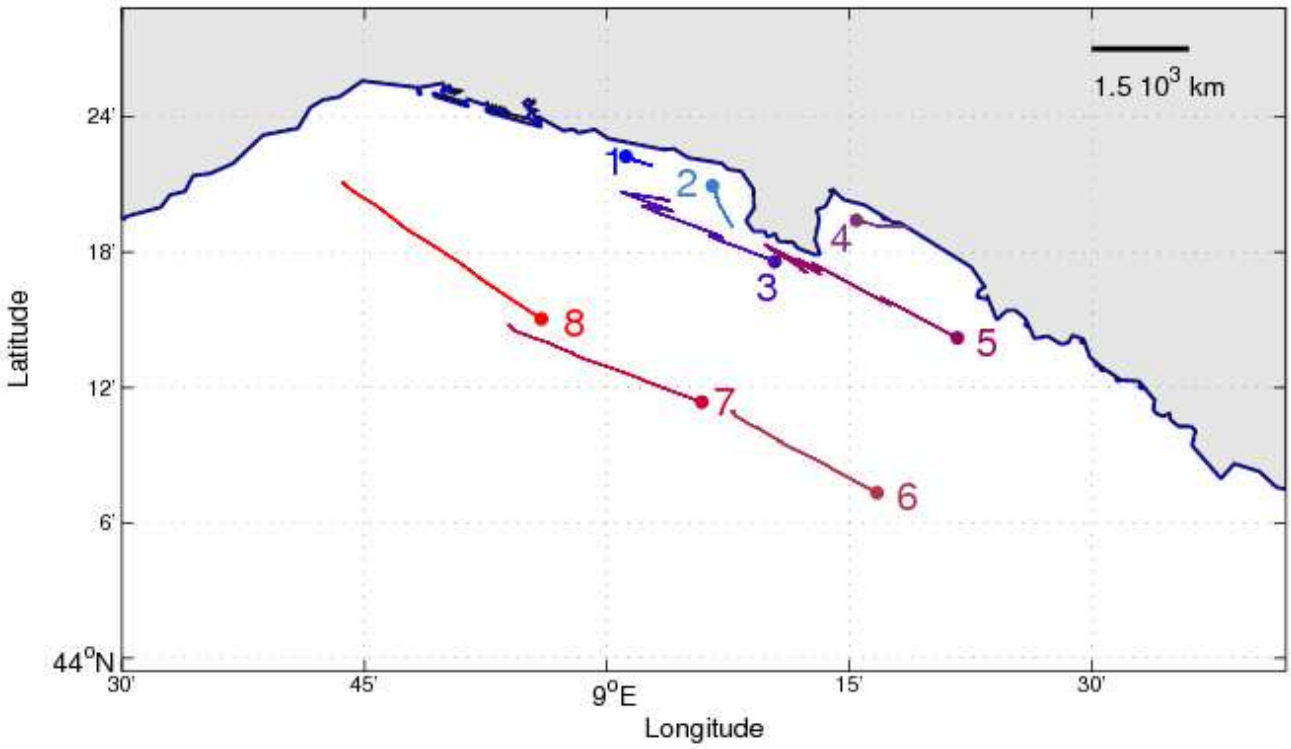

Figure 5.13: Positions of the eight stations, where the in scale progressive vectors of current velocity computed by the model for the three simulated years without wind forcing are computed. Full dots represent the initial positions. The scale of the current progressive vectors is reported at the top right corner.

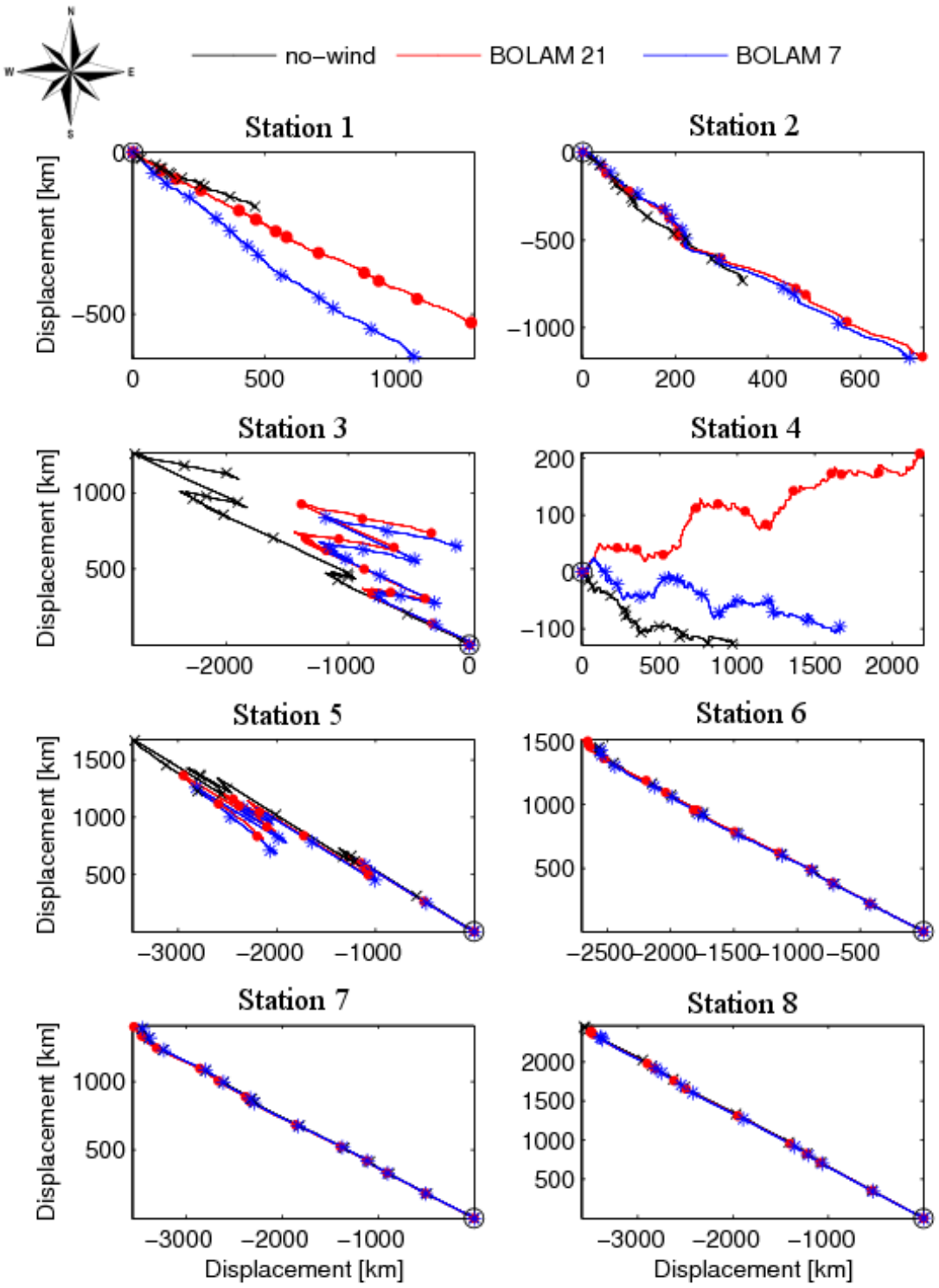

Figure 5.14: Simulated current progressive vectors in the in-shore and off-shore stations. Black line represents the current progressive vector considering no-wind forcing, red line considering the BOLAM 21 forcing with the constant drag coefficient value and blue line considering the BOLAM 7 one with the same constant drag coefficient value. The circles represent the starting positions. A cross (no-wind), full dot (BOLAM 21 forcing) and star (BOLAM 7 forcing) are drawn every 90 days starting from January 1^{st}, 2001.

forcing is small, the difference between the forced coastal circulation, especially at stations 3 and 5, is much bigger.

In Fig. 5.16, the amplitude and the direction of the simulated current considering no-wind forcing (A), BOLAM 7 with the constant C_D value (B) and with the variable C_D value (C), are shown.
Once again, off-shore the differences in the simulated current between the three represented scenarios are small and are mainly observable in the case in which the variable drag coefficient value is considered.
In-shore, the greater differences can be observed in station 1, 2 and 4 where the coastal countercurrent and the eddy behind the cape are formed. The latters are more intense in the scenario with the variable value of drag coefficient.

In order to assess the variation in kinetic energy associated with the currents considering the different forcing, the numerical domain is divided in four parts, with an idealized division between the in-shore and off-shore area and east and west zone of the promontory (dashed black line in Fig. 5.2). The average specific kinetic energies for different zones and scenarios are computed and reported in Table 5.2.

		Average specific kinetic energy $(10^{-8}\ s^{-2})$			
forcing		***zones***			
		in-W	*in-E*	*off-W*	*off-E*
no-wind		0.94 ± 1.01	3.42 ± 4.19	1.68 ± 2.65	1.91 ± 2.93
BOLAM 21	C_D *constant*	1.06 ± 0.84	3.80 ± 4.23	1.71 ± 2.58	2.02 ± 2.94
	C_D *variable*	1.72 ± 2.05	5.61 ± 6.18	2.42 ± 2.39	2.63 ± 2.90
BOLAM 7	C_D *constant*	1.07 ± 0.78	3.67 ± 4.30	1.62 ± 2.48	1.96 ± 2.89
	C_D *variable*	1.78 ± 2.32	6.30 ± 8.44	1.95 ± 2.39	2.75 ± 2.89

Table 5.2: Average specific kinetic energy in the four zones of the domain (Fig. 5.2) for every simulated scenario.

For all zones, the average specific kinetic energy is greater considering wind forcing than no-wind scenario. In fact considering the wind forcing, the specific kinetic energy increases especially in the in-shore zones. In particular, the kinetic energy of the in-west zone mostly increases than the other ones. Moreover, the greater increase of the kinetic energy for the in-shore west zone is observed considering the higher resolution wind forcing, both with the constant and variable drag coefficient value. However, an increase of the kinetic energy in all considered zones is observed considering the variable value of drag coefficient.

Moreover, in order to assess the intensity of the eddy downstream to the cape, the mass transport trough the section A (Fig. 5.2) is computed. The average mass transport through the section A is negative in all simulated scenarios indicating an off-shore transport, in according to the presence of the eddy downstream the cape (Table 5.3). Considering the experiments with the wind forcing, this off-shore transport increases. Moreover in the experiment with BOLAM 7 forcing both with the constant and variable drag coefficient value, the mass transport is greater than in the same case with BOLAM 21 forcing. The greatest value of the off-shore transport is due to the experiment considering BOLAM 7 forcing with the variable C_D value.

In order to highlight the difference in the simulated coastal current considering the different forcings, along-shore and cross-shore components of the simulated current at station 5, for five considered scenarios,

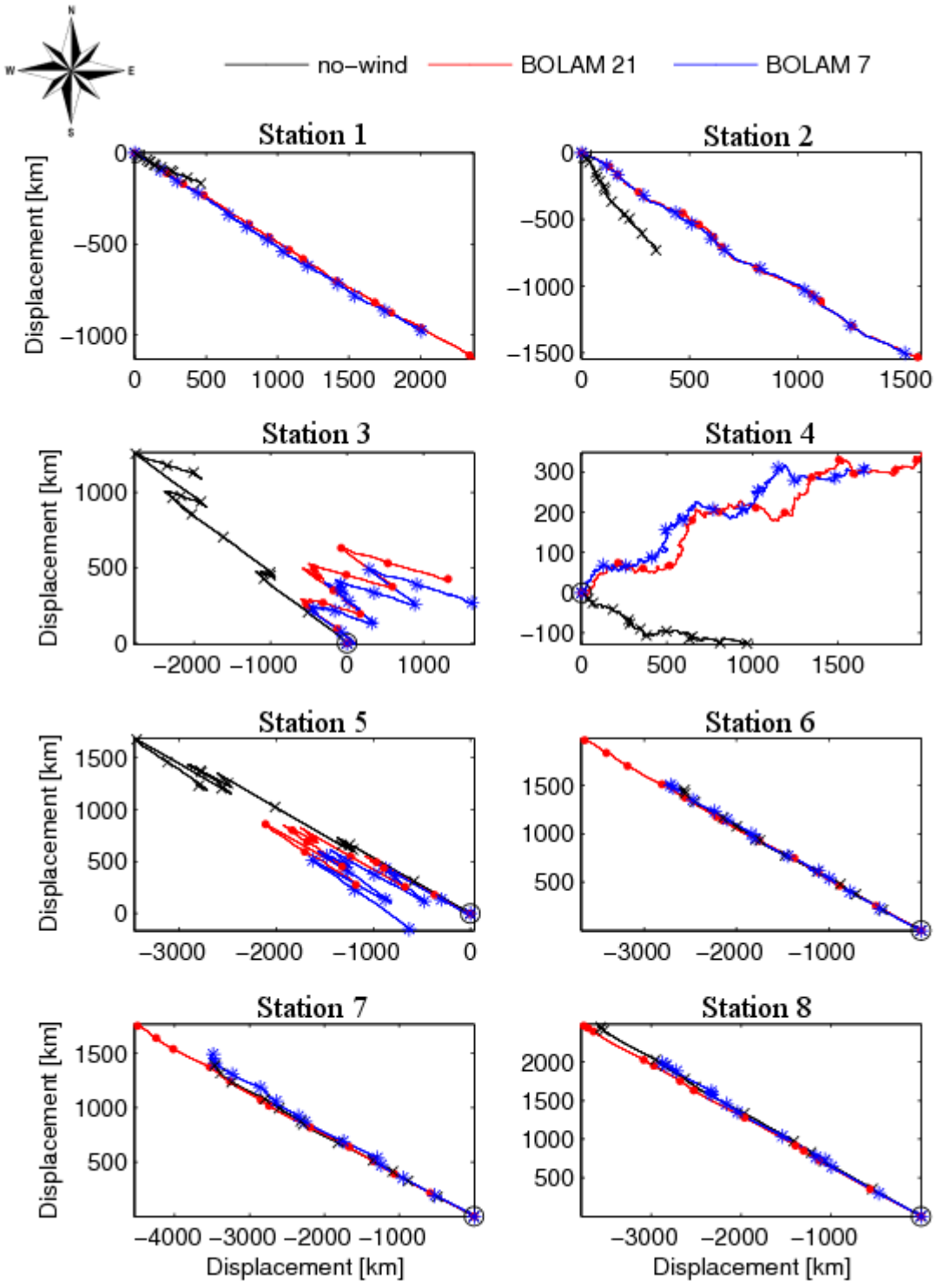

Figure 5.15: Simulated current progressive vectors in the in-shore and off-shore stations. Black line represents the same current progressive vector considering no-wind forcing already showed in Fig. 5.14, red line considering the BOLAM 21 forcing with the variable drag coefficient value and blue line considering the BOLAM 7 one with the same variable drag coefficient value. The circles represent the starting positions. A cross, full dot and star are drawn every 90 days starting from January 1^{st}, 2001 for no-wind, BOLAM 21 and BOLAM 7 wind forcing, respectively.

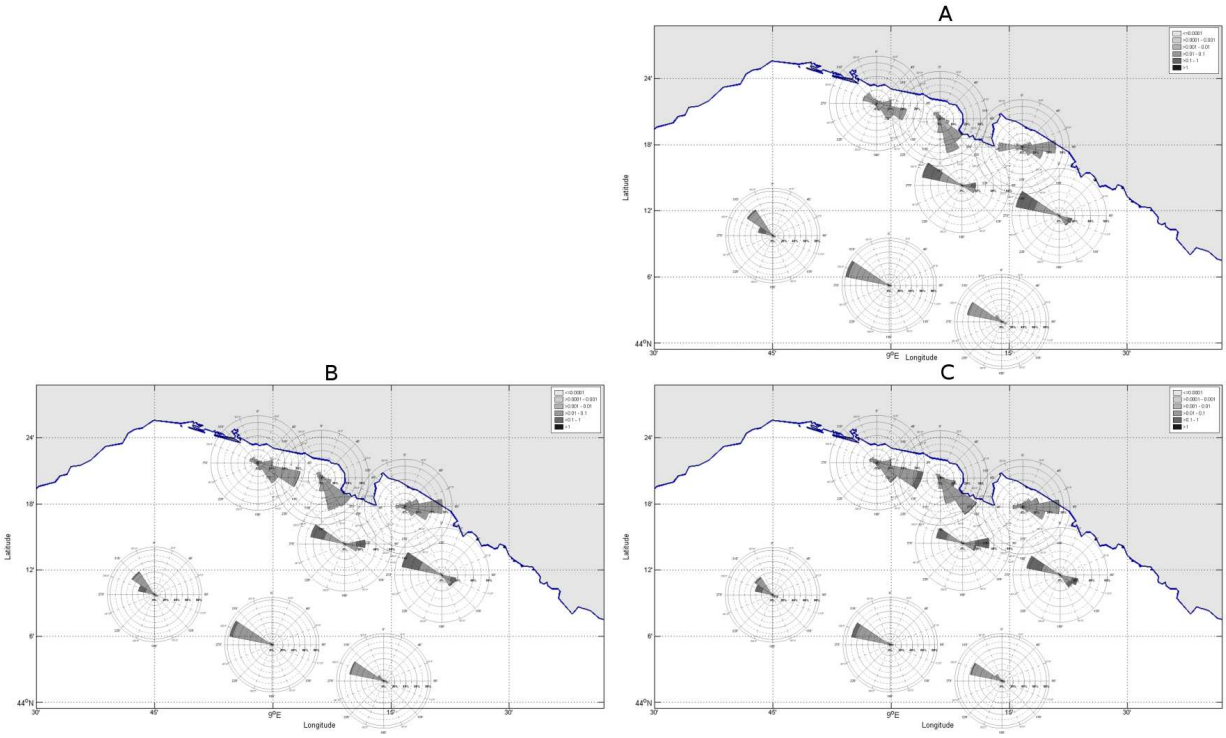

Figure 5.16: Current roses of the complete time series considering: A) no-wind forcing, B) BOLAM 7 wind forcing with the constant C_D value and C) BOLAM 7 wind forcing with the variable C_D value, in the eight considered stations. For stations 1, 2 and 4 the frequency scale range between 0 % and 35 %, for stations 3 and 5 between 0 % and 60 % and finally, for stations 6, 7 and 8 between 0 % and 82 %.

		Mass transport (10^{-2} Sv)		
forcing		***simulated years***		
		2001	*2002*	*2003*
no wind		-0.39 $\pm$ 1.10	-0.32 $\pm$ 0.77	-0.27 $\pm$ 1.88
BOLAM 21	C_D *constant*	-0.72 $\pm$ 1.89	-0.53 $\pm$ 1.50	-0.91 $\pm$ 2.11
	C_D *variable*	-1.50 $\pm$ 3.25	-1.06 $\pm$ 2.95	-2.12 $\pm$ 3.89
BOLAM 7	C_D *constant*	-0.77 $\pm$ 1.92	-0.56 $\pm$ 1.63	-0.96 $\pm$ 2.14
	C_D *variable*	-1.80 $\pm$ 3.82	-1.39 $\pm$ 3.09	-2.27 $\pm$ 4.29

Table 5.3: Annual average and standard deviation of mass transport trough the section A showed in Fig. 5.2 for every simulated scenario.

are computed following the methodology used by Astraldi and Manzella (1983) for *in-situ* data. Moreover, we distinguish between the two directions of every velocity component. In Table 5.4, the maximum and average values of the simulated current for every direction, are reported. While the annual average coastal current (i.e. northwestward along-shore component) does not varies much considering the different scenarios, the annual average coastal countercurrent (i.e. southeastward along-shore component) is more intense when higher-resolution wind forcing and variable drag coefficient value are considered. Both for the northeastward and southwestward cross-shore components, the annual average does not varies with the different simulated scenarios.

Model Output			***along-shore*** (cm s^{-1})		***cross-shore*** (cm s^{-1})	
			NW (-)	SE (+)	NE (+)	SW (-)
no wind		max	21.7	14.1	2.9	6.5
		ave $\pm$ std	8.7 $\pm$ 5.4	5.7 $\pm$ 3.6	0.3 $\pm$ 0.3	0.8 $\pm$ 0.8
BOLAM 21	C_D *constant*	max	21.4	15.2	3.2	6.5
		ave $\pm$ std	8.7 $\pm$ 5.4	6.1 $\pm$ 3.6	0.3 $\pm$ 0.3	0.8 $\pm$ 0.8
	C_D *variable*	max	25.6	18.7	3.2	6.5
		ave $\pm$ std	8.9 $\pm$ 5.3	7.1 $\pm$ 4.8	0.3 $\pm$ 0.3	0.8 $\pm$ 0.8
BOLAM 7	C_D *constant*	max	21.5	18.4	6.7	6.4
		ave $\pm$ std	8.7 $\pm$ 5.3	6.3 $\pm$ 3.8	0.3 $\pm$ 0.4	0.9 $\pm$ 0.9
	C_D *variable*	max	23.0	18.9	6.7	6.4
		ave $\pm$ std	8.6 $\pm$ 5.3	8.0 $\pm$ 5.2	0.3 $\pm$ 0.4	0.9 $\pm$ 0.9

Table 5.4: Comparison between the model outputs of current velocity in station 5, considering the different scenarios.

5.2.3 Cluster analysis results

The cluster analysis, firstly on the two wind data sets (i.e. BOLAM 21 and BOLAM 7 runs) and then on the five coastal current data sets (i.e. no-wind forcing, BOLAM 21 forcing with the constant and variable C_D value, BOLAM 7 forcing with the same constant and variable C_D value), is performed.

In regard to the wind data, only the results obtained with the BOLAM 7 data set are reported. The reason of this choice is that the wind simulated by BOLAM 7 model better reproduces the wind dynamic of the area resulting in general less smooth and less uniform into the domain than the BOLAM 21 one, as showed by previous results.

The dendogram obtained by the cluster procedure is showed in Fig. 5.17 and corresponds to the successive hierarchical merging of the wind patterns into a single final cluster.

The total variance of the subsequent cluster merging as a function of the number of remaining clusters is showed in Fig. 5.18. The diagram shows a strong reduction of the total variance at the steps corresponding to $k = 2$, $k = 3$, $k = 6$ and $k = 10$ clusters, while it decreases slowly after the latter value. Also the wind data set considering BOLAM 21 model show a reduction of the total variance at the steps corresponding to $k = 3$ and $k = 6$ clusters. We choose $k = 3$ because it represents the higher aggregation level characterized by very different clusters.

In Fig. 5.19, the monthly cycles of the resulting clusters for the BOLAM 7 wind are showed. Cluster $w1$ shows a seasonal cyclicity in winter, while clusters $w2$ and $w3$ are mainly summer regimes. Cluster $w1$ is very frequent every month and has a maximum in December and January. As far as summer regimes are concerned, cluster $w2$ has a maximum in July and August, while the distribution of cluster $w3$ is more spread than the other summer regime.

The cluster analysis performs on the five data sets of coastal current also generates three different clusters with a similar monthly distributions than the ones in Fig. 5.19. Moreover, for the current, the clusters are

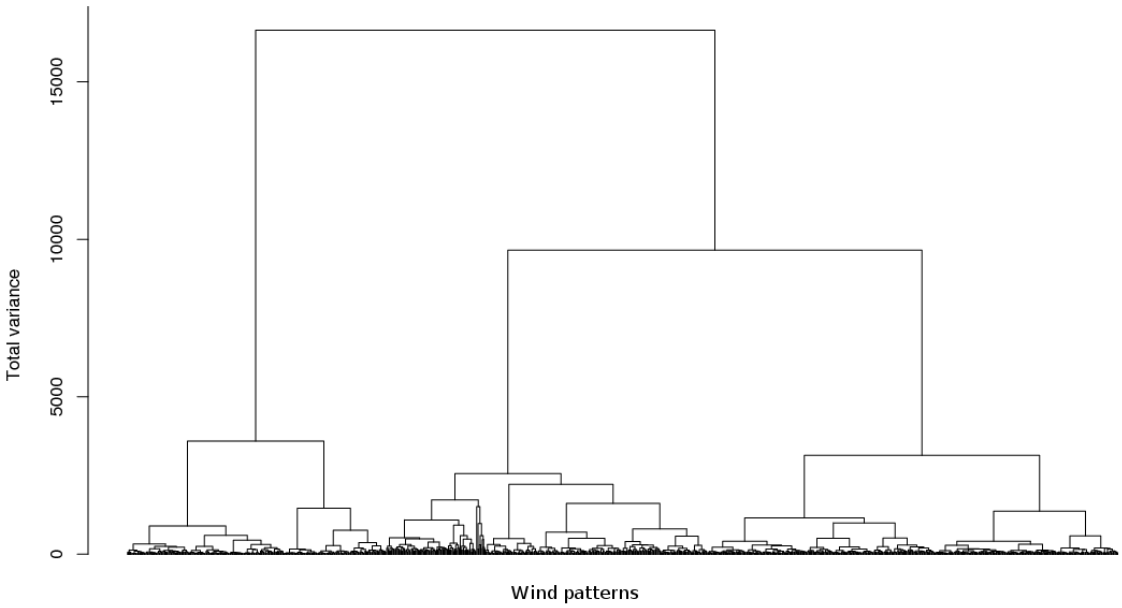

Figure 5.17: Cluster dendrogram of successive aggregations between the wind patterns considering BOLAM 7 model.

also distributed in the same way as for the wind: one cluster in winter and the other two in summer.

To have a deeper understanding of the three obtained clusters both for the wind and for the current data sets, the components of the horizontal velocity are recovered and the corresponding average vectors, i.e. the vectors of the average components, are calculated for every cluster. In the following, the resulting current regimes together with the corresponding wind forcing (i.e. wind cluster with the more similar monthly distribution) are shown. In particular, only the current regimes with no-wind forcing, BOLAM 21 and BOLAM 7 wind forcing with the variable C_D value are showed. The results obtained with the constant value of C_D are quite similar to the no-wind forcing results.

The average wind field in cluster $w1$ (Fig. 5.20 A) corresponding to the winter regime, comes from north-east direction. The current cluster $c1$ corresponds to winter regime and in every scenario it is characterized by a strong signal over the all domain and associated with high average current speeds toward the north-west. In the lee of the cape, considering the no-wind (Fig. 5.20 B) and BOLAM 21 forcing (Fig. 5.20 C) the eddy is not present or not well developed as in the case of BOLAM 7 forcing (Fig. 5.20 D).

For the summer regimes, the wind cluster $w2$ (Fig. 5.21 A) shows an intense wind blowing from the south-east. In regard to the current clusters, for the no-wind forcing experiment (Fig. 5.21 B), cluster $c2$ is characterized by a westward transport more intense near the coast. In the experiments with the wind forcing, a countercurrent in the south-east direction is present in-shore and the average current amplitude is higher with BOLAM 7 wind forcing (Fig. 5.21 D) than with BOLAM 21 wind forcing (Fig. 5.21 C).

The wind structure in cluster $w3$ (Fig. 5.22 A) is not constant within the domain, following an anticyclonic rotation of the wind which blows from the north-east in the eastern part of the domain and from the south-east in the western part. Note that the average wind is weaker than in the previous cases. The current cluster $c3$ is characterized by an intense current off-shore, which can be observed in every simulated scenario. Considering wind forcing, a weak coastal countercurrent is formed and considering BOLAM 7 wind forcing (Fig. 5.22 D), this countercurrent is more intense than with BOLAM 21 wind forcing (Fig. 5.22 C), especially

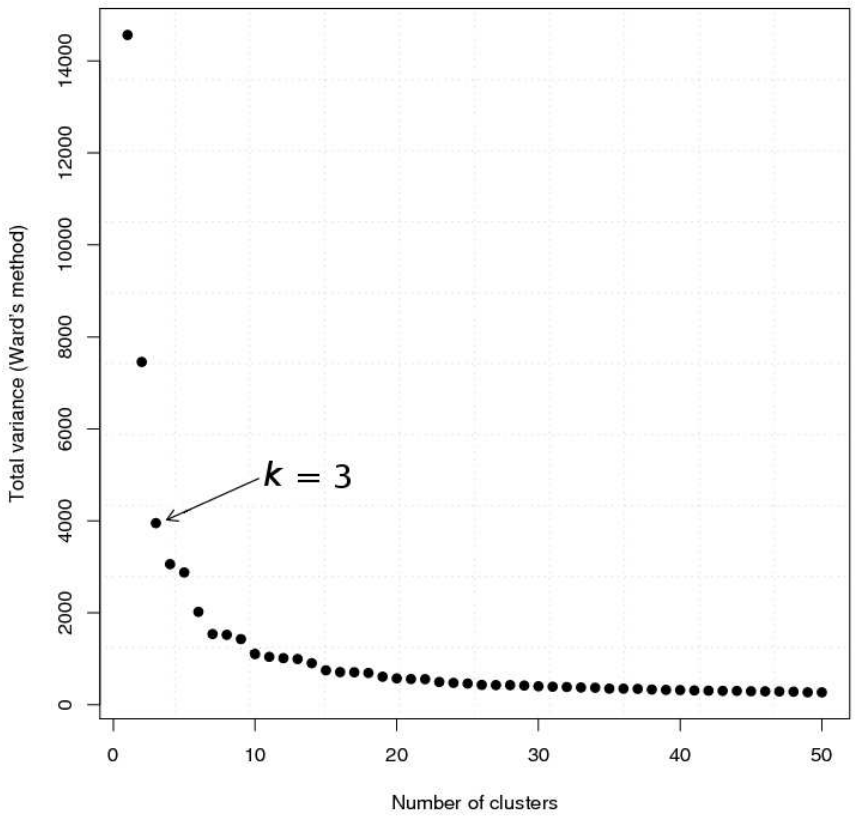

Figure 5.18: Sum of cluster variances. Values of the total variance corresponding to successive cluster merging for the last 50 aggregations, for the wind data set considering BOLAM 7 model.

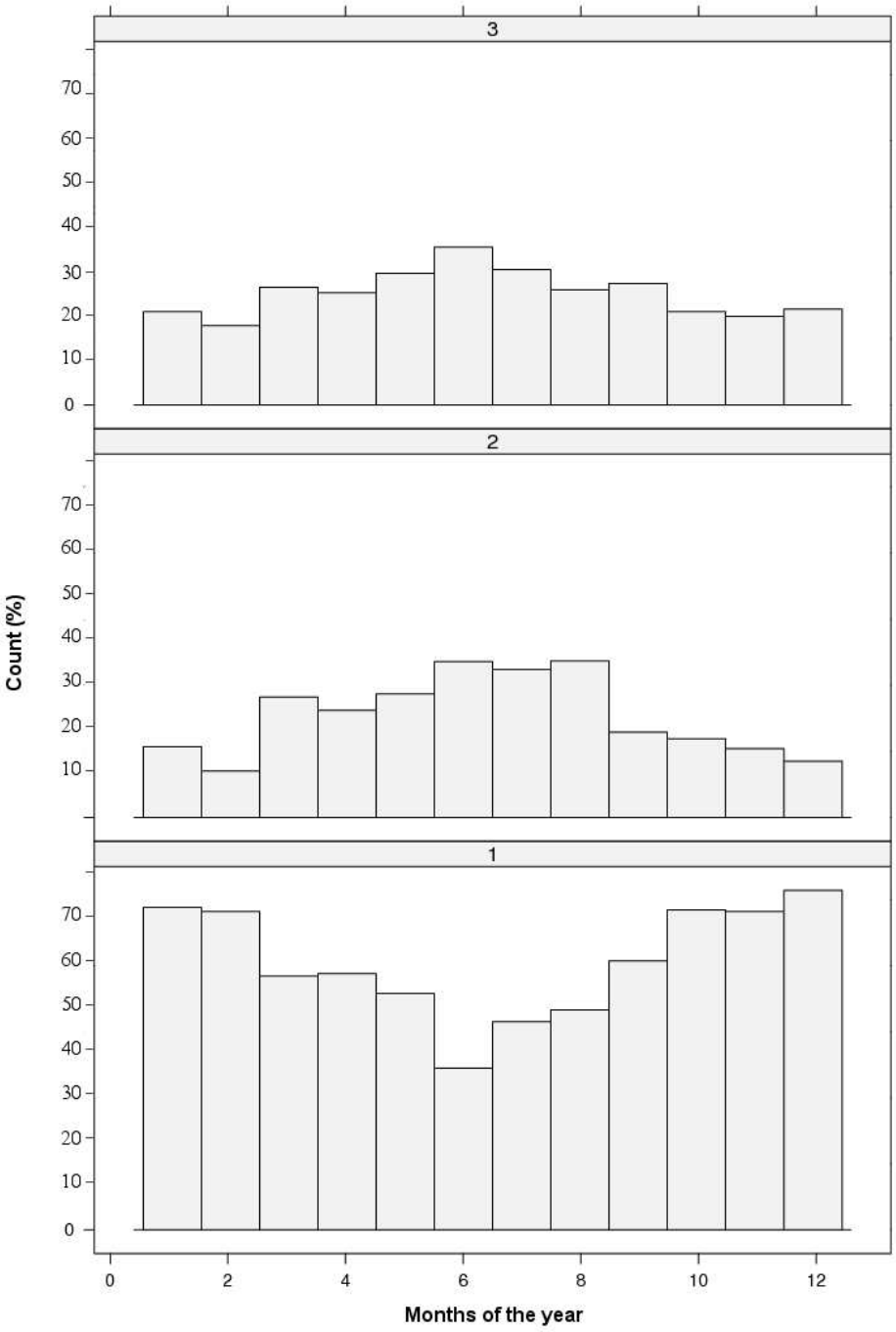

Figure 5.19: Monthly distributions of the three BOLAM 7 wind clusters corresponding to $k = 3$ and representing the mean wind regimes in the area under study.

around the cape.

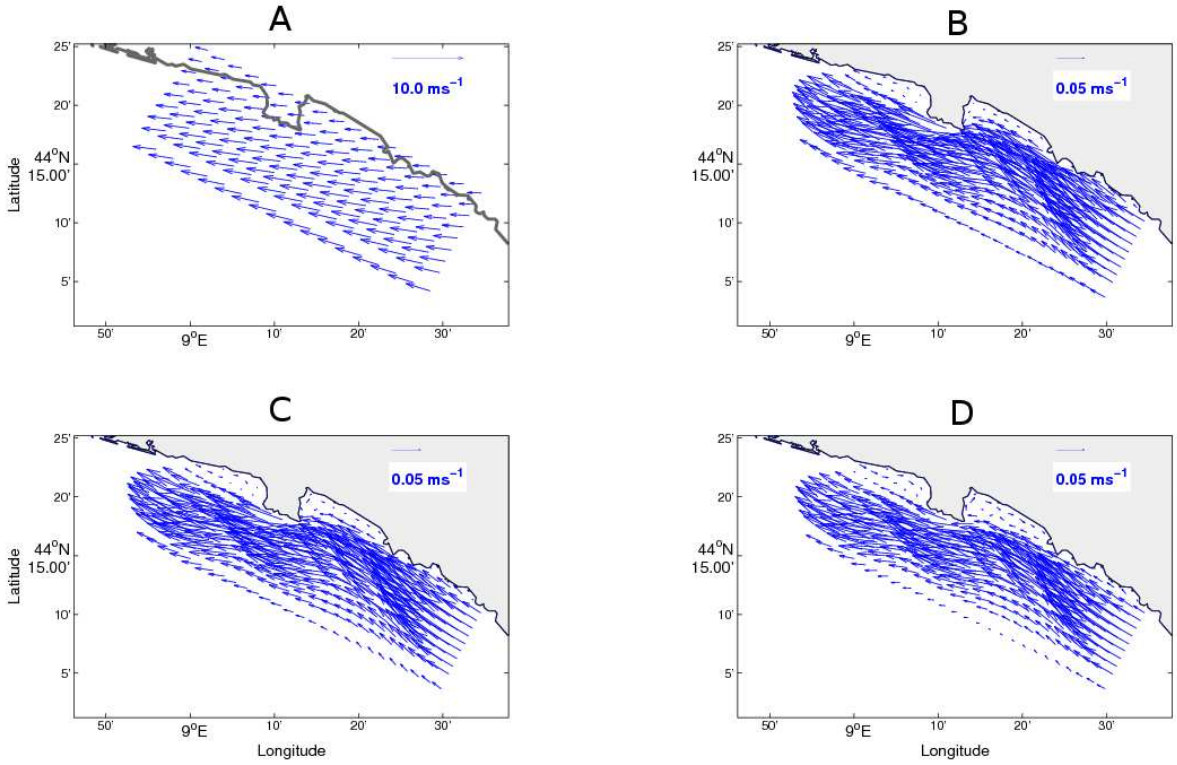

Figure 5.20: Average wind vectors of cluster $w1$ considering BOLAM 7 model (A) and the average current vectors of cluster $c1$ considering no-wind forcing (B), BOLAM 21 forcing with the variable C_D value (C) and BOLAM 7 forcing with the variable C_D value (D).

5.3 Discussion

In the studied area, the local winds are strongly influenced by the complex topography of the zone (Bruschi and Manzella, 1980; Pinardi and Masetti, 2000). The BOLAM 7 model uses an orography with a three times greater resolution than BOLAM 21 and it permits to better resolve the local wind circulation of the area. Indeed, using this model, the southerly winds are more frequent and the events of southwesterly wind are also better resolved. Moreover, the winds blowing from the north is rotated in the east direction in the eastern part of the domain because the presence of the cape deflects these winds. This detailed feature is not reproduced by the BOLAM 21 model. Because of the land and sea mask discussed previously, the wind amplitude is underestimated in both models.

In regard to the water circulation, at the same position of station 5, Astraldi and Manzella (1983) measured the current amplitude and direction with a currentmeter array providing annual mean values at 16, 50 and 95 m. In order to provide a qualitative comparison between the *in situ* data and the model outputs, we can compute, from these data, depth-averaged annual values of -15.7 and 0.3 cm s^{-1} for along-shore (positive towards the south-east) and cross-shore (positive towards the north-east) components, respectively. The comparison can be only qualitative because the data are measured by Astraldi and Manzella (1983) many years ago and moreover, we consider a 2D model. Comparing the model outputs and the *in situ* data, the modeled current results are underestimated. This is mainly due to two reasons: the Symphonie current

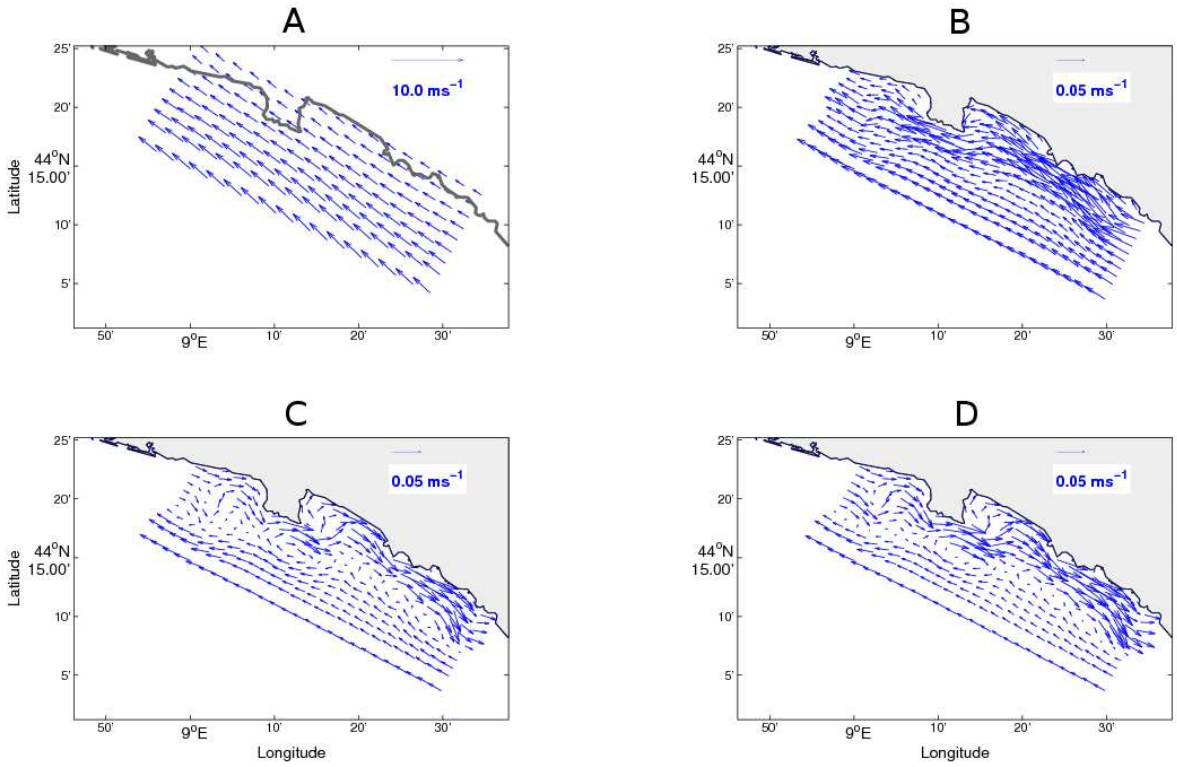

Figure 5.21: As Fig. 5.20 for the wind cluster $w2$ and the current clusters $c2$.

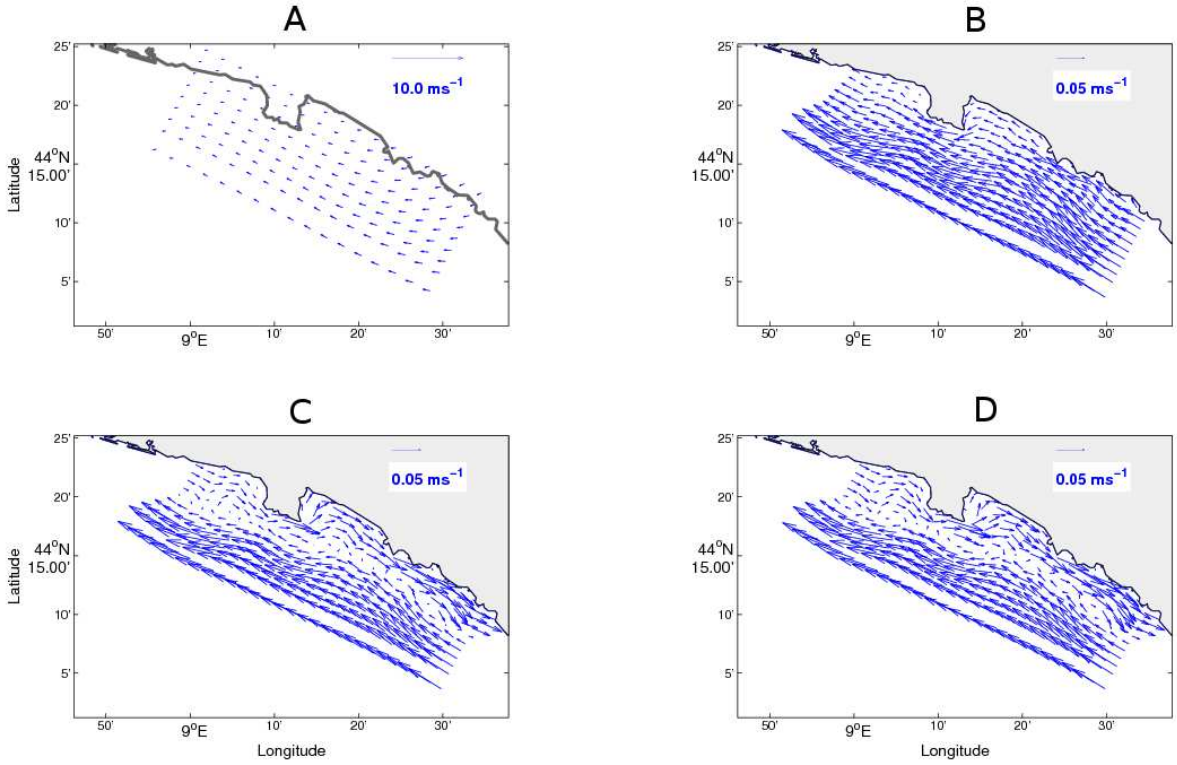

Figure 5.22: As Fig. 5.20 for the wind cluster $w3$ and the current clusters $c3$.

outputs used at the incoming boundary are less intense than the *in situ* data and the modeled wind intensity used as forcing is underestimated.

However, in this study, the coastal model well reproduces the barotropic, north-westward along-shore transport presented in the observations (Bruschi and Manzella, 1980). Periods of flow reversal associated with southerly winds (Astraldi and Manzella, 1983) and the presence of anticyclonic eddies around the cape (Doglioli et al., 2004a) are also simulated. Moreover, since the primary aim of this study is an assessment of the importance of the higher resolution wind forcing on the coastal circulation and its effect is greater near the coast where the dynamic is two-dimensional, this modelling tool has proved successful.

The greater effects of the higher resolution wind forcing near the coast is also highlighted considering the variations of the average specific kinetic energy. Indeed, it is maximum in the two in-shore zones and especially in the in-shore western zone, where the eddy is observed. In fact, the higher resolution wind forcing plays an important role in resolving current separation and eddy formation, resulting in an intensification of the recirculations.

Considering the annual average mass transport through section A (Fig. 5.2), the greater transport is found in the experiment considering BOLAM 7 wind forcing with the variable C_D value, implying an eddy intensification. Also the countercurrent associated with the southerly winds is more intense considering the higher resolution wind forcing.

Considering the drag coefficient value varying with wind intensity, an increase of the current intensity, especially in the coastal area, is generally observed. So, for example, the exceptional events of southwesterly wind are crucial in producing an intensification of the countercurrent and eddy recirculations. Indeed, the effect of these winds on the circulation can not be appreciated in the experiments with the constant drag coefficient because, since having a strong intensity, they are very rare. The presence of the countercurrent in the eastern Ligurian Sea is already observed by several authors (Bruschi and Manzella, 1980; Esposito and Manzella, 1982) but unfortunately there are no measurements in this area near the coast. Moreover, the only *in situ* data available (Astraldi and Manzella, 1983), do not distinguish between current and countercurrent contributions to the average values, so that it is not possible to state what forcing is the most realistic one. With our results, it is highlighted that the countercurrent is mainly due to the wind forcing. A further confirmation of this conclusion is that Doglioli et al. (2004a), not considering the wind forcing, do not observed the coastal countercurrent in east direction. So, it is reasonable to suppose that the higher resolution wind forcing gives more reliable description of the characteristics of the countercurrent.

Moreover, in order to highlight the differences occurring in the current circulation considering different wind forcings, the cluster analysis on the wind data sets and then on the current ones is performed. The methodology already tested and verified with wind data (Burlando, 2008; Burlando et al., 2008) is followed in order to identify the main local regimes. The same seasonality both for the wind and the current patterns is found, corresponding to one winter and two summer scenarios. This seasonal variability of the Ligurian circulation is also shown in several works in the area (Astraldi et al., 1990; Astraldi and Gasparini, 1992; Astraldi et al., 1994; Echevin et al., 2002).

The cluster analysis on the wind and current data is performed independently on the different data sets and I find that the results are fluid-dynamically coherent. The winter regime is characterized by the wind blowing from the north-east. Considering the theoretical Ekman transport relation, which predicts that the wind stress produces a transport of water to the right of the wind in the northern hemisphere, the resulting current flows north-westward. This produces an intensification of the general northwestward transport. And, indeed, the winter current cluster $c1$ is characterized by this situation (Fig. 5.20).
It is worth noting that the wind in the winter regime is more rotates eastward than shown by the wind roses (Fig. 5.11). This because, the average wind is the mean of the components of the wind patterns and, since the wind blowing from the north-northeast is very frequent and its patterns distribution is not symmetric, the mean and the mode values do not coincide.
In the summer regimes, the wind blows from the southeast producing a water accumulation against the coast upwind the cape. This water accumulation creates a pressure gradient from the coast to off-shore. The balance of the Ekman transport due to the wind and the pressure gradient give rise to the southeastward countercurrent shown in the summer clusters (Fig. 5.21 and Fig. 5.22). Moreover lee the cape, the eddy

presence creates the southeastward current that is shown in Fig. 5.21 and Fig. 5.22 too.
For these reasons, we consider the wind and the current regimes, determinated by the cluster analysis, are fluid-dynamic coherent. Moreover, the cluster analysis highlights that the coastal circulation in this area is driven by the wind and that the wind resolution has a strong effect on the currents near the coast.

5.4 Conclusions

As far as the numerical aspect of the present investigation, it provides a contribution in two different directions: on the one hand, it contributes to our understanding of the role played by the wind resolution to resolve coastal circulation and eddy generation mechanism in presence of shelf and steep slope; on the other hand, it provides indications on the appropriate model configuration and parameter ranges to be used as a basis for future realistic modelling of the specific area.

Indeed, the results of the high-resolution coastal circulation model forced by the two versions of the atmospheric model BOLAM, well reproduces the observed north-westward along-shore transport and the periods of flow reversal in-shore associated with southerly winds. Moreover, the presence of anticyclonic eddies around the north-western side of the cape are also simulated. It is shown that the wind forcing plays a key role in enhancing the coastal dynamics and the eddy formation around the cape. Indeed, an intensification of the eddy and countercurrent formation is observed with the higher resolution wind forcing.

Both the specific average kinetic energy and the annual average mass transport show an intensification of the eddy downstream of the cape and of the countercurrent. These effects are mainly due to the resolution of the orography used in the wind-forcing model.
In the case of high resolution wind, the effect of the variable value of the drag coefficient with the wind speed has a great impact in-shore and causes an intensification of the countercurrent and of the eddy.

The performed cluster analysis highlights the season variability of the studied area. One winter and two summer regimes both for the wind and for the current patterns are found. The winter regime is characterized by the presence of northeasterly winds that reinforce the general northwestward circulation. The formation of the eddy downstream of the cape can be observed considering the higher resolution wind forcing.
During the summer regimes, the countercurrent, associated to the southeasterly winds, appears only if the wind forcing is taken into account. As a conclusion, it can be stated that in coastal areas characterized by complex topography, the higher resolution wind forcing plays a fundamental role to accurately resolve the coastal circulation especially near the coast.

Moreover, the most important coastal circulation patterns of this area, identified through a cluster analysis of the simulated flow fields, turn out to be significantly sensitive to the parameterization chosen for describing the wind-sea interaction, so that there is a real need for future systematic testing and comparison of numerical model results with measurement data.

6

Conclusions

In the present work, original and innovative answers to the three scientific questions are given. The questions regard the effect of degradation and local Mediterranean conditions on the aquaculture impact assessment and the role played by the wind and its resolution on coastal circulation. The coastal waters belonging to the Marine Protected Area of the Promontorio of Portofino in the eastern Ligurian Sea (northwestern Mediterranean) are taken into account. In this area, several activities and interests converge and, in the light of its great natural and touristic value, many conflicts are arisen. Therefore, it is necessary a careful management of the coastal zone pushing through an accuracy knowledge of the involved processes.

In this dissertation, firstly, the possible impacts correlate to the marine fish farm is analyzed. Indeed, in chapter 3 the environmental problems due to the cages are introduced. Aquaculture is the food-related activity with the most rapid growth in the world. Since this growth produces an immediate concern, it is necessary to develop tools to predict the environmental impacts coming from intensive marine fish farms. Moreover, following only the fate of the aquaculture waste is not sufficient to correctly assess the organic load on the sea bottom. The modeling effort should consider the natural capability of the benthic environment in reacting and absorbing fluctuations in the organic load. For this reason, the capability of the POM-LAMP3D model has been improved including both a more realistic advection-dispersion setup and a new benthic model, the Finite Organic Accumulation Module (FOAM). This module computes the sediment stress level based on the ratio between the quantity of oxygen supplied to the sediment carried by current on the bottom, and the quantity of oxygen demanded by the sediment for the organic carbon degradation (Findlay and Watling, 1997). Several simulations are carried out switching suitable parameters such as: i) the waste typologies (uneaten feed or faecal particles), ii) the release conditions (continuous or twice a day) and iii) the particle chemical-physical characteristics (settling velocity) depending on the reared fish and the hydrology of the site where the fish farm is located (in this case Sea Bass and Gilthead Sea Bream reared in the Mediterranean Sea, Vassallo et al., 2006; Magill et al., 2006). The obtained results confirm that uneaten feed is the primary cause of ecological impact on the sediment, according to Beveridge et al. (1991) and Vezzulli et al. (2003), while faecal waste are almost completely degraded. Furthermore, the maximum impacts, in terms of both stress level and organic carbon concentration, are due to the quickly settling feed, released in periodical mode and during slow current periods. These results support the use of self-feeders that are already proposed by several authors (e.g. Azzaydi et al., 1998) in order to reduce uneaten feed losses with no effect on growth rates. Therefore, the new and more complete modelling framework here presented is able to improve the objectivity in decision making processes and it may be successfully used for planning and monitoring purposes.

Anyway, in order to further improve the prediction capability of the model framework, specific in-situ measurements are required for evaluate the values of the mineralization rates and bethic metabolism in typical Mediterranean conditions. Indeed, the different mineralization rates reflect the sediment stress levels and are used to compute the organic carbon concentration remaining on the seabed after degradation. The determination of the mineralization rates and the benthic metabolism activity is a key parameter in the accuracy of the model prediction. Nevertheless, the lack in literature of these values, specifically targeting

Mediterranean conditions motivate us to perform two sampling campaigns in a typical Mediterranean fish farm in the warm and cold season of 2006. In chapter 4, the description of the farm chosen for the *in situ* measurements and the methodology of sampling and analysis of the samples are described.

Biodepositon rates, background sedimentation, benthic O_2 respiration and CO_2 production are measured. Unlike what observed in Atlantic conditions (Findlay and Watling, 1997), in the Mediterranean ones, the benthic response to the organic enrichment of the bottom depends on water temperature. Moreover, three different sediment state categories on the basis of the respiratory quotient (Dilly, 2003) are distinguished. New simulations with the measured Mediterranean parameters are performed considering two macro-periods, warm and cold season in the same Ligurian fish farm considered in the previous chapter. Organic degradation for both uneaten feed and faeces is evaluated by changing release modality (continuous and periodical) and by varying the settling velocities. The new FOAM simulations better reproduce the nutrient load on the seabed than the ones of the previous chapter in which the Atlantic parameterization is used. The new setup leads to more realistic results that confirm what already assessed in chapter 3: the feed particles are the primary cause of ecological impact to the benthos community and the more frequent conditions of high sediment stress level and the higher values of organic carbon concentration on the seabed are due to the feed particles released in periodical mode (twice in a day).

Furthermore, the new results clearly indicate different pathways, temperature dependent, of carbon oxidation, with higher oxygen demand, measured in warm season, associated to the same carbon input. Moreover, the extension of the impacted area and the organic carbon concentration remaining on the seabed vary seasonally, with a contraction in the warm period while in this season it is maximum the frequency of the high stress level of sediment. The modelling framework can therefore represent an important tool in decision making processes, for planning and monitoring purposes. Managers and policy makers may take care of these differences in planning the installation of new fish farms or the expansion of existing ones. A balance among the organic matter spread or load and the occurrence of different sediment states may be accurately evaluated with the application of the model.

Therefore, it would be very interesting to systematically characterize the Mediterranean fish farms applying the entire model POM-LAMP3D and FOAM to several sites. Moreover, several sampling campaigns should be carried out in order to obtain a whole range of variations of FOAM parameters with temperature and improve the prediction capability of the model. It is in fact expected that parameters may continuously vary with water temperature allowing a more reliable model setup in function of detected (or expected) water temperature. At this purpose, further field experiments are needed to completely characterize the metabolic dynamics of sediments covering the whole range of Mediterranean Sea temperatures.

In chaper 5 the attention is focused on the improvements of the coastal circulation model because, as discussed in the chapter 1, it influences the dispersion of the waste and the state of the sediment.

As far as the numerical aspect of this chapter, it provides a contribution in two different directions: on the one hand, it contributes to our understanding of the role played by the wind resolution to resolve coastal circulation and eddy generation mechanism in presence of shelf and steep slope; on the other hand, it provides indications on the appropriate model configuration and parameter ranges to be used as a basis for future realistic modelling of the specific area.

The wind forcing and topographic features as headlands and capes play a key role on the shallow water hydrodynamics. Moreover, the variability of the wind speed and wind stress curl in coastal areas is associated with the observed variability of the instabilities around promontories. Moreover, it is well-known that in areas with a complex orography it strongly influence the local wind and consequently the coastal dynamics.

This chapter is aimed to assess the role of the wind stress and its resolution on the coastal circulation and, in particular, on the eddy formation around the Promontorio of Portofino. The circulation between 2001 to 2003 is simulated by the coastal-circulation high-resolution numerical model POM, coupled with the atmospheric mesoscale model BOLAM in its two version: BOLAM 21 with a horizontal resolution of 21 km and BOLAM 7 with a horizontal resolution of 7 km. Moreover at the incoming boundary, the outputs of the regional model Symphonie are used, thus being able to reproduce the seasonal variability of the current. The effect of using different values of the drag coefficient in the bulk formula for the computation of the wind stress is also tested. Finally, a cluster analysis is performed to distinguish the main wind and coastal-flow patterns in the area under study.

The results well reproduce the observed north-westward along-shore transport and the periods of flow

reversal in-shore associated with southerly winds. Moreover, the presence of anticyclonic eddies around the north-western side of the cape are also simulated. It is shown that the wind forcing plays a key role in enhancing the coastal dynamics and the eddy formation around the cape. Indeed, an intensification of the eddy and countercurrent formation is observed with the higher resolution wind forcing. Moreover, in the case of high resolution wind, the effect of the variable value of the drag coefficient with the wind speed has a great impact in-shore and causes a further intensification of the countercurrent and the eddy.

The observed season variability of the area (Astraldi et al., 1990, 1994) is reproduced by the results of the cluster analysis. Indeed, one winter and two summer regimes both for the wind and for the current patterns are found. The winter regime is characterized by the presence of northeasterly winds that reinforce the general northwestward circulation. The formation of the eddy downstream of the cape can be observed considering the higher resolution wind forcing. During the summer regimes, the countercurrent, associated to the southeasterly winds, appears only if the wind forcing is taken into account.

As a conclusion, it can be stated that in coastal areas characterized by complex topography, the higher resolution wind forcing plays a fundamental role to accurately resolve the coastal circulation especially near the coast. For this reason, the use of an atmospheric model with even higher resolutions than in the present study, will be considered in future developments. In order to specifically analyze the eddy characteristics, a three dimensional description of the circulation will be taken into account. Moreover, the most important coastal circulation patterns of this area, identified through a cluster analysis of the simulated flow fields, turn out to be significantly sensitive to the parameterization chosen for describing the wind-sea interaction, so that there is a real need for future systematic testing and comparison of numerical model results with measurement data.

A

Appendix A - Numerical models

A.1 Priceton Ocean Model

POM (Priceton Ocean Model) is a three-dimensional, primitive equation, time-dependent, σ coordinate, free surface estuarine and coastal ocean circulation model, incorporating a turbulence closure model to provide a realistic parameterization of the vertical mixing processes.
It is developed initially by Blumberg and Mellor (1987) with successively contributions by several authors. It is free distributed on-line with its FORTRAN code (http://www.aos.princeton.edu/WWWPUBLIC/htdocs.pom/). The principal attributes of the model are as follows:

- It contains an imbedded second moment turbulence closure sub-model to provide vertical mixing coefficients.
- It is a sigma coordinate model in that the vertical coordinate is scaled on the water column depth.
- The horizontal grid uses curvilinear orthogonal coordinates and an "Arakawa C" differencing scheme.
- The horizontal time differencing is explicit whereas the vertical differencing is implicit. The latter eliminates time constraints for the vertical coordinate and permits the use of fine vertical resolution in the surface and bottom boundary layers.
- The model has a free surface and a split time step. The external mode portion of the model is two-dimensional and uses a short time step based on the CFL condition and the external wave speed. The internal mode is three-dimensional and uses a long time step based on the CFL condition and the internal wave speed.
- Complete thermodynamics have been implemented.

The prognostic variables are the three components of the velocity field, temperature, salinity and two quantities which characterize the turbulence, the turbulence kinetic energy and the turbulence macroscale. The momentum equations are nonlinear and incorporate a variable Coriolis parameter. Frognostic equations governing the thermodynamic quantities, temperature and salinity account for water mass variations brought about by highly time-dependent coastal upwelling processes as well as horizontal advective processes. Free surface elevation is also calculated prognostically, with only some sacrifice in computational time so that tides and storm surge events can also be simulated. This is accomplished by use of a mode splitting technique whereby the volume transport and vertical velocity shear are solved separately. Other computer variables include the density, vertical eddy viscosity and vertical eddy diffusivity. The model also accommodates realistic coastline geometry and bottom topography.

A.1.1 Governing equations

The equations which form the basis of the circulation model describe the velocity and surface elevation fields, and the salinity and temperature fields. Two simplifying approximations are used:

- first, it is assumed that the weigh of the fluid identically balances the pressure (hydrostatic assumption),
- second, density differences are neglected unless the differences are multiplied by gravity (Boussinesq approximation).

Consider a system of orthogonal Cartesian coordinates with x increasing eastward, y increasing northward and z increasing vertically upwards. The free surface is located at $z = \eta(x, y, t)$ and the bottom is at $z = -H(x, y)$. If $\mathbf{v}$ is the horizontal velocity vector with components (u,v) and ∇ the horizontal gradient operator, the continuity equation is

$$\nabla \cdot \mathbf{v} + \frac{\partial w}{\partial z} = 0 \tag{A.1}$$

The Reynolds momentum equations are

$$\frac{\partial u}{\partial t} + \mathbf{v} \cdot \nabla u + w\frac{\partial u}{\partial z} - fv = -\frac{1}{\rho_0}\frac{\partial p}{\partial x} + \frac{\partial}{\partial z}\left(K_M \frac{\partial u}{\partial z}\right) + F_x \tag{A.2}$$

$$\frac{\partial v}{\partial t} + \mathbf{v} \cdot \nabla v + w\frac{\partial v}{\partial z} + fu = -\frac{1}{\rho_0}\frac{\partial p}{\partial y} + \frac{\partial}{\partial z}\left(K_M \frac{\partial v}{\partial z}\right) + F_y \tag{A.3}$$

$$\rho g = -\frac{\partial p}{\partial z} \tag{A.4}$$

with ρ_0 the reference density, ρ the in situ density, g the gravitational acceleration, p the pressure, K_M the vertical eddy diffusivity of turbulent momentum mixing. A latitudinal variation of the Coriolis parameter, f, is introduced by use of the β plane approximation.
The pressure at depth z can be obtained by integrating the vertical component of the equation of motion, Eq. (A.4), from z to the free surface η, and is

$$p(x, y, z, t) = p_{atm} + g\rho_0\eta + g\int_z^0 \rho(x, y, z', t)dz' \tag{A.5}$$

Henceforth, the atmospheric pressure, p_{atm} is assumed constant. The conservation equations for temperature and salinity may be written as

$$\frac{\partial \Theta}{\partial t} + \mathbf{v} \cdot \nabla \Theta + w\frac{\partial \Theta}{\partial z} = \frac{\partial}{\partial z}\left(K_H \frac{\partial \Theta}{\partial z}\right) + F_\Theta \tag{A.6}$$

$$\frac{\partial S}{\partial t} + \mathbf{v} \cdot \nabla S + w\frac{\partial S}{\partial z} = \frac{\partial}{\partial z}\left(K_H \frac{\partial S}{\partial z}\right) + F_S \tag{A.7}$$

where Θ is the potential temperature (or in situ temperature for shallow water applications) and S is the salinity. The vertical eddy diffusivity for turbulent mixing of heat and salt is denoted as K_H. Using the temperature and salinity, the density is computed according to an equation of state of the form

$$\rho = \rho(\Theta, S) \tag{A.8}$$

The potential density is ρ, that is, the density evaluated as a function of potential temperature and salinity but at atmospheric pressure; it provides accurate density information to calculate horizontal baroclinic gradients which enter in the pressure gradient terms and the vertical stability of the water column which enters into the turbulence closure model even in deep water when pressure effects become important.

All of the motions induced by small-scale processes not directly resolved by the model grid (subgrid scale) is parameterized in terms of horizontal mixing processes. The terms F_x, F_y, F_Θ and F_S in Eq. (A.2), Eq. (A.3), Eq. (A.6) and Eq. (A.7) represent these unresolved processes and in analogy to molecular diffusion can be written as

$$F_x = \frac{\partial}{\partial x}\left[2A_M\frac{\partial u}{\partial x}\right] + \frac{\partial}{\partial y}\left[A_M\left(\frac{\partial u}{\partial y} + \frac{\partial v}{\partial x}\right)\right] \tag{A.9}$$

$$F_y = \frac{\partial}{\partial y}\left[2A_M\frac{\partial v}{\partial y}\right] + \frac{\partial}{\partial x}\left[A_M\left(\frac{\partial u}{\partial y} + \frac{\partial v}{\partial x}\right)\right] \tag{A.10}$$

and

$$F_{\Theta,S} = \frac{\partial}{\partial x}A_H\frac{\partial(\Theta,S)}{\partial x} + \frac{\partial}{\partial y}A_H\frac{\partial(\Theta,S)}{\partial y} \tag{A.11}$$

Note that F_x and F_y are invariant to coordinate rotation. While, these horizontal diffusive terms are meant to parameterize subgrid scale processes, in practice the horizontal diffusivities, A_M and A_H, are usually required to damp small-scale computational noise. The form of F_x, F_y and $F_{\Theta,S}$ allows for variable A_M and A_H but thus far they have been held constant. The diffusivities are chosen so that they do not produce excessive smoothing of real features. Values as low as 10 m^2s^{-1} have been used successfully in various applications. The relatively fine vertical resolution used in the applications resulted in a reduced need for horizontal diffusion because horizontal advection followed by vertical mixing effectively acts like horizontal diffusion in a real physical sense. An enhancement, now in progress, is to relate A_M and A_H to the scales of motion being resolved in the model and to the local deformation field as suggested by Smagorinsky (1963).

A.1.2 Turbulence closure

The governing equations contain parameterized Reynolds stress and flux terms which account for the turbulent diffusion of momentum, heat and salt. The parameterization of turbulence in the model is based on the work of Mellor and Yamada (1974).
The vertical mixing coefficients, K_M and K_H, in Eq. (A.2), Eq. (A.3), Eq. (A.6) and Eq. (A.7) are obtained by appealing to a second order turbulence closure scheme (Mellor and Yamada, 1982) which characterizes the turbulence by equations for the turbulence kinetic energy, $\frac{q^2}{2}$, and a turbulence macroscale, ℓ, according to,

$$\begin{aligned}\frac{\partial q^2}{\partial t} + \mathbf{v}\cdot\nabla q^2 + w\frac{\partial q^2}{\partial z} = \frac{\partial}{\partial z}\left(K_q\frac{\partial q^2}{\partial z}\right) \quad + \\ 2K_M\left[\left(\frac{\partial u}{\partial z}\right)^2 + \left(\frac{\partial v}{\partial z}\right)^2\right] \quad + \quad \frac{2g}{\rho_0}K_H\frac{\partial \rho}{\partial z} - \frac{2q^3}{B_1\ell} + F_q\end{aligned} \tag{A.12}$$

and

$$\begin{aligned}\frac{\partial q^2\ell}{\partial t} + \mathbf{v}\cdot\nabla(q^2\ell) + w\frac{\partial q^2\ell}{\partial z} = \frac{\partial}{\partial z}\left(K_q\frac{\partial q^2\ell}{\partial z}\right) \quad + \\ \ell E_1 K_M\left[\left(\frac{\partial u}{\partial z}\right)^2 + \left(\frac{\partial v}{\partial z}\right)^2\right] \quad + \quad \frac{\ell E_1 g}{\rho_0}K_H\frac{\partial \rho}{\partial z} - \frac{q^3}{B_1}\widetilde{w} + F_\ell\end{aligned} \tag{A.13}$$

where a wall proximity function is defined as

$$\widetilde{w} \equiv 1 + E_2 \left(\frac{\ell}{kL} \right)^2 \tag{A.14}$$

and where

$$L^{-1} \equiv (\eta - z)^{-1} + (H + z)^{-1} \tag{A.15}$$

Near surfaces it may be shown that both ℓ/k and L are equal to the distance from the surface (k = 0.4 is the von Karman constant) so that $\widetilde{w} = 1 + E_2$. Far from the surfaces where $\ell << L$, $w^2 \cong 1$. The length scale provided by Eq. (A.13) is a characteristic length of the turbulent motion at any point in space or time. An alternative to Eq. (A.13) is to use a transport equation for the dissipation rate. The former approach according to Mellor and Yamada (1982) is more consistent since it uses an equation which describes large-scale turbulence to determine the turbulent macroscale. The terms F_q and F_ℓ in Eq. (A.12) and Eq. (A.13) are the horizontal mixing and are parameterized analogously to temperature and salinity by using Eq. (A.11).

While details of the closure model are rather involved, it is possible to reduce the prescription of the mixing coefficients K_M, K_H and K_q to the following expressions,

$$K_M \equiv \ell q S_M \tag{A.16}$$

$$K_H \equiv \ell q S_H \tag{A.17}$$

$$K_q \equiv \ell q S_q \tag{A.18}$$

The stability functions, S_M, S_H and S_q are analytically derived, algebraic relations functionally dependent upon $\frac{\partial u}{\partial z}$, $\frac{\partial v}{\partial z}$, $g\rho_0 \frac{\partial \rho}{\partial z}$, q and ℓ. These relations derive from closure hypotheses described by Mellor and Yamada (1982).

A.1.3 Boundary conditions

The boundary conditions at the free surface, $z = \eta(x, y)$, are

$$\rho_o K_M \left(\frac{\partial u}{\partial z}, \frac{\partial v}{\partial z} \right) = (\tau_{0x}, \tau_{0y}) \tag{A.19}$$

$$\rho_o K_H \left(\frac{\partial \Theta}{\partial z}, \frac{\partial S}{\partial z} \right) = (\dot{H}, \dot{S}) \tag{A.20}$$

$$q^2 = B_1^{2/3} u_{\tau s}^2 \tag{A.21}$$

$$q^2 \ell = 0 \tag{A.22}$$

$$w = u \frac{\partial \eta}{\partial x} + v \frac{\partial \eta}{\partial y} + \frac{\partial \eta}{\partial t} \tag{A.23}$$

where (τ_{0x}, τ_{0y}) is the surface wind stress vector with the friction velocity, $u_{\tau s}$, the magnitude of the vector. It is doubtful that the mixing length goes to zero at a surface containing wind induced waves as suggested by

Eq. (A.22). The error is incurred in the near surface layers of thickness of order of the wave height. This is an area where further improvement is necessary. The quantity $B_1^{2/3}$ is an empirical constant (6.51) arising from the turbulence closure relations. The net ocean heat flux is $\dot{H}$ and here $\dot{S} \equiv S(0)[\dot{E} - \dot{P}]/\rho_0$ where $(\dot{E} - \dot{P})$ is the net evaporation-precipitation fresh water surface mass flux rate and $S(0)$ is the surface salinity.
On the side walls and bottom of the basin, the normal gradients of Θ and S are zero so that there are no advective and diffusive heat and salt fluxes across these boundaries. At the lower boundary (b),

$$\rho_o K_M \left(\frac{\partial u}{\partial z}, \frac{\partial v}{\partial z} \right) = (\tau_{bx}, \tau_{by}) \tag{A.24}$$

$$q^2 = B_1^{2/3} u_{\tau b}^2 \tag{A.25}$$

$$q^2 \ell = 0 \tag{A.26}$$

$$w_b = -u_b \frac{\partial H}{\partial x} - v_b \frac{\partial H}{\partial y} \tag{A.27}$$

where $H(x, y)$ is the bottom topography and $u_{\tau b}$ is the friction velocity associated with the bottom frictional stress (τ_{bx}, τ_{by}). The bottom stress is determined by matching velocities with the logarithmic law of the wall. Specifically,

$$\boldsymbol{\tau}_b = \rho_0 C_D \left| \mathbf{v}_b \right| \mathbf{v}_b \tag{A.28}$$

with value of the drag coefficient C_D given by

$$C_D = \left[\frac{1}{k} \frac{ln(H + z_b)}{z_0} \right]^{-2} \tag{A.29}$$

where z_b and $\mathbf{v}_b$ are the grid point and corresponding velocity in the grid point nearest the bottom and k is the von Karman constant. The final result of Eq. (A.28) and Eq. (A.29) in conjunction with the turbulent closure derived K_M is that the calculations will yield

$$\mathbf{v} = \left(\frac{\boldsymbol{\tau}_b}{k u_{\tau b}} \right) ln \left(\frac{z}{z_0} \right) \tag{A.30}$$

in the lower boundary region if enough resolution is provided. In those instances where the bottom boundary layer is not well resolved it is more appropriate to specify $C_D = 0.0025$. The actual algorithm is to set C_D to the larger of the two values given by Eq. (A.29) and 0.0025. The parameter z_0 depends on the local bottom roughness; in the absence of specific information $z_0 = 1$ cm is used as suggested by Weatherly and Martin (1978).

Open lateral boundary conditions are problematic since one must parameterize the environment exterior to the relevant domain. Two types of open boundaries exist, inflow and outflow. Temperature and salinity are prescribed from data at an inflowing boundary, whereas at outflow boundaries,

$$\frac{\partial \Theta, S}{\partial t} + u_n \frac{\partial \Theta, S}{\partial n} = 0 \tag{A.31}$$

is solved where the subscript n is the coordinate normal to the boundary. Turbulence kinetic energy and the macroscale quantity $(q^2 l)$ are calculated with sufficient accuracy at the boundaries by neglecting the advection in comparison with other terms in their respective equations.

The open lateral velocity boundary conditions in some of the applications are computed by using the available hydrographic data in conjunction with a simplified diagnostic model. This type of model uses only geostrophic plus Ekman dynamics and therefore solves a simplified form of the full equations of motion. It does not require a velocity at a reference level but only along a single transect crossing f/H contours. While the normal component of velocity is specified, a free slip condition is used for the tangential component.

In other applications including those with tidal forcing, either the elevation is prescribed as a function of time and space or a radiation condition of the form

$$\frac{\partial \eta}{\partial t} + c\frac{\partial \eta}{\partial n} = F(s,t) \tag{A.32}$$

is prescribed. Here c is the local shallow water wave speed, $(gH)^{1/2}$, and s is the tangential coordinate. The function $F(s,t)$ incorporates the necessary forcing due to tides and the mean calculation as described by Blumberg and Kantha (1985). The nonlinear terms in the momentum equations are additionally neglected at the open boundary.

A.1.4 Vertical Coordinate Representation

It has often been noted that the ordinary x, y, z coordinate system has certain disadvantages in the vicinity of large bathymetric irregularities. It is desirable to introduce a new set of independent variables that transforms both the surface and the bottom into coordinate surfaces. The governing external and internal mode equations are transformed from (x, y, z, t) to (x^*, y^*, σ, t^*) coordinates, where

$$\begin{aligned} x^* &= x \\ y^* &= y \\ \sigma &= \frac{z-\eta}{H+\eta} \\ t^* &= t \end{aligned} \tag{A.33}$$

Now let $D \equiv H + \eta$ and apply the chain rule; the following relationships linking derivatives in the old system to those in the new system are obtained:

$$\frac{\partial G}{\partial x} = \frac{\partial G}{\partial x^*} - \frac{\partial G}{\partial \sigma}\left(\frac{\sigma}{D}\frac{\partial D}{\partial x^*} + \frac{1}{D}\frac{\partial \eta}{\partial x^*}\right) \tag{A.34}$$

$$\frac{\partial G}{\partial y} = \frac{\partial G}{\partial y^*} - \frac{\partial G}{\partial \sigma}\left(\frac{\sigma}{D}\frac{\partial D}{\partial y^*} + \frac{1}{D}\frac{\partial \eta}{\partial y^*}\right) \tag{A.35}$$

$$\frac{\partial G}{\partial z} = \frac{1}{D}\frac{\partial G}{\partial \sigma} \tag{A.36}$$

$$\frac{\partial G}{\partial t} = \frac{\partial G}{\partial t^*} - \frac{\partial G}{\partial \sigma}\left(\frac{\sigma}{D}\frac{\partial D}{\partial t^*} + \frac{1}{D}\frac{\partial \eta}{\partial t^*}\right) \tag{A.37}$$

where G is an arbitrary field available, and σ ranges from $\sigma = 0$ at $z = \eta$ to $\sigma = -1$ at $z = -H$. A new vertical velocity can now be defined

$$\omega \equiv w - u\sigma\frac{\partial D}{\partial x^*} + \frac{\partial \eta}{\partial x^*} - v\sigma\frac{\partial D}{\partial y^*} + \frac{\partial \eta}{\partial y^*} - \left(\sigma\frac{\partial D}{\partial t^*} + \frac{\partial \eta}{\partial t^*}\right) \tag{A.38}$$

which transforms the boundary conditions, Eq. (A.23) and Eq. (A.27), into

$$\omega(x^*, y^*, 0, t^*) = 0 \tag{A.39}$$

$$\omega(x^*, y^*, -1, t^*) = 0 \tag{A.40}$$

Also, any vertically integrated quantity, G, for example, now appears as

$$\overline{G} = \int_{-1}^{0} G d\sigma \tag{A.41}$$

Eq. (A.1), Eq. (A.2), Eq. (A.3), Eq. (A.6), Eq. (A.7), Eq. (A.12) and Eq. (A.13) may now be rewritten as (all asterisks will be dropped for notational convenience)

$$\frac{\partial \eta}{\partial t} + \frac{\partial Du}{\partial x} + \frac{\partial Dv}{\partial y} + \frac{\partial \omega}{\partial \sigma} = 0 \tag{A.42}$$

$$\begin{aligned} \frac{\partial Du}{\partial t} \quad &+ \quad \frac{\partial Du^2}{\partial x} + \frac{\partial Duv}{\partial y} + \frac{\partial u\omega}{\partial \sigma} - fDv + gD\frac{\partial \eta}{\partial x} = \\ &- \quad \frac{\mathrm{g}D^2}{\rho_0}\int_{\sigma}^{0}\left[\frac{\partial \rho}{\partial x} - \frac{\sigma}{D}\frac{\partial D}{\partial x}\frac{\partial \rho}{\partial \sigma}\right]d\sigma + \frac{\partial}{\partial \sigma}\left[\frac{K_M}{D}\frac{\partial u}{\partial \sigma}\right] + DF_x \end{aligned} \tag{A.43}$$

$$\begin{aligned} \frac{\partial Dv}{\partial t} \quad &+ \quad \frac{\partial Dv^2}{\partial y} + \frac{\partial Duv}{\partial x} + \frac{\partial v\omega}{\partial \sigma} + fDu + gD\frac{\partial \eta}{\partial y} = \\ &- \quad \frac{\mathrm{g}D^2}{\rho_0}\int_{\sigma}^{0}\left[\frac{\partial \rho}{\partial y} - \frac{\sigma}{D}\frac{\partial D}{\partial y}\frac{\partial \rho}{\partial \sigma}\right]d\sigma + \frac{\partial}{\partial \sigma}\left[\frac{K_M}{D}\frac{\partial v}{\partial \sigma}\right] + DF_y \end{aligned} \tag{A.44}$$

$$\frac{\partial D\Theta}{\partial t} + \frac{\partial Du\Theta}{\partial x} + \frac{\partial Dv\Theta}{\partial y} + \frac{\partial \Theta\omega}{\partial \sigma} = \frac{\partial}{\partial \sigma}\left[\frac{K_H}{D}\frac{\partial \Theta}{\partial \sigma}\right] + DF_\Theta \tag{A.45}$$

$$\frac{\partial DS}{\partial t} + \frac{\partial DuS}{\partial x} + \frac{\partial DvS}{\partial y} + \frac{\partial S\omega}{\partial \sigma} = \frac{\partial}{\partial \sigma}\left[\frac{K_H}{D}\frac{\partial S}{\partial \sigma}\right] + DF_S \tag{A.46}$$

$$\begin{aligned} \frac{\partial Dq^2}{\partial t} \quad &+ \quad \frac{\partial Duq^2}{\partial x} + \frac{\partial Dvq^2}{\partial y} + \frac{\partial q^2\omega}{\partial \sigma} = \frac{\partial}{\partial \sigma}\left[\frac{K_q}{D}\frac{\partial q^2}{\partial \sigma}\right] \\ &+ \quad \frac{2K_M}{D}\left[\left(\frac{\partial u}{\partial \sigma}\right)^2 + \left(\frac{\partial v}{\partial \sigma}\right)^2\right] + \frac{2g}{\rho_0}K_H\frac{\partial \rho}{\partial \sigma} - \frac{2Dq^3}{\Lambda_l} + DF_q \end{aligned} \tag{A.47}$$

$$\begin{aligned} \frac{\partial Dq^2\ell}{\partial t} \quad &+ \quad \frac{\partial Duq^2\ell}{\partial x} + \frac{\partial Dvq^2\ell}{\partial y} + \frac{\partial q^2\omega}{\partial \sigma} = \frac{\partial}{\partial \sigma}\left[\frac{K_q}{D}\frac{\partial q^2\ell}{\partial \sigma}\right] \\ &+ \quad E_1\ell\left\{\frac{K_M}{D}\left[\left(\frac{\partial u}{\partial \sigma}\right)^2 + \left(\frac{\partial v}{\partial \sigma}\right)^2\right] + \frac{qE_3}{\rho_0}K_H\frac{\partial \rho}{\partial \sigma}\right\} - \frac{Dq^3}{B_1}\widetilde{w} + DF_\ell \end{aligned} \tag{A.48}$$

The horizontal viscosity and diffusion terms are defined according to:

$$DF_x \equiv \frac{\partial \widehat{\tau}_{xx}}{\partial x} - \frac{\partial}{\partial \sigma}\left[\left(\frac{\sigma}{D}\frac{\partial D}{\partial x}+\frac{1}{D}\frac{\partial \eta}{\partial x}\right)\widehat{\tau}_{xx}\right] + \frac{\partial}{\partial y}(\widehat{\tau}_{yx}) - \frac{\partial}{\partial \sigma}\left[\left(\frac{\sigma}{D}\frac{\partial D}{\partial y}+\frac{1}{D}\frac{\partial \eta}{\partial y}\right)\widehat{\tau}_{yx}\right] \tag{A.49}$$

$$DF_y \equiv \frac{\partial \widehat{\tau}_{yy}}{\partial y} - \frac{\partial}{\partial \sigma}\left[\left(\frac{\sigma}{D}\frac{\partial D}{\partial y}+\frac{1}{D}\frac{\partial \eta}{\partial y}\right)\widehat{\tau}_{yy}\right] + \frac{\partial}{\partial x}(\widehat{\tau}_{xy}) - \frac{\partial}{\partial \sigma}\left[\left(\frac{\sigma}{D}\frac{\partial D}{\partial x}+\frac{1}{D}\frac{\partial \eta}{\partial x}\right)\widehat{\tau}_{xy}\right] \tag{A.50}$$

with

$$\widehat{\tau}_{xx} = 2A_M\left[\frac{\partial Du}{\partial x} - \frac{\partial}{\partial \sigma}\left(\sigma\frac{\partial D}{\partial x}+\frac{\partial \eta}{\partial x}\right)u\right] \tag{A.51}$$

$$\widehat{\tau}_{xy} = \widehat{\tau}_{yx} = A_M\left[\frac{\partial Du}{\partial y} - \frac{\partial}{\partial \sigma}\left(\sigma\frac{\partial D}{\partial y}+\frac{\partial \eta}{\partial y}\right)u\right] + A_M\left[\frac{\partial Dv}{\partial x} - \frac{\partial}{\partial \sigma}\left(\sigma\frac{\partial D}{\partial x}+\frac{\partial \eta}{\partial x}\right)v\right] \tag{A.52}$$

$$\widehat{\tau}_{yy} = 2A_M\left[\frac{\partial Dv}{\partial y} - \frac{\partial}{\partial \sigma}\left(\sigma\frac{\partial D}{\partial y}+\frac{\partial \eta}{\partial y}\right)v\right] \tag{A.53}$$

Also,

$$DF_{\Theta_i} = \frac{\partial \widehat{q}_x}{\partial x} - \frac{\partial}{\partial \sigma}\left[\left(\frac{\sigma}{D}\frac{\partial D}{\partial x}+\frac{1}{D}\frac{\partial \eta}{\partial x}\right)\widehat{q}_x\right] + \frac{\partial \widehat{q}_y}{\partial y} - \frac{\partial}{\partial \sigma}\left[\left(\frac{\sigma}{D}\frac{\partial D}{\partial y}+\frac{\partial \eta}{\partial y}\right)\widehat{q}_y\right] \tag{A.54}$$

$$\widehat{q}_x = A_H\left[\frac{\partial \Theta_i D}{\partial x} - \frac{\partial}{\partial \sigma}\left(\sigma\frac{\partial D}{\partial x}+\frac{\partial \eta}{\partial x}\right)\Theta_i\right] \tag{A.55}$$

$$\widehat{q}_y = A_H\left[\frac{\partial \Theta_i D}{\partial y} - \frac{\partial}{\partial \sigma}\left(\sigma\frac{\partial D}{\partial y}+\frac{\partial \eta}{\partial y}\right)\Theta_i\right] \tag{A.56}$$

where Θ_i now represents Θ, S, q^2 and $q^2\ell$.

A.1.5 Mode splitting technique

The equations, governing the dynamics of coastal circulation, contain fast moving external gravity waves and slow moving internal gravity waves. It is desirable in terms of computer economy to separate the vertically integrated equations (external mode) from the vertical structure equations (internal mode). This technique, known as mode splitting (Simons, 1974; Madala and Piacsek, 1977) permits the calculation of the free surface elevation with little sacrifice in computational time by solving the velocity transport separately from

the three-dimensional calculation of the velocity and the thermodynamic properties. The velocity external mode equations are obtained by integrating the internal mode equations over the depth, thereby eliminating all vertical structure. Thus, by integrating Eq. (A.42) from $\sigma = -1$ to $\sigma = 0$ and using the boundary conditions Eq. (A.39) and Eq. (A.40), equation for the surface elevation can be written as

$$\frac{\partial \eta}{\partial t} + \frac{\partial D\overline{U}}{\partial x} + \frac{\partial D\overline{V}}{\partial y} \tag{A.57}$$

After integration, the momentum equations, Eq. (A.2) and Eq. (A.3) become

$$\begin{aligned} \frac{\partial (D\overline{U})}{\partial t} &+ \frac{\partial (D\overline{U^2})}{\partial x} + \frac{\partial (D\overline{UV})}{\partial y} - fD\overline{V} \\ &+ gD\frac{\partial \eta}{\partial x} - D\overline{F}_x = -\overline{wu}(0) + \overline{wu}(-1) - \frac{\partial \overline{DU^2}}{\partial x} - \frac{\partial \overline{DU'V'}}{\partial y} \\ &- \frac{gD^2}{\rho_0}\frac{\partial}{\partial x}\int_{-1}^{0}\int_{\sigma}^{0}\rho d\sigma' d\sigma - \frac{gD}{\rho_0}\frac{\partial D}{\partial x}\int_{-1}^{0}\int_{\sigma}^{0}\sigma'\frac{\partial \rho}{\partial \sigma}d\sigma' d\sigma \end{aligned} \tag{A.58}$$

$$\begin{aligned} \frac{\partial (D\overline{V})}{\partial t} &+ \frac{\partial (D\overline{UV})}{\partial x} + \frac{\partial (D\overline{V^2})}{\partial y} + fD\overline{U} \\ &+ gD\frac{\partial \eta}{\partial y} - D\overline{F}_y = -\overline{wv}(0) + \overline{wv}(-1) - \frac{\partial \overline{DU'V'}}{\partial x} - \frac{\partial \overline{DV'^2}}{\partial y} \\ &- \frac{gD^2}{\rho_0}\frac{\partial}{\partial y}\int_{-1}^{0}\int_{\sigma}^{0}\rho d\sigma' d\sigma + \frac{gD}{\rho_0}\frac{\partial D}{\partial y}\int_{-1}^{0}\int_{\sigma}^{0}\sigma'\frac{\partial \rho}{\partial \sigma'}d\sigma' d\sigma \end{aligned} \tag{A.59}$$

The overbars denote vertically integrated velocities such as

$$\overline{U} \equiv \int_{-1}^{0} U d\sigma \tag{A.60}$$

The wind stress components are $-\overline{wu}(0)$ and $-\overline{wv}(0)$, and the bottom stress components are $-\overline{wu}(-1)$ and $-\overline{wv}(-1)$. The terms in Eq. (A.58) and Eq. (A.59) involving U'^2 , $U'V'$, and V'^2 represent vertical averages of the cross-products of the velocity departures from the vertically integrated (average) velocity and are often denoted as the dispersion terms. Thus

$$\left(\overline{U'^2}, \overline{V'^2}, \overline{U'V'}\right) = \int_{-1}^{0}\left(U'^2, V'^2, U'V'\right) d\sigma \tag{A.61}$$

where $(U', V') = (U - \overline{U}, V - \overline{V})$. The quantities $\overline{F}_x$ and $\overline{F}_y$ are vertical integrals of the horizontal momentum diffusion and are defined according to

$$D\overline{F_x} = \frac{\partial}{\partial x}\left(2A_M\frac{\partial \overline{U}D}{\partial x}\right) + \frac{\partial}{\partial y}A_M\left(\frac{\partial \overline{U}D}{\partial y} + \frac{\partial \overline{V}D}{\partial x}\right) \tag{A.62}$$

$$D\overline{F_y} = \frac{\partial}{\partial y}\left(2A_M\frac{\partial \overline{V}D}{\partial y}\right) + \frac{\partial}{\partial y}A_M\left(\frac{\partial \overline{U}D}{\partial y} + \frac{\partial \overline{V}D}{\partial x}\right) \tag{A.63}$$

The computational strategy is to solve equations for the external mode, the shallow water wave equations Eq. (A.57), Eq. (A.58), and Eq. (A.59), with a short time step to resolve tidal motions. The external mode solutions are obtained with the terms on the right-hand side of Eq. (A.58) and Eq. (A.59) held fixed in time and after a large number of time steps, of the order of 100, an internal mode calculation is carried out. The external mode provides $\frac{\partial \eta}{\partial x}$ and $\frac{\partial \eta}{\partial y}$ for insertion into the internal mode equations, Eq. (A.42) through Eq. (A.48), which are then solved with a much longer time step. Once the vertical structure has been determined, the terms on the right-hand side Eq. (A.58) and Eq. (A.59) are updated and another external mode solution begins. In future simulations, the advective and diffusive terms in Eq. (A.58) and Eq. (A.59) will be supplied by the internal mode.

The external mode equations have not been subtracted from the original equations Eq. (A.42) and Eq. (A.44) to form the more conventional internal mode set. Consequently there may be a slow tendency for the vertical integral of the internal mode velocities to differ from the external mode velocities. This arises because of different truncation errors in each mode. To insure against accumulated mismatch, the vertical mean of the internal velocity is replaced at every time step by the external mode velocity.

A.2 Symphonie Model

Symphonie is a three-dimensional primitive equation, sigma-coordinate free-surface ocean model. The model is inspired by the POM model (Blumberg and Mellor, 1987), widely used by the coastal ocean modelling community. As we will see in the following, some of the algorithmic choices (notably the pressure gradient force) are however significantly distinct from POM.
The three components of the current, free surface elevation, temperature and salinity are computed on a C grid, using an energy conserving finite difference method (Marsaleix et al., 2008). A generalized vertical coordinate and a curvilinear horizontal coordinate are used. The sigma-coordinate formalism is well adapted to the conservation issue posed by the free surface, since it leads to a set of equations in which the volume variation of grid cells is naturally included.
The problem is slightly complicated by time-splitting techniques, used to limit calculus costs regarding surface gravity waves. The coupling of the external and internal modes (Blumberg and Mellor, 1987) is partly conditioned by conservation issues, since the barotropic current involved in 3D advection fluxes is deduced from a time average of the external mode solution, consistent with volume variation of grid cells over one internal time step. As the integral of the flux-divergence over the domain volume is equivalent to the surface integral of the fluxes over the boundaries, global conservation of primary variables directly concerns the boundary conditions of the model. The global tracer balance related to advection and diffusion should remain intact in case of solid boundaries, since fluxes through the coastal or the bottom boundaries should equal zero. As far as velocities are concerned, bottom friction (and eventually coastline friction in case of no-slip condition) modifies the global momentum balance. Tracer and momentum balances strongly depend on open boundary conditions. Most open boundary schemes are based on local dynamics considerations only, such as the radiation of outgoing waves or the definition of incoming variables. Nonetheless, boundary conditions can also satisfy global constraints (Shulman et al., 1998; Marsaleix et al., 2006).
The turbulence closure is achieved through a prognostic equation for the turbulent kinetic energy and a diagnostic equation for the mixing and dissipation length scales.
Moreover, a Non-Hydrostatic version of the Symphonie code is now available. A prognostic equation for the vertical momentum has been implemented resulting in the inversion of a classical Poisson equation for the non-hydrostatic component of the pressure.

A.2.1 Numerical formulation

The model grid is adjusted to the bathymetry thanks to a sigma-coordinate system leading to the following model equations:

$$\frac{\partial \widetilde{u}}{\partial t^*}+\frac{\partial \widetilde{u}u}{\partial x^*}+\frac{\partial \widetilde{v}u}{\partial y^*}+\frac{\partial \omega u}{\partial \sigma}-f\widetilde{v}=\frac{-H}{\rho_0}\frac{\partial p}{\partial x}+\frac{\partial}{\partial x^*}\widetilde{K}^x\frac{\partial u}{\partial x^*}+\frac{\partial}{\partial y^*}\widetilde{K}^y\frac{\partial u}{\partial y^*}+\frac{\partial}{\partial \sigma}\frac{\widetilde{K}^z}{H}\frac{\partial u}{\partial \sigma} \tag{A.64}$$

$$\frac{\partial \widetilde{v}}{\partial t^*}+\frac{\partial \widetilde{u}v}{\partial x^*}+\frac{\partial \widetilde{v}v}{\partial y^*}+\frac{\partial \omega v}{\partial \sigma}+f\widetilde{u}=\frac{-H}{\rho_0}\frac{\partial p}{\partial y}+\frac{\partial}{\partial x^*}\widetilde{K}^x\frac{\partial v}{\partial x^*}+\frac{\partial}{\partial y^*}\widetilde{K}^y\frac{\partial v}{\partial y^*}+\frac{\partial}{\partial \sigma}\frac{\widetilde{K}^z}{H}\frac{\partial v}{\partial \sigma} \tag{A.65}$$

where asterisks refer to the sigma-coordinate system and tildes indicate a multiplication by the scale factor $H = h + \eta$, which is the sum of the water column thickness at rest and the sea level anomaly (e.g., $\widetilde{u} = Hu$). The appearance of the asterisk for time in partial differentiation with respect to time is explained by the fact that sigma levels actually move (due to sea level anomaly variations) with respect to the absolute system of coordinates. Details on the coordinate transformation leading to the formulation of derivatives in the sigma-coordinate system can be found in Johns et al. (1983). The division of the pressure gradient by a reference density comes from the Boussinesq approximation. Hydrostatic equilibrium and the expression of the horizontal derivative in the sigma-coordinate system lead to

$$-\frac{1}{\rho_0}\frac{\partial p}{\partial x}=-g\frac{\partial \eta}{\partial x}-\frac{1}{\rho_0}\left(\frac{\partial p'}{\partial x^*}+\frac{\partial z}{\partial x^*}g\rho'\right) \tag{A.66}$$

where $p' = g\int_z^\eta \rho' dz'$ is the hydrostatic pressure anomaly associated with the density anomaly, $\rho' = \rho - \rho_0$. This formulation of the pressure gradient is characterized by the appearance of a term depending on the sea level anomaly only (first term on the right hand side of Eq. (A.66)). This is motivated by considerations on the free-surface computation that will be detailed later on. For sake of clarity, density is related to temperature and salinity through a linear equation of state. Thus, the density variations are governed by a simple advection diffusion tracer equation, linearly deduced from those for temperature and salinity, namely

$$\frac{\partial \widetilde{\rho}}{\partial t^*}+\frac{\partial \widetilde{u}\rho}{\partial x^*}+\frac{\partial \widetilde{v}\rho}{\partial y^*}+\frac{\partial \omega\rho}{\partial \sigma}=\frac{\partial}{\partial x^*}\widetilde{K}_T^x\frac{\partial \rho}{\partial x^*}+\frac{\partial}{\partial y^*}\widetilde{K}_T^y\frac{\partial \rho}{\partial y^*}+\frac{\partial}{\partial \sigma}\frac{\widetilde{K}_T^z}{H}\frac{\partial \rho}{\partial \sigma} \tag{A.67}$$

Using a linear equation of state is reasonable in a coastal context, since pressure effects on water density remain limited as long as the shallow water approximation is considered. Note also that a non-linear equation possibly destroys the energetic consistency of the pressure gradient force (Gerdes, 1993), but the limitation of this assumption should be kept in mind. The parameterization of sub-grid processes is given by diffusion terms on the right hand side of Eq. (A.67), involving mixing coefficients that can be calculated in different ways. Although (K^z, K_T^z) are generally calculated by a turbulent closure scheme representing the energy cascade toward small scales (Mellor and Yamada, 1982), the other mixing coefficients $(\widetilde{K}^x,\ \widetilde{K}^y,\ \widetilde{K}_T^x,\ \widetilde{K}_T^y)$ are usually given by more basic techniques intended to reduce numerical noise (Smagorinsky, 1993), if not simply reduced to a fixed value.

Momentum and tracer advection have the form of a flux-divergence, resulting from the combination of the primitive equations with the continuity equation. The latter is given by

$$\frac{\partial \eta}{\partial t^*}+\frac{\partial \widetilde{u}}{\partial x^*}+\frac{\partial \widetilde{v}}{\partial y^*}+\frac{\partial \omega}{\partial \sigma}=0 \tag{A.68}$$

This equation is used to compute ω, the vertical velocity in sigma coordinates (Blumberg and Mellor, 1987). We will just retain here that x vanishes at the bottom and at the sea surface, so that the depth integral of Eq. (A.68) leads to a simple relationship linking the sea level anomaly variations to the depth-averaged component of the current, $(\widehat{u},\widehat{v}) = H^{-1}\int_{-h}^{\eta}(u,v)\,dz$. This relationship reads

$$\frac{\partial \eta}{\partial t^*}+\frac{\partial \widetilde{\widehat{u}}}{\partial x^*}+\frac{\partial \widetilde{\widehat{v}}}{\partial y^*}=0 \tag{A.69}$$

with $(\widehat{\widehat{u}},\widehat{\widehat{v}}) = H(\widehat{u},\widehat{v})$. In the case of a finite difference method using a leapfrog scheme for the time-stepping procedure, Eq. (A.69) is computed first, i.e. the sea level anomaly variation term is computed from the divergence of the depth-averaged current known from the previous iteration. Then Eq. (A.68) gives ω, using the horizontal current components from the previous iteration and the sea level anomaly variation term provided by Eq. (A.69). Momentum Eq. (A.64) and Eq. (A.65) and density Eq. (A.67) are

then computed using mixing coefficient values from the previous iteration. In the case of an explicit method, the barotropic part of the pressure gradient (first term at the right hand side of Eq. (A.66)) poses a problem of numerical stability, generally leading to a separate treatment of the barotropic variable, using a time step specially suited for surface wave computation. This time step is normally much smaller than what it would be obtained if baroclinic physics was only considered. The so-called time-splitting technique, presented in Blumberg and Mellor (1987), is based on Eq. (A.69), completed with two equations for the depth-averaged current, deduced from the vertical integral of momentum, Eq. (A.64) and Eq. (A.65), i.e.

$$\frac{\partial \widetilde{\widehat{u}}}{\partial t^*} + \frac{\partial \widetilde{\widehat{u}}\widehat{u}}{\partial x^*} + \frac{\partial \widetilde{\widehat{v}}\widehat{u}}{\partial y^*} + -f\widetilde{\widehat{v}} = -gH\frac{\partial \eta}{\partial x} + \frac{\partial}{\partial x^*}\widetilde{\widehat{K}}^x\frac{\partial \widehat{u}}{\partial x^*} + \frac{\partial}{\partial y^*}\widetilde{\widehat{K}}^y\frac{\partial \widehat{u}}{\partial y^*} + \left[\frac{K^z}{H}\frac{\partial u}{\partial \sigma}\right]_{\sigma 0}^{\sigma 1} - H\int_{\sigma 0}^{\sigma 1}\left(\frac{1}{\rho_0}\frac{\partial p'}{\partial x} + \frac{\partial \widetilde{u}'u'}{\partial x^*} + \frac{\partial \widetilde{v}'u'}{\partial y^*}\right)d\sigma\frac{\partial}{\partial \sigma}\frac{\widetilde{K}^z}{H}\frac{\partial u}{\partial \sigma} \tag{A.70}$$

$$\frac{\partial \widetilde{\widehat{v}}}{\partial t^*} + \frac{\partial \widetilde{\widehat{u}}\widehat{v}}{\partial x^*} + \frac{\partial \widetilde{\widehat{v}}\widehat{v}}{\partial y^*} + +f\widetilde{\widehat{u}} = -gH\frac{\partial \eta}{\partial y} + \frac{\partial}{\partial x^*}\widetilde{\widehat{K}}^x\frac{\partial \widehat{v}}{\partial x^*} + \frac{\partial}{\partial y^*}\widetilde{\widehat{K}}^y\frac{\partial \widehat{v}}{\partial y^*} + \left[\frac{K^z}{H}\frac{\partial v}{\partial \sigma}\right]_{\sigma 0}^{\sigma 1} - H\int_{\sigma 0}^{\sigma 1}\left(\frac{1}{\rho_0}\frac{\partial p'}{\partial y} + \frac{\partial \widetilde{u}'v'}{\partial x^*} + \frac{\partial \widetilde{v}'v'}{\partial y^*}\right)d\sigma\frac{\partial}{\partial \sigma}\frac{\widetilde{K}^z}{H}\frac{\partial u}{\partial \sigma} \tag{A.71}$$

where (σ_0, σ_1) are the bottom and surface values of σ.

Symphonie model uses the sigma-coordinate transformation of Johns and Oguz (1987) with $(\sigma_0, \sigma_1) = (0, 1)$. Note however that this is just a special case of the more general terrain following coordinate transformation. Besides the numerical aspects can virtually be transposed to a wide range of coordinate transformations, like for instance the hybrid terrain pressure coordinate system often used in atmospheric models (see for instance Arakawa and Suarez, 1983). Note that $(\widehat{K}^x, \widehat{K}^y)$ correspond to the depth-averaged values of Eq. (A.69) - Eq. (A.71) (hereafter external mode equations) are used to compute $(\eta,\ \widehat{u}, \widehat{v})$ with a small time step. The terms under the integral at the right hand side of Eq. (A.70) and Eq. (A.71) are frozen over a time period equivalent to one time step of the so-called internal mode equations. The latter consist of momentum Eq. (A.64) and Eq. (A.65), and tracer Eq. (A.67). The time-splitting technique works in the following manner: at the beginning of each iteration, a baroclinic current, (u', v'), is obtained by removing the depth-averaged value from the absolute current provided by the internal mode solution. This baroclinic current and the three-dimensional pressure anomaly, p', provide the last term at the right hand side of Eq. (A.70) and Eq. (A.71). The latter and Eq. (A.69) are then integrated over one external mode sequence with a small time step. At the end of the external mode sequence, the depth-averaged component of the absolute current is updated using a time-averaged value of the external mode solution. Three-dimensional equations, e.g. continuity Eq. (A.68), momentum Eq. (A.64) and Eq. (A.65) and tracer equation are then computed. Note that Eq. (A.64) and Eq. (A.65) can actually be viewed as a pair of equations for the baroclinic components of the current $(u',\ v') = (u - \widehat{u}, v - \widehat{v})$.

A.3 Lagrangian Assessment for Marine Pollution

LAMP3D (Lagrangian Assessment for Marine Pollution 3 Dimensional Model) is a single-particle lagrangian model (Doglioli, 2000): at each time step, Δt, a particle moves from its position $\boldsymbol{r} = (x, y, z)$ with a velocity $\mathbf{v}(\boldsymbol{r}(t), t)$ causing a displacement, which determines the new position of a particle in a time interval $\Delta t = t_2 - t_1$

$$\mathbf{r}(t_1 + \Delta t) = \mathbf{r}(t_1) + \int_{t_1}^{t_1+\Delta t}\mathbf{v}\Big(\mathbf{r}(t), t\Big)\,dt$$

The total velocity $\mathbf{v}(\boldsymbol{r}(t), t)$ is formed by $\mathbf{U}(\boldsymbol{r}(t), t)$ and $\mathbf{v}'$ (Zannetti, 1990),

$$\mathbf{v} = \mathbf{U} + \mathbf{v}'$$

where $\mathbf{U}$ is the calculated flow field, representing the transport process due to the mean flow field, while $\mathbf{v}'$ is a stochastic fluctuation, which is related to the turbulence and small scale eddies.

The time and space scales of the dispersion processes allow to use a simple "random walk model" (Allen, 1982):

$$\mathbf{r}_{n+1} - \mathbf{r}_n = \mathbf{U}_n \Delta t + \boldsymbol{\varrho}_n$$

To assign a value to $\boldsymbol{\varrho} = (\varrho_x, \varrho_y, \varrho_z)$ the LAMP3D algorithm uses the FORTRAN generator of pseudorandom numbers with uniform distribution in the interval $[0, 1]$ to obtain a normal probability density function with zero mean and given standard deviation $\boldsymbol{\sigma} = (\sigma_x, \sigma_y, \sigma_z)$.

Thus, for a cloud of Q diffusing particles released in the absence of velocity from a single point $P(0, 0, 0)$ at time $t = 0$, their space distribution at some time later $t = n\Delta t$ is

$$C(\mathbf{r}, n) = \frac{Q}{\left(2\pi n \boldsymbol{\sigma}^2\right)^{3/2}} \left(e^{-\frac{\mathbf{r}^2}{2n\sigma^2}}\right) \tag{A.72}$$

This is identical to the point source Gaussian solution

$$G(\boldsymbol{r}, t) = \frac{1}{(4\pi\kappa_q t)^{3/2}} \left(e^{-\frac{\mathbf{r}^2}{(4\kappa_q t)}}\right) \tag{A.73}$$

for the standard diffusion equation for the property q

$$\frac{\partial q}{\partial t} = \kappa_q \, \partial^2 q$$

where κ_q is the diffusion coefficient, measured in $\mathrm{m^2 s^{-1}}$.

The model input parameter $\boldsymbol{\sigma}$ is given by

$$\boldsymbol{\sigma} = \sqrt{2\kappa_q \Delta t}$$

in meters. A comparison between the 'K-theory' κ_q coefficient and experimental data given by Bacciola et al. (1993) allows a suitable choice of the value $\boldsymbol{\sigma} = 3.46$ m.

LAMP3D uses a constant standard deviation value on the horizontal grid $\sigma_{i,j} = \sigma_x = \sigma_y$ which decreases, as the intensity of turbulent processes, with the depth:

$$\sigma_{i,j}(z_n) = \sigma_{i,j}(0) \left(1 + \frac{z_n}{H_{i,j}}\right)$$

where z_n is the vertical coordinate of the particle and $H_{i,j}$ is the local bathymetry value.

Specific properties can be assigned to each single particle. Different typology of particle can be considered: dissolved or particulate matter. For the latter, (i) conservative, (ii) decaying and (iii) settling particles can be considered.

i) Conservative particle number is constant for the whole duration of the simulation, except if particles cross the open boundaries or if there is a source in the domain.

ii) An exponential decay is applied to decaying particles:

$$c = c_0 \cdot 10^{-\frac{\mathrm{t}}{\mathrm{T_{90}}}}$$

where $\mathrm{T_{90}}$ is the time required to degrade 90% of the biodegradable matter in a given environment (Vismara, 1992).

iii) A sedimentation velocity $\boldsymbol{w}_{sed} = (0, 0, w_{sed})$ is added to deterministic velocity $\mathbf{U}$ of settling particles.

At the end of each suitably chosen time interval the concentration field $C_{i,j,k}$ is computed by simply counting the number of particles found within each grid cell.

A.3.1 The POM-LAMP3D coupled model

In order to simulate the 3D dispersion of pollutant, the LAMP3D transport model is coupled to the POM model. The 2D scheme (POM2D) is used. A suitable, although approximate, method is then used to build a 3D flow field.

As already seen in section A.1.5, POM2D solves the equation of the free surface elevation and the momentum equations integrated from bottom ($\sigma = -1$) to surface ($\sigma = 0$) and provides the horizontal vertically averaged velocity component

$$\overline{U} = \int_{-1}^{0} U \mathrm{d}\sigma \qquad \overline{V} = \int_{-1}^{0} V \mathrm{d}\sigma$$

The LAMP3D model calculates the 3D velocity field $\mathbf{U}_{i,j,k} = (u_{i,j,k}, v_{i,j,k}, w_{i,j,k})$ using mass conservation and theoretical vertical velocity profiles (Doglioli, 2000). The vertical profile based on the Ekman spiral model is used. Even if the Ekman spiral profile details have been very rarely measured, the effects of the transport integral on the water column has been frequently observed both in deep and in coastal waters. In this way, using the mean horizontal velocity vector provided by POM2D ($\mathbf{v}_{i,j}^{\mathrm{POM2D}}$) the horizontal velocity $\mathbf{v}_{i,j,k}^{\mathrm{H}} = (u_{i,j,k}, v_{i,j,k})$ at a given depth $k\Delta z$ can be calculated by the formula

$$\mathbf{v}_{i,j,k}^{\mathrm{H}} = \mathbf{v}_{i,j}^{\mathrm{POM2D}} \, \kappa H_{i,j} \, \frac{e^{\kappa(\mathrm{H}+\mathrm{k})} - e^{-\kappa(\mathrm{H}+\mathrm{k})}}{\left(e^{\frac{\kappa \mathrm{H}}{2}} - e^{\frac{-\kappa \mathrm{H}}{2}}\right)^2}$$

where

$$\kappa = (1+\imath)\frac{\pi}{\left(\frac{\delta_E}{\Delta Z}\right)}$$

is a complex ($\imath$ is the imaginary unit) function of Ekman depth $\delta_E = 150$ m.

The code imposes the mass conservation in each grid cell and calculates a 3D field for the vertical component of the velocity:

$$w_{i,j,k} = w_{i,j,k+1} + \Delta Z \left(\mathrm{Re}\left\{ \frac{\mathbf{v}_{i+1,j,k}^{\mathrm{POM2D}} - \mathbf{v}_{i-1,j,k}^{\mathrm{POM2D}}}{2\Delta X} \right\} + \mathrm{Im}\left\{ \frac{\mathbf{v}_{i,j+1,k}^{\mathrm{POM2D}} - \mathbf{v}_{i,j-1,k}^{\mathrm{POM2D}}}{2\Delta Y} \right\} \right)$$

The deterministic velocity of each diffusing particle is determined through a weighted interpolation of velocity at the eight nearest neighbouring grid points.

A.4 BOlogna Limited Area Model

BOLAM (BOlogna Limited Area Model) has been developed at the Institute of Sciences of Atmosphere and Climate (ISAC) of the National Research Council (CNR) of Bologna, Italy (Buzzi et al., 1994; Buzzi and Malguzzi, 1997). It is used operationally for weather forecasting at the Meteo - Hydrological Center for Civil Protection (CFMI-PC) of the Ligurian Region and at the Oceanic and Atmospheric Physics Group at the Department of Physics (DIFI) of the University of Genoa.

BOLAM is a grid-point hydrostatic meteorological model in sigma coordinates, with variable spacing in the vertical such as to give higher resolution near the surface and, to a smaller extent, near the tropopause.

The vertical discretization is of the Lorenz type, with vertical velocity defined at intermediate levels between those where the prognostic variables are known. Upper and lower boundary conditions of vanishing vertical velocity are applied at $\sigma = 0$ and $\sigma = 1$.

Horizontal discretization for the enstrophy and energy conserving second order advection scheme is performed on an Arakawa C-grid (Mesinger and Arakawa, 1976; Haltiner and Williams, 1980), with latitude (φ) and longitude (λ) as independent variables.

The prognostic variables are: zonal (u) and meridional (v) wind components, potential temperature (θ), specific humidity (q), and surface pressure (p_s). The use of θ as thermodynamic prognostic variable instead of virtual temperature T_v makes it possible to simplify the thermodynamic equation at the expense of the

introduction of small errors mostly related to the neglect of the dependence of gas constant and specific heat on the mixing ratio of water substance in the definition of potential temperature.

A fourth-order horizontal diffusion term, based on the ∇^4 spatial operator, is added to all prognostic equations except in the tendency of p_s. Horizontal diffusion can introduce significant errors when σ surfaces become rough over complex terrain; in this respect, the use of θ instead of temperature is advantageous and avoids the need for a spatially dependent diffusion coefficient. Sensitivity tests have indicated reduction of numerical noise over steep orography in the present version of the model compared with a previous one which used T_v as prognostic variable. A second-order horizontal diffusion is applied to the divergence of horizontal velocity, to reduce gravity wave amplitude and to limit somehow the development of explicit convection. The advection equation is solved using the forward-backward advection scheme (FBAS) implemented by Malguzzi and Tartaglione (1999). FBAS is equivalent to applying a leapfrog scheme twice with half the time step. Thus, using FBAS it is possible to save half the computer time needed to compute advection.

The lateral boundary conditions are imposed using a relaxation scheme of the Davies-Lehmann type (Davies, 1976; Lehmann, 1993) that minimizes wave energy reflection.

The physical package includes vertical diffusion, dry adiabatic adjustment, soil water and energy balance, radiation, large-scale precipitation and evaporation, and parameterisation of moist convection.

Vertical diffusion, confined to the lower part of the troposphere, is a parameterisation of turbulent mixing of momentum, potential temperature and specific humidity. The scheme is based on a mixing-length hypothesis, with exchange coefficients depending on the Richardson number, as in Louis et al. (1982).

Bottom boundary fluxes of the above quantities are a linear function of the wind speed at the lowest sigma level and of the vertical gradient of the quantity in the layer between the lowest sigma level and the ground. The constant of proportionality depends on the Richardson number in such layer above the ground and on surface roughness. The roughness length is fixed over land (in the present version it is prescribed as a simple function of topography elevation), and it is computed with the Charnock (1955) formula, which depends on surface wind, over water. On flat land, in particular, the roughness length only parameterises the dynamic effects of the airflow around the roughness elements of the terrain, like trees, buildings and so on, and assumes values within an upper limit equal to about 1 m. In areas with more complex topography, the z_0 parameter also includes the effects of wind friction with the ground associated with that part of the orography spectrum that is not explicitly represented in the model orography and assumes values up to about 10 m. To avoid possible numerical instabilities, an implicit time scheme has been implemented in which the surface fluxes and the Richardson number are computed at the oldest time level. A parameterization of dry convective adjustment enhances vertical mixing of potential temperature by slowly relaxing toward a neutral condition if the lapse rate becomes super-adiabatic.

The model computes a surface energy and water balance. The soil is divided into three layers: temperature and wetness are predicated in the two uppermost layers and are kept constant in the deepest bottom layer. In addition, snow depth is predicated over land, depending on accumulation, melting and sublimation. Albedo is prescribed and may change in time only as a function of snow cover. Surface temperature over water is kept constant in time and equal to the climatological value. Sea ice treatment is also included.

The radiation scheme consists in a simplified version of the scheme described in Geleyn and Hollingsworth (1979), with optical properties computed as explained in Ritter and Geleyn (1992). Clouds, that are computed as a function of the local relative humidity, interact with radiation (Geleyn, 1981). Total cloud cover at any level depends on the cloud distribution in the above column of air, assuming a certain degree of correlation between clouds at adjacent levels. The water cycle is based on six explicit prognostic variables: specific humidity, cloud ice, cloud water, rain, snow, graupel.

A semi-Lagrangian scheme for 3-D advection and fall of hydrometeors is applied. The most important microphysical processes (see Buzzi and Malguzzi, 1997) are parameterized as functions of local thermodynamic variables and concentration of condensate, with a simplified approach similar in several aspects to that proposed by Schultz (1995). The parameterization of moist convection is attained using the method devised by Kain and Fritsch (1992). In order to allow for convection rooted at some level above the ground (e.g. in cases of low level inversions), the check for unstable conditions is carried out for a number of levels above the surface. In cases of elevated convection, the precipitation at the base of the convective layer is treated as in the large-scale precipitation routine (e.g. evaporation is considered explicitly).

As far as geographical and climatological information are concerned, the topography is obtained by interpolation of the U.S. Navy $1/6$th degree topography on the model grid, while SST, initial soil wetness and

deep soil parameters are computed by interpolation in space and time from climatological monthly data.

B

Appendix B - Numerical code of the FOAM model

B.1 FOAM code

```
1
2
3  !                     SOFTWARE LICENSING
4  !    This program is free software; you can redistribute it and or modify it under ↩
       the terms of the GNU General
5  Public License (GPL) as published by the Free Software Foundation, either Version 2 ↩
       of the license, or (at your
6  option) any later version.
7  !    This program is distributed  in the hope that  it  will be useful, but without ↩
       any warranty; without even the
8  implied warranty of merchantability or fitness for a particular purpose.
9  !    See  the GPL  for more details.
10 !    A copy of the GNU General Public License is available at http://www.gnu.org/↩
       copyleft/gpl.html
11
12       Program FOAM
13
14       PARAMETER (IMLAMP=20,JMLAMP=20,IMF=160,JMF=160)
15       CHARACTER*15 dataini
16       character*3  recNUMsim,recNUMsim2
17       character*8  fileIN
18       character*8  fileOUT
19       REAL    Vbot [allocatable](:,:)
20       REAL    Vb   [allocatable](:,:)
21       REAL    FLUXB[allocatable](:,:)
22       REAL    O2sup[allocatable](:,:)
23       REAL    O2dem[allocatable](:,:)
24       REAL    rI   [allocatable](:,:)
25       REAL    CONCB[allocatable](:,:)
26       DATA SMALL/1.e-09/,UNDEF/-9999.9/
27
28       include 'param_foam.fi'
29
30       write(*,*) 'simulation number'
31       read(*,*) recNUMsim
```

```
32
33        write(*,*) 'restart?1=yes'
34        read(*,*) restart
35         if (restart.eq.1) then
36          write(*,*) 'restart simulation number'
37          read(*,*) recNUMsim2
38         endif
39
40        write(*,*) 'CONCBcrit'
41        read(*,*) CONCBcrit
42
43          IEND=(IEND/72)*72
44          I2ORE=72
45
46        deltaXF=(deltaXLAMP/IMF)*IMLAMP
47        deltaYF=(deltaYLAMP/JMF)*JMLAMP
48        rIOLAkm=IOLAMP*deltaXLAMP/1000
49        rJOLAkm=JOLAMP*deltaYLAMP/1000
50        delkmXF=deltaXF/1000
51        delkmYF=deltaYF/1000
52
53
54        ALLOCATE(Vbot (IMLAMP,JMLAMP))
55        ALLOCATE(Vb   (IMF,JMF))
56        ALLOCATE(FLUXB(IMF,JMF))
57        ALLOCATE(O2sup(IMF,JMF))
58        ALLOCATE(O2dem(IMF,JMF))
59        ALLOCATE(rI   (IMF,JMF))
60        ALLOCATE(CONCB(IMF,JMF))
61
62        AREA=0
63        do j=1,JMF
64         do i=1,IMF
65          FLUXB(i,j)=0
66          O2sup(i,j)=0
67          O2dem(i,j)=0
68         enddo
69        enddo
70
71
72  !-----INPUT file
73        open(11,file='../POM_DATA/foam'//recNUMsim//'.txt'
74       &       ,status='old')
75
76  !-----OUTPUT file
77
78  !=>binary input for GRADS
79        open(99,file='../POM_GRADS/foam_rest_'//recNUMsim//'.bin'
80       &       ,form='unformatted',recordType='stream',status='new')
81
82  !=>ascii IMPACTED AREA
83        open(97,file='../POM_GRADS/AREA_rest_'//recNUMsim//'.txt'
84       &       ,status='new')
85
86  !=>ascii BARYCENTER
87        open(96,file='../POM_GRADS/BAR_rest_'//recNUMsim//'.txt'
88       &       ,status='new')
89
90  !=>ascii final CONCB
```

```
91        open(90,file='../POM_GRADS/CONCB_rest_'//recNUMsim//'.txt'
92       &       ,status='new')
93
94  !=>ascii CONCB
95        open(79,file='../POM_GRADS/CONCB_bar_'//recNUMsim//'.txt'
96       &       ,status='new')
97
98  !=>ascii rI
99        open(78,file='../POM_GRADS/rI_bar_'//recNUMsim//'.txt'
100      &       ,status='new')
101 !=>ascii FLUXB
102       open(77,file='../POM_GRADS/FLUXB_bar_'//recNUMsim//'.txt'
103      &       ,status='new')
104
105
106 !RESTART
107
108       if (restart.eq.1) then
109         open(10,file='../POM_GRADS/CONCB_rest_'//recNUMsim2//'.txt'
110      &       ,status='old')
111
112         do i=1,IMF
113          do j=1,JMF
114           read(10,'(24X,D12.4)') CONCB(i,j)
115          enddo
116         enddo
117
118       else
119        do i=1,IMF
120          do j=1,JMF
121           CONCB(i,j)=0
122          enddo
123         enddo
124       endif
125
126
127       do it=1,IEND,I2ORE
128
129        read(11,'(6X,I12)') IINT
130        write(*,*) 'IINT',IINT
131        read(11,*)
132        read(11,*)
133        do
134         read(11,'(I12,2F12.4)',err=99999) Ip,Xpart,Ypart
135          Ixx=INT(Xpart/deltaXF)
136          Iyy=INT(Ypart/deltaYF)
137          FLUXB(Ixx,Iyy)=FLUXB(Ixx,Iyy)+1
138        enddo
139 99999  continue
140        read(11,*)
141        do i=1,IMLAMP
142         do j=1,JMLAMP
143          read(11,'(24X,F12.4)') Vbot(i,j)
144         enddo
145        enddo
146
147       do i=1,IMF
148        do j=1,JMF
149         if(IMLAMP.ne.IMF.and.JMLAMP.ne.JMF)then
```

```
150           iLAMP=INT(i*IMLAMP/(IMF+0.0001))+1
151           jLAMP=INT(j*JMLAMP/(JMF+0.0001))+1
152          else
153           iLAMP=i
154           jLAMP=j
155          endif
156
157 !-----bottom velocity and oxygen supply
158
159          if(iLAMP.lt.IMLAMP.and.jLAMP.lt.JMLAMP)then
160           Vb(i,j)=0.25*(Vbot(iLAMP,jLAMP)+Vbot(iLAMP+1,jLAMP+1)
161      &                 +Vbot(iLAMP,jLAMP+1)+Vbot(iLAMP+1,jLAMP))
162          else
163           Vb(i,j)=Vbot(iLAMP,JLAMP)
164          endif
165
166          O2sup(i,j) = 736.3 + 672.5*LOG10(Vb(i,j)+SMALL)
167
168          if(O2sup(i,j).le.0.0) then
169            O2sup(i,j)=SMALL
170          endif
171
172 !-----flux toward the bottom and oxygen demand
173
174          FLUXB(i,j)=FLUXB(i,j)/(deltaXF*deltaYF) ![part/m2]
175          FLUXB(i,j)=FLUXB(i,j)*12*weight         ![mmolC/m2/day]
176
177 !         O2dem(i,j) = 1.07*FLUXB(i,j) - 32.6      !Atlantic parameters
178
179         O2dem(i,j) = 2.405*FLUXB(i,j) - 42.254   !Mediterranean parameters
180
181          if(O2dem(i,j).le.0.0) then
182           O2dem(i,j)=SMALL
183          endif
184
185 !-----Index of impact
186
187          rI(i,j)= O2sup(i,j)/O2dem(i,j)
188
189          if(O2sup(i,j).eq.SMALL.and.O2dem(i,j).eq.SMALL) then
190             rI(i,j)=1+2*DeltaFW
191          endif
192
193         enddo
194        enddo
195
196 !-----net flux
197
198        do j=1,JMF
199         do i=1,IMF
200          if(rI(i,j).lt.(1-DeltaFW)) then
201           FLUXB(i,j) = FLUXB(i,j)-r_iper
202          endif
203          if(rI(i,j).gt.(1+DeltaFW)) then
204           FLUXB(i,j) = FLUXB(i,j)-r_olig
205          endif
206          if((rI(i,j).ge.(1-DeltaFW)).and.(rI(i,j).le.(1+DeltaFW)) ) then
207           FLUXB(i,j) = FLUXB(i,j)-r_meso
208          endif
```

```
209         enddo
210        enddo
211
212 !-----bottom concentration
213
214        AREA=0
215        do j=1,JMF
216         do i=1,JMF
217          CONCB(i,j)=CONCB(i,j)+FLUXB(i,j)/12  ![mmolC/m2]
218           if(CONCB(i,j).lt.0) then
219             CONCB(i,j)=0.
220           endif
221
222 !-----impacted area
223
224           if (CONCB(i,j) .gt. CONCBcrit) then
225            AREA=AREA+deltaXF*deltaYF            ![m^2]
226           endif
227         enddo
228        enddo
229        write(97,*) IT,AREA
230
231 !-----barycenter
232
233         partx=0
234         party=0
235         partot=0
236         xbar=0
237         ybar=0
238         do i=1,IMF
239            do j=1,JMF
240               if (CONCB(i,j) .gt. CONCBcrit) then
241                 partx=partx+CONCB(i,j)*i
242                 party=party+CONCB(i,j)*j
243                 partot=partot+CONCB(i,j)
244               endif
245            enddo
246         enddo
247         if(partot.eq.0) then
248          xbar=0
249          ybar=0
250         else
251          xbar=partx/partot*deltaXF            ![m]
252          ybar=party/partot*deltaYF            ![m]
253         endif
254          write(96,*) IT,xbar,ybar
255
256 !-----rI and CONCB
257
258          ibar=xbar/deltaXF
259          jbar=ybar/deltaYF
260          if(ibar .gt. 0 .and. jbar .gt. 0) then
261           write(77,*) IT,FLUXB(ibar,jbar)
262           write(78,*) IT,rI(ibar,jbar)
263           write(79,*) IT,CONCB(ibar,jbar)
264          else
265           write(77,*) IT,' NaN'
266           write(78,*) IT,' NaN'
267           write(79,*) IT,' NaN'
```

```
268         endif
269
270 !****************** file BIN for GrADS *********************
271
272       do j=JMF,1,-1
273        do i=1,IMF
274          write(99) Vb(i,j)
275        enddo
276       enddo
277       do j=JMF,1,-1
278        do i=1,IMF
279          write(99) rI(i,j)
280        enddo
281       enddo
282       do j=JMF,1,-1
283        do i=1,IMF
284          write(99) FLUXB(i,j)
285        enddo
286       enddo
287       do j=JMF,1,-1
288        do i=1,IMF
289         write(99) CONCB(i,j)
290        enddo
291       enddo
292
293         do j=1,JMF
294          do i=1,IMF
295           FLUXB(i,j)=0
296          enddo
297         enddo
298
299       enddo !it
300
301          do i=1,IMF
302           do j=1,JMF
303            write(90,'(24X,D12.4)') CONCB(i,j)
304           enddo
305          enddo
306
307        close(99)
308        close(97)
309        close(96)
310        close(90)
311        close(79)
312        close(78)
313        close(77)
314
315        close(11)
316        close(10)
317
318 !-----output file => ascii input for GRADS
319
320        open(98,file='../POM_GRADS/foam_rest_'//recNUMsim//'.ctl'
321       &       ,status='new')
322
323 11109  format(A6,F8.2)
324 11110  format(50A)
325 11111  format(1A,'DEF ',I3,' LINEAR ',A4,A8)
326 11112  format(1A,'DEF ',I4,' LINEAR ',A15,I15,'mn')
```

```
327
328 11113  format(1A,'DEF ',I3,' LINEAR ',F12.5,F12.5)
329
330 11114  format(A5,I3,37A)
331 11115  format(1A,'DEF ',I3,' LEVELS ',12I6)
332
333
334       write(98,11110)'DSET ./foam_rest_'//recNUMsim//'.bin'
335
336       write(98,11110)'TITLE ------- SIMULATION NUMBER '//recNUMsim//' -------'
337       write(98,11109)'UNDEF ',undef
338       write(98,11110)'OPTIONS yrev'
339
340       mnPRTD1=120          !NINT(PRTD1*24*60)
341       itMAX=IEND/I2ORE
342       scala=1.*IMLAMP/IMF
343       write(98,11113) 'X',IMF,rIOLAkm,delkmXF
344       write(98,11113) 'Y',JMF,rJOLAkm,delkmYF
345       write(98,11110) 'ZDEF 1 levels 1'
346
347       write(98,11112) 'T',iTMAX,dataini,mnPRTD1
348
349       write(98,11110) 'VARS 4'
350       write(98,11110) 'VB     0  99 [cm/s]'
351       write(98,11110) 'rI     0  99 [adim]'
352       write(98,11110) 'FLUXB  0  99 net flux [mmol/m2/d]'
353       write(98,11110) 'CONCB  0  99 bottom concentration [mmol/m2]'
354       write(98,11110) 'ENDVARS'
355
356       write(98,*)
357       write(98,11110) 'FOAM parameters'
358       write(98,*) ' deltaFW',                    DeltaFW
359       write(98,*) ' r_oligo [mmol/m2/day]',      r_olig
360       write(98,*) ' r_iper [mmol/m2/day]',       r_iper
361       write(98,*) ' r_meso [mmol/m2/day]',       r_meso
362       write(98,*) ' particle weight [mol]',      weight
363
364       close(98)
365
366       STOP
367       END
```

Bibliography

Albérola, C., Millot, C., Font, J., 1995. On the seasonal and mesoscale variabilities of the Northern Current during the PRIMO-0 experiment in the western Mediterranean Sea. Oceanologica Acta 18(2), 163–192.

Aliani, S., Griffa, A., Molcard, A., 2003. Floating debris in the Ligurian Sea, North-Western Mediterranean. Mar. Poll. Bull. 46, 1142–1149.

Allen, C., 1982. Numerical simulation of contaminant dispersion in estuarine flow. Proc. R. Soc. Lond. A 381, 179–194.

Anderson, L., Hall, P., Iverfeldt, A., Van Der Loeff, M., Sundby, B., Westerlund, S., 1986. Benthic respiration measured by total carbonate production. Limnology and Oceanography 31, 319–329.

Arakawa, A., Suarez, M., 1983. Vertical differencing of the primitive equations in sigma coordinates. Monthly Weather Review 111, 34–45.

Astraldi, M., Gasparini, G., 1986. La circolazione costiera nel mar ligure orientale. Boll. Mus. Ist. Biol. Univ. Genova 52 suppl, 317–331.

Astraldi, M., Gasparini, G., 1992. The seasonal characteristics of the circulation in the north Mediterranean Basin and their relationship with the atmospheric-climatic condition. J. Geophys. Res. 97(C6), 9531–9540.

Astraldi, M., Gasparini, G., Manzella, G., 1990. Temporal variability of currents in the Eastern Ligurian Sea. J. Geophys. Res. 95(C2), 1515–1522.

Astraldi, M., Gasparini, G., Sparnocchia, S., 1994. The Seasonal and Interannual Variability in the Ligurian-Provencal Basin. In: La Violette, P.E. (Ed.), Seasonal and interannual variability of the Western Mediterranean Sea, Coastal and Estuarine Studies 46, 93–113.

Astraldi, M., Manzella, G., 1983. Some observations on current measurements on the East Ligurian Shelf, Mediterranean Sea. Cont. Shelf Res. 2, 183–193.

Azzaydi, M., Madrid, J., Zamora, S., Snchez-Vzquez, F., Martnez, F., 1998. Effect of three feeding strategies (automatic, ad libitum demand-feeding and time-restricted demand-feeding) on feeding rhythms and growth in European sea bass (*Dicentrarchus labrax*, L.). Aquaculture 163, 285–296.

Bacciola, D., Borghini, M., Degl'Innocenti, F., Galli, C., Lazzoni, E., Meloni, R., Sparnocchia, S., Cannarsa, S., Di Fesca, V., Manzella, G. M. R., Marri, P., Raso, G., 1993. Esperimenti per la determinazione del coefficiente di diffusione locale. Tech. rep., ENEA, RTI/AMB/GEM-MAR/93/07.

Baldi, A., Marri, P., Schirone, A., 1997. Applicazione di un modello per la simulazione del trasporto e della diluizione di inquinanti nelle acque costiere. Tech. rep., ENEA, RTI/AMB/GEM-MAR/97/04/RL2/A1.4.

Bartoli, M., Nizzoli, D., Naldi, M., Vezzulli, L., Porrello, S., Lenzi, M., Viaroli, P., 2005. Inorganic nitrogen control in wastewater treatment ponds from a fish farm (Orbetello, Italy): denitrification versus Ulva uptake. Marine Pollution Bulletin 50, 1386–1397.

Bastos, A., Collins, M., Kenyon, N., 2003. Water and sediment movement around a coastal headland: Portland Bill, Southern UK. Ocean Dynamics 53 (C3), 309–321.

Bastos, A., Kenyon, N., Collins, M., 2002. Sedimentry processes, bedforms and facies, associtated with a coastal headland: Portland Bill, Southern UK. Mar. Geol. 187, 235–258.

Basurco, B., Lovatelli, A., 2003. The aquaculture situation in the Mediterranean Sea predictions for the future. Ocean docs: http://hdl.handle.net/1834/543.

Becker, G., Pauly, M., 1996. Sea surface temperature changes in the North Sea and their causes. ICES Journal of Marine Science 53, 887–898.

Bennett, A., Kloeden, P., 1978. Boundary conditions for limited-area forecasts. J. Atmos. Sci. 35, 990–996.

Beveridge, M., Phillips, M., Clarke, R., 1991. A quantitative and qualitative assessment of wastes from aquatic animal production. In: Brune, D. E., Tomasso, J. R. (Eds.), Advances in World Aquaculture Volume 3. World Aquaculture Society, Baton-Rouge, USA, pp. 506–533.

Blumberg, A., Mellor, G., 1987. A description of a three-dimensional coastal ocean circulation model. In: Heaps, N. (Ed.), Three-Dimensional Coastal Ocean Models. Vol. 4. American Geophysical Union, Washington, D.C., p. 208.

Blumberg, A. F., Kantha, L. H., 1985. Open boundary condition for circulation models. J. of Hydra. Eng. 111,2, 237–255.

Blumberg, A. F., Signell, R., Jenter, H., 1993. Modeling transport processes in the coastal ocean. J. Marine Env. Engg. 1, 31–52.

Boucher, G., Clavier, J., Garrigue, C., 1994. Oxygen and carbon dioxide fluxes at the water-sediment interface of a tropical lagoon. Marine Ecology Progress Series 107, 185–193.

Boyer, D., Tao, L., 1987. On the motion of linearly stratified rotating fluids past capes. J. Fluid Mech. 180, 429–449.

Bruschi, A., Manzella, G., 1980. Wind and current autumnal data series analysis on the Ligurian continental shelf. Il Nuovo Cimento C 3(2), 151–164.

Bryan, K., 1969. A numerical method for the study of the world ocean. Journal of Computational Physics 4, 347–376.

Bunker, A., 1972. Wintertime interactions of the atmosphere with the Mediterranean Sea. J. Phys. Oceanogr 2, 225–238.

Burlando, M., 2008. The synoptic-scale surface wind climate regimes of the Mediterranean Sea according to the cluster analysis of ERA-40 wind fields. Theor. Appl. Climatol. 96, 69–83.

Burlando, M., Antonelli, M., Ratto, C., 2008. Mesoscale wind climate analysis: identification of anemological regions and wind regimes. Int. J. Climatol. 28(5), 629–641.

Buzzi, A., Fantini, M., Malguzzi, P., Nerozzi, F., 1994. Validation of a limited area model in cases of Mediterranean cyclogenesis: surface fields and precipitation scores. Meteorol. Atmos. Phys. 53, 137–153.

Buzzi, A., Malguzzi, P., 1997. The BOLAM III model: recent improvements and results. MAP Newsletter 7, 98–99.

Buzzi, A., Tartaglione, N., Malguzzi, P., 1998. Numerical simulations of the 1994 Piedmont flood: role of orography and moist processes. Mon. Wea. Rev. 126(9), 2369–2383.

Campins, J., Genovès, A., Jansà, A., Guijarro, J., Ramis, C., 2000. A catalogue and a classification of surface cyclones for the Western Mediterranean. Int. J. Climatol. 20, 969–984.

Campins, J., Jansà, A., Genovès, A., 2006. Three-dimensional structure of western Mediterranean cyclones. Int. J. Climatol. 26, 323–343.

Castelao, R., Barth, J., 2006. The relative importance of wind strength and alongshelf bathymetric variations on the separation of a coastal upwelling jet. J. Phys. Oceanogr. 36, 412–425.

Castelao, R. M., Barth, J. A., 2007. The Role of Wind Stress Curl in Jet Separation at a Cape. J. Phys. Oceanogr. 37, 2652–267.

Castellari, S., Pinardi, N., Leanman, K., 2000. Simulation of water mass formation processes in the Mediterranean Sea: Influence of the time frequancy of the atmospheric forcing. J. Geophys. Res. 105 (C10), 24157–24181.

Charnock, H., 1955. Wind stress on a water surface. Quart. J. Roy. Meteor. Soc. 81, 639–640.

Chen, Y., Beveridge, M., Telfer, T., 1999a. Physical characteristics of commercial pelleted atlantic salmon feeds and consideration of implications for modeling of waste dispersion through sedimentation. Acquacult. Int. 7, 89–100.

Chen, Y., Beveridge, M., Telfer, T., 1999b. Settling rate characteristics and nutrient content of the faeces of Atlantic salmon, $Salmo\ salar$ L., and the implications for modelling of solid waste dispersion. Acquac. Res. 30, 395–398.

Chèruy, F., Speranza, A., Sutera, A., Tartaglione, N., 2004. Surface winds in the Euro-Mediterranean area: the real resolution of numerical grids. Annales Geophysicae 22, 4043–4048.

Chiswell, S., Roemmich, D., 1998. The east cape current and two eddies: a mechanism for larval retention? N. Z. J. Mar. Freshwat. Res. 32 (3), 385–397.

Chu, P., Ivanov, L., Margolina, T., 2007. On non-linear sensitivity of marine biological models to parameter variations. Ecol. Model. 206, 369–382.

COM, 2001a. Commission of the European Communities, Brussels. Biodiversity action plan for fisheries 162.

COM, 2001b. Commission of the European Communities, Brussels. A Sustainable Europe for a Better World: A European Union Strategy for Sustainable Development 264.

COM, 2002. Commission of the European Communities, Brussels. A Strategy for the sustainable development of European aquaculture Strategy for Sustainable Development 511.

Conte, A., Pavone, A., Ratto, C., 1998. Numerical evaluation of the wind energy resource of Liguria. J. Wind Eng. Ind. Aerodyn. 74-76, 355–364.

Corner, R., Brooker, A., Telfer, T., Ross, L., 2006. A fully integrated GIS-based model of particulate waste distribution from marine fish-cage sites. Aquaculture 258, 299–311.

Coutis, P., Middleton, J., 2002. The physical and biological impact of a small island wake in the deep ocean. Deep Sea Research Part I: Oceanographic Research Papers 49(8), 1341–1361.

Cox, M., 1975. A baroclinic model of the world ocean: Preliminary results. In: Numerical Models of Ocean Circulation. Washington, DC: National Academy of Sciences, 107–120.

Crépon, M., Boukthir, M., 1987. Effect of deep water formation on the circulation of the Ligurian Sea. Annales Geophysicae 5B(1), 43–48.

Crépon, M., Wald, L., Monget, J., 1982. Low-frequency waves in the Ligurian Sea during December 1977. Journal of Physical Oceanography 87, 595–600.

Cromey, C., Nickell, T., Black, K., 2002. DEPOMOD-modelling the deposition and the biological effects of wastes solids from marine cage farms. Aquaculture 214 (1-4), 211–239.

Csanady, G., 1982. Circulation in the coastal ocean. D.Reidel Publishing Company, Kluwer Group, Dordrech, Holland.

Cummins, P. F., Mysak, L. A., 1988. A quasi-geostrophic circulation model of the northeast Pacific. Part I: A preliminary numerical experiment. J. Phys. Oceanogr. 18(9), 1261–1286.

Dalsgaard, T., Krause-Jensen, D., 2006. Monitoring nutrient release from fish farms with macroalgal and phytoplankton bioassays. Aquaculture 256(1-4), 302–310.

Dalsgaard, T., Nielsen, L., Brotas, V., Underwood, G., Nedwell, D., Sundbck, K., Rysgaard, S., Miles, A., Bartoli, M., Dong, L., Thornton, D., Ottosen, L., Castaldelli, G., Risgaard-Petersen, N., 2000. Protocol handbook for NICE-Nitrogen cycling in estuaries: a project under the EU research programme. Marine Science and Technology (MAST III), 62National Environmental Research Institute, Silkeborg, Denmark.

Davies, H. C., 1976. A lateral boundary formulation for multi-level prediction models. Quart. J. Roy. Meteor. Soc. 102, 405–418.

Davies, P., Dakin, J., Falconer, R., 1995. Eddy formation behind a coastal headland. J. Coast. Res. 11 (1), 154–167.

De Gaetano, P., Doglioli, A., Magaldi, M., Vassallo, P., Fabiano, M., 2008. FOAM, a new simple benthic degradative module for the LAMP3D model: an application to a Mediterranean fish farm. Aquac. Res. 39, 1229–1242.

Denniss, T., Middleton, J., Manasseh, R., 1995. Recirculation in the lee of complicated headlands: A case study of Bass Point. J. Geophys. Res. 100 (C8), 16087–16100.

Dilly, O., 2003. Regulation of the respiratory quotient of soil microbiota by availability of nutrients. FEMS Microbiology Ecology 43, 375–381.

Doglioli, A., 2000. *LAMP3D, un modello Lagrangiano per lo studio della dispersione di inquinanti in acque costiere*. Tesi di Laurea, Università degli Studi di Genova.

Doglioli, A., Griffa, A., Magaldi, M., 2004a. Numerical study of a coastal current on a steep slope in presence of a cape: The case of the Promontorio di Portofino. J. Geophys. Res. 109, C12033, doi: 10.1029/2004JC002422.

Doglioli, A., Magaldi, M., Vezzulli, L., Tucci, S., 2004b. Development of a numerical model to study the dispersion of wastes coming from a marine fish farm in the Ligurian Sea (Western Mediterranean). Aquaculture 231 (1-4), 215–235.

Dudley, R., Panchang, V., Newell, C., 2000. Application of a comprehensive modeling strategy for the management of net-pen aquaculture waste transport. Aquaculture 187, 319–349.

Echevin, V., Crèpon, M., Mortier, L., 2002. Simulation and analysis of the mesoscale circulation in the northwestern Mediterranean Sea. Ann. Geophys. 21, 281–297.

Esposito, A., Manzella, G., 1982. Current circulation in the Ligurian Sea. In: Nihoul, J. (Ed.), Hydrodynamics of semi-enclosed seas. Elsevier Scientific Publishing Company, Amsterdam, pp. 187–204.

Everitt, B., 1977. Cluster analysis. HEB, London.

Farmer, R., Pawlowicz, D., Jiang, R., 2002. Tilting separation flows: a mechanism for intense vertical mixing in the coastal ocean. Dyn. Atmos. Oceans 36, 43–58.

Findlay, R., Watling, L., 1997. Prediction of benthic impact for salmon net-pens based on the balance of benthic oxygen supply and demand. Mar. Ecol. Prog. Ser. 155, 147–157.

Flather, R., 1976. A tidal model of the nothwest european continental shelf. Mem. Soc. R. Sci. Liege Ser. 6 (10), 141–164.

Freeland, H., 1990. The flow of a coastal current past a blunt headland. Atmosphere-Ocean 28, 288–302.

Fulton, E., Parslow, J., Smith, A., Johnson, C., 2004. Biogeochemical marine ecosystem models II: the effect of physiological detail on model performance. Ecol. Model. 173, 371–406.

Geleyn, J., 1988. Interpolation of wind temperature and humidity values from model levels to the height of measurements. Tellus 40(A), 347–351.

Geleyn, J. F., 1981. Some diagnostics of the cloud-radiation interaction in the ECMWF forecasting model. Workshop on Radiation and Cloud-Interactions in Numerical Modelling, Reading, UK, 209.

Geleyn, J. F., Hollingsworth, A., 1979. An economical analytical method for the computation of the interaction between scattered and line adsorption of radiation. Contrib. Phys. Atmos. 52, 1–16.

Gerdes, R., 1993. A primitive equation ocean circulation model using a general vertical coordinate transformation. 1. Description and testing the model. Journal of Geophysical Research 98, 14,683–14,701.

Geyer, W., 1993. Three-dimensional tidal flow around headlands. J. Geophys. Res. 98 (C1), 955–966.

Gillibrand, P., Turrell, W., 1997. The use of simple models in the regulation of the impact of fish farms on water quality in Scottish sea lochs. Aquaculture 159, 33–46.

Gleeson, T., 1954. Cyclogenesis in the mediterranean region. Arch. Meteo. Geo. Bio. N6(2), 153–171.

Gowen, R., Bradbury, N., Brown, J., 1989. The use of simple models in assessing two of the interactions between fish farming and marine environment. In: DePauw, N., Jaspers, E., Ackefors, H., Wilkins, N. (Eds.), Aquaculture - A Biotechnology in Progress. European Aquaculture Society, pp. 1071–1080.

Guld, R., 2008. Oxygen dynamics of marine sediments. Marine Biology Research 4, 243–289.

Haidvogel, D., Beckmann, 1998. Numerical models of the coastal ocean. In: Brink, K., Robinson, A. (Eds.), The sea. Vol. 10. John Wiley & Sons,Inc., pp. 457–482.

Haidvogel, D., Beckmann, A., 1999. Numerical ocean circulation modeling. Vol. Series on environmental science and management Vol. 2. Imperial College Press.

Hall, P., Anderson, L., Holby, O., Kollberg, S., Samuelsson, M., 1990. Chemical fluxes and mass balances in a marine fish cage farm. i. carbon. Mar. Ecol. Prog. Ser. 61, 61–73.

Haltiner, G. J., Williams, R., 1980. Numerical Prediction and Dynamic Meteorology. 2d ed., John Wiley and Sons 477.

Hargrave, B., Holmer, M., Newcombe, C., 2008. Towards a classification of organic enrichment in marine sediments based on biogeochemical indicators. Marine Pollution Bulletin 56(5), 810–824.

Hayward, T., Mantyla, A., 1990. Physical, chemical and biological structure of a coastal eddy near cape mendocino. J. Mar. Res. 48, 825–850.

Henderson, A., Gamito, S., Karakassis, I., Pederson, P., Smaal, A., 2001. Use of hydrodynamic and benthic models for managing environmental impacts of marine aquaculture. Journal of Applied Ichthyology 17, 163–172.

Herbaut, C., Mortier, L., Crèpon, M., 1996. A sensitivity study of the general circulation of the Western Mediterranean Sea. J. Phys. Oceanogr. 26, 65–84.

Holmer, M., Kristensen, E., 1992. Impact of marine fish cage farming on sediment metabolism and sulfate reduction of underlying sediments. Mar. Ecol. Prog. Ser. 80, 191–201.

Holmer, M., Marbà, N., Diaz-Almela, E., Duarte, C., Tsapakis, M., Danovaro, R., 2007. Sedimentation of organic matter from fish farms in oligotrophic Mediterranean assessed through bulk and stable isotope (d13C and d15N) analysis. Aquaculture 262, 268–280.

Homar, V., Jansà, A., Campins, J., Genovès, A., Ramis, C., 2007. Towards a systematic climatology of sensitivities of Mediterranean high impact weather: a contribution based on intense cyclones. Nat. Hazards Earth Syst. Sci. 7, 445–454.

Hu, Z., Doglioli, A., Petrenko, A., Marsaleix, P., Dekeyser, I., 2009. Numerical simulations of eddies in the Gulf of Lion. Ocean Model. 28(4), 203–208.

Jø rgensen, S., Bendoricchio, G., 1994. Fundamentals of Ecological Modelling. Elsevier, Amsterdam.

John, M., Pond, S., 1992. Tidal plume generation around a promontory: effects on nutrient concentrations and primary productivity. Cont. Shelf Res. 12(2-3), 339–354.

Johns, B., Oguz, T., 1987. Turbulent energy closure schemes. In: Heaps, N. (Ed.), Three-Dimensional Coastal Ocean Models. In: Coastal Estuarine Science vol. 4. American Geophysical Union, 17–39.

Johns, B., Sinha, P., Dube, S., Mohanty, U., Rao, A., 1983. Simulation of storm surges using a three-dimensional numerical model: an application to the 1977 Andhra Cyclone. Quarterly Journal of the Royal Meteorological Society 109, 211–224.

Jones, O., Simons, R., Jones, E., Harris, J., 2006. Influence of seabed slope and Coriolis effects on the development of sandbanks near headlands. J. Geophys. Res. 111, C03020, doi:10.1029/2005JC002944.

Jusup, M., Klanjscek, J., Petricioli, D., Legovic, T., 2009. Predicting aquaculture-derived benthic organic enrichment: Model validation. Ecological Modelling 220, 2407–2414.

Kain, J. S., Fritsch, J. M., 1992. The role of the convective “trigger function” in numerical forecasts of mesoscale convective systems. Meteor. Atmos. Phys. 49, 93–106.

Karakassis, I., Hatziyanni, E., Tsapakis, M., Plaiti, W., 2000. Impact of cage farming of fish on the seabed in three mediterranean coastal areas. ICES J. Mar. Sci. 57, 1462–1471.

Kastendeuch, P., Kaufmann, P., 1997. Classification of summer wind fields over complex terrain. Int. J. Climatol. 17, 521–534.

Kaufmann, P., Weber, R., 1996. Classification of mesoscale wind fields in the MISTRAL field experiment. J. Appl. Meteorol. 35, 1963–1979.

Kaufmann, P., Whiteman, C., 1999. Cluster-analysis classification of wintertime wind patterns in the Grand Canyon region. J. Applied Meteorol. 38, 1131–1147.

Lehmann, R., 1993. On the choice of relaxation coefficients for Davies lateral boundary scheme for regional weather prediction models. Meteor. Atmos. Phys. 52, 1–14.

Lermusiaux, P., Chiu, C., Gawarkiewicz, G., Abbot, P., Robinson, A., Miller, R., Haley, P., Leslie, W., Majumdar, S., Pang, A., Lekien, F., 2006. Quantifying uncertainities in ocean predictions. In: Paluszkiewicz, T., Harper, S. (Eds.) Oceanography, special issue on Advances in Computational Oceanography 19(1), 92–105.

Lionello, P., Bhend, J., Buzzi, A., Della-Marta, P., Krichak, S., Jansà, A., Maheras, P., Sanna, A., Trigo, I., Trigo, R., 2006. Cyclones in the Mediterranean region: climatology and effects on the environment. Vol. Amsterdam: Elsevier (NETHERLANDS). In P.Lionello, P.Malanotte-Rizzoli, R.Boscolo (eds) Mediterranean Climate Variability.

Louis, J., Tiedke, M., Geleyn, J., 1982. A short history of the PBL parameterization at ECMWF. Proc. Workshop on Planetary Boundary Layer Parameterization, Shinfield Park, Reading, United Kingdom, ECMWF.

Lozano, C., Robinson, A., Arango, H., Gangopadhyay, A., Sloan, Q., Hadley, P., Anderson, L., Leslie, W., 1996. An interdisciplinary ocean prediction system: assimilation strategies and structured data models. In: Malanotte-Rizzoli, P. (Ed.), Modern Approaches to Data Assimilation in Ocean Modeling. Elsevier, 413–452.

Madala, R., Piacsek, S., 1977. A semi-implicit numerical model for baroclinic oceans. J. Comput. Phys. 23, 167–178.

Magill, S. H., Thetmeyer, H., Cromey, C. J., 28 February 2006. Settling velocity of faecal pellets of gilthead sea bream (Sparus aurata L.) and sea bass (Dicentrarchus labrax L.) and sensitivity analysis using measured data in a deposition model. Aquaculture 251 (2-4), 295–305.

Maheras, P., Flocas, H., Patrikas, I., Anagnostopoulou, C., 2001. A 40 year objective climatology of surface cyclones in the Mediterranean region: spatial and temporal distribution. Int. J. Climatol. 21, 109–130.

Malanotte-Rizzoli, P., Bergamasco, A., 1989. The circulation of the eastern Mediterranean: I. Oceanol. Acta 12, 335–351.

Malanotte-Rizzoli, P., Bergamasco, A., 1991. The wind and thermally driven circulation of the eastern Mediterranean Sea: II. The Baroclinic case. Dyn.Atmos.Oceans 15, 355–419.

Malguzzi, P., Tartaglione, N., 1999. An economical second order advection scheme for explicit numerical weather prediction. Quart. J. Roy. Meteor. Soc. 125, 2291–2303.

Marsaleix, P., Auclair, F., Estournel, C., 2006. Considerations on open boundary conditions for regional and coastal ocean models. Journal of Atmospheric and Oceanic Technology 23, 1604–1613.

Marsaleix, P., Auclair, F., Floor, J., Herrmann, M., Estournel, C., Pairaud, I., Ulses, C., 2008. Energy conservation issues in sigma-coordinate free-surface ocean models. Ocean Model. 20, 61–89.

May, P., 1982. Climatological Flux Estimates in the Mediterranean Sea: Part I. Winds and Wind Stresses. NORDA Technical Report 54.

McCabe, R., Pawlak, G., 2006. Form drag due to flow separation at a headland. J. Phys. Oceanogr. 36(11), 2136–2152.

Mellor, G., Yamada, T., 1974. A hierarchy of turbulence closure models for planetary boundary layers. J. Atmos. Sci. 31, 1791–1896.

Mellor, G., Yamada, T., 1982. Development off a turbulence closure model for geophysical fluid problems. Rev. Geophys. Space Physics 20 (4), 851–875.

Mesinger, F., Arakawa, A., 1976. Numerical methods used in atmospheric models. GARP Publication Series 14, 64.

Molcard, A., Pinardi, N., Iskandarani, M., Haidvogel, D., 2002. Wind driven general circulation of the Mediterranean Sea simulated with a Spectral Element Ocean Model. Dyn. Atmos. Oceans 35 (2), 97–130.

Morrisey, D., Gibbs, M., Pickmere, S., Cole, R., 2000. Predicting impacts and recovery of marine-farm sites in Stewart Island, New Zealand, from the Findlay-Watling model. Aquaculture 185, 257–271.

Moskalenko, L. V., 1974. Steady state wind driven currents in the eastern half of the Mediterranean Sea. Okianologia 4 (14), 491–494.

Murdoch, R., 1989. The effects of a headland eddy on surface macro-zooplankton assemblages north of Ontago Peninsula, New Zealand. Estuar. Coast. Shelf S. 29, 361–383.

Oliger, J., Sundstrom, A., 1978. Theoretical and practical aspects of some initial boundary value problems in fluid mechanics. SIAM J. Appl. Math 35, 419–446.

Orlanski, I., 1976. A simple boundary condition for unbounded hyperbolic flows. J. Comput. Phys. 21, 251–269.

Panchang, V., Cheng, G., Newell, C., 1997. Modeling hydrodynamics and aquaculture waste transport in Coastal Maine. Estuaries 20, 14–41.

Pattiaratchi, C., James, A., Collins, M., 1986. Island wakes and headland eddies: a comparison between remotely sensed data and laboratory experiments. J. Geophys. Res. 92 (C1), 783–794.

Pawlak, G., MacCready, P., Edwards, K., McCabe, R., 2003. Observations on the evolution of tidal vorticity at a stratified deep water headland. Geophys. Res. Lett. 30(24), 2234. doi:10.1029/2001JC001234.

Pérenne, N., Lavelle, J. W., Smith IV, D. C., Boyer, D. L., 2001. Impulsively started flow in a submarine canyon: Comparison of results from laboratory and numerical models. J. Atmos. Oceanic Technol. 18, 1698–1718.

Pergent-Martini, C., Boudouresque, C., Pasqualini, V., Pergent, G., 2006. Impact of fish farming facilities on Posidonia oceanica meadows: a review. Marine Ecology 27, 310–319.

Pinardi, N., Allen, I., De Mey, P., Korres, G., Lascaratos, A., Le Traon, P., Maillard, C., Manzella, G., Tziavos, C., 2003. The Mediterranean ocean Forecasting System: first phase of implementation (1998-2001). Ann. Geophys. 21(1), 3–20.

Pinardi, N., Masetti, E., 2000. Variability of the large-scale general circulation of the Mediterranean Sea from observations and modelling: a review. Palaeogeography, Palaeoclimatology, Palaeoecology 158, 153–173.

Pinardi, N., Navarra, A., 1993. Baroclinic wind adjustment processes in the Mediterranean Sea. Deep Sea Research 40(6):, 1299–1326.

Pingree, R., 1978. The formation of the shambles and other banks by tidal stirring of the seas. J.Mar. Biol. Ass. U.K. 58, 211–226.

Pusceddu, A., Fraschetti, S., Mirto, S., Holmer, M., Danovaro, R., 2007. Effects of intensive mariculture on sediment biochemistry. Ecol. Appl. 17, 1366–1378.

Rankin, K., Mullineaux, L., Geyer, W., 1994. Transport of juvenile gem clams (Gemma gemma) in a headland wake. Estuaries 17(3), 655–667.

Raymond, W., Kuo, H., 1984. A radiation boundary condition for multidimensional flows. Q. J. Roy. Meteor. Soc. 110, 535–551.

Reid, G., Liutkus, M., Robinson, S., Chopin, T., Blair, T., Lander, T., Mullen, J., Page, F., Moccia, R., 2009. A review of the biophysical properties of salmonid faeces: implications for aquaculture waste dispersal models and integrated multi-trophic aquaculture. Aquaculture Research 40, 257–273.

Ritter, B., Geleyn, J. F., 1992. A comprehensive radiation scheme for numerical weather models with potential applications in climates simulations. Mon. Wea. Rev. 120, 303–325.

Robinson, A. R., Haidvogel, D. B., 1980. Dynamical forecast experiments with a barotropic open ocean model. J. Phys. Oceanogr. 10(12), 1909–1928.

Roughan, M., Mace, J., Largier, J., Morgan, S., Fisher, J., Carter, M., 2005. Subsurface recirculation and larval retention in the lee of a small headland: a variation on the upwelling shadow theme. J. Geophys. Res. 110, C10027., doi:10.1029/2005JC002898.

Sadoux, S., Baey, J.-M., Fincham, A., Renouard, D., 2000. Experimental study of the stability of an intemediate current and its interaction with a cape. Dyn. Atmos. Oceans 31, 165–192.

Salmona, P., Veradi, D., 2001. The marine protected area of Portofino, Italy: a difficult balance. Ocean & Coastal Management 44, 39–60.

Schultz, P., 1995. An explicit cloud physics parameterization for operational numerical weather prediction. Mon. Wea. Rev. 123, 3331–3343.

Seinfeld, J. H., 1975. Air Pollution - Physical and chemical fundamentals. New York: McGraw-Hill.

Semtner, A., 1995. Modeling Ocean Circulation. Science 269(5229), 1379–1385.

Shulman, I., Lewis, J., Blumberg, A., Nicholas Kim, B., 1998. Optimized boundary conditions and data assimilation with application to the M2 tide in the Yellow Sea. Journal of Atmospheric and Oceanic Technology 15, 1066–1071.

Signell, R., Geyer, W., February 1991. Transient eddy formation around headlands. J. Geophys. Res. 96 (C2), 2561–2575.

Simons, T. J., 1974. Verification of numerical models of Lake Ontario. Part I, circulation in spring and early summer. J. Phys. Oceanogr. 4, 507–523.

Smagorinsky, J., 1963. General circulation experiments with the primitive equations, I. The basic experiment. Mont. Weather Rev. 91, 99–164.

Smagorinsky, J., 1993. Some historical remarks on the use of nonlinear viscosities. In: Galperin, B., Orszag, S. (Eds.), Large Eddy Simulations of Complex Engineering and Geophysical Flows. Cambridge University Press, Cambridge,UK.

Sommerfield, A., ???? In: Partial differential equations Lecture Notes on Theoretical Physics. Vol. Vol. 6., Year = 1949. Academic Press, San Diego, CA.

Spall, M., Robinson, A., 1989. A new open ocean, hybrid coordinate primitive equations model. Math. Comput. Simulat. 31, 241–269.

Stewart, I., 1992. Warning-handle with care! Nature 355, 16–17.

Stewart, R. H., 2008. Introduction to Physical Oceanography. College Station TX: Texas A&M Univ.

Stigebrandt, A., Aure, J., Ervik, A., Hansen, P., 2004. Regulating the local environmental impact of intensive marine fish farming III. A model for estimation of the holding capacity in the Modelling-Ongrowing fish farm-Monitoring system. Aquaculture 234, 239–261.

Swallow, J., Canston, G., 1973. The pre-conditionig phase of MEDOC 1969 - I. Observations. Deep Sea Research 20, 429–448.

Taupier-Letage, I., Millot, C., 1986. General hydrodynamical features in the Ligurian Sea inferred from the DYOME experiment. Oceanol. Acta 9(2), 119–131.

Theede, H., Ponat, A., Hiroki, K., Schlieper., C., 1969. Studies on the resistance of marine bottom invertebrates to oxygen-deficiency and hydrogen sulphide. Mar. Biol. 2, 325–337.

Therkildsen, M., Lomstein, B., 1993. Seasonal variation in net benthic C-mineralization in a shallow estuary. FEMS Microbiology Ecology 12, 131–142.

Trigo, I., 2006. Climatology and interannual variability of stormtracks in the Euro-Atlantic sector: a comparison between ERA-40 and NCEP/NCAR reanalyses. Clim. Dyn. 26, 127–143.

Trigo, I., Bigg, G., Davies, T., 2002. Climatology of cyclogenesis mechanisms in the Mediterranean. Mon. Weather Rev. 130, 549–569.

Trigo, I., Davies, T., Bigg, G., 1999. Objective climatology of cyclones in the Mediterranean region. J. Climate 12, 1685–1696.

Tsutsumi, H., Kikuchi, T., Tanaka, M., Higashi, T., Imasaka, K., Miyazaki, M., 1991. Benthic faunal succession in a cove organically polluted by fish farming. Marine Pollution Bulletin 23, 233–238.

UNEP/MAP/MED, P., 2004. Mariculture in the Mediterranean. MAP Technical Reports Series No. 140, UNEP/MAP, Athens.

Vassallo, P., Doglioli, A., Rinaldi, F., Beiso, I., 2006. Determination of physical behaviour of feed pellets in Mediterranean water. Aquac. Res. 37 (2), 119–126.

Verron, J., Davies, P. A., Dakin, J. M., 1991. Quasigeostrophic flow past a cape in a homogeneous fluid. Fluid Dyn. Res. 7, 1–21.

Vezzulli, L., Chelossi, E., Riccardi, G., Fabiano, M., 2002. Bacterial community structure and activity in fish farm sediment of the Ligurian Sea (Western Mediterrenean). Aquacult. Int. 10 (2), 123–141.

Vezzulli, L., Marrale, D., Moreno, M., Fabiano, M., December 2003. Sediment organic matter and meiofauna community response to long-term fish-farm impact in the Ligurian Sea (Western Mediterranean). Chem. Ecol. 19 (6), 431–440.

Vismara, R., 1992. Ecologia Applicata 2^a edizione. Hoepli, Milano.

Warn-Varnasa, A., Gangopadhyayb, A., Hawkinsc, J., Robinsond, A., 2005. Wilkinson Basin area water masses: a revisit with EOFs. Continental Shelf Research 25(2), 277–296.

Weatherly, G., Martin, P., 1978. On the structure and dynamics of the ocean bottom boundary layer. J. Phys. Oceanogr. 8, 557–570.

Weber, R., Kaufmann, P., 1995. Automated classification scheme for wind fields. J. Appl. Meteorol. 34, 1133–1141.

Wu, R., Lam, K., MacKay, D., Lau, T., Yam, V., 1994. Impact of marine fish farming on water quality and bottom sediment: a case study in the sub tropical environment. Marine Environmental Research 38, 115–145.

Zannetti, P., 1990. Air Pollution Modeling. Computational Mechanics Publications, Boston.